Low Frequency Variability of the Meridional Overturning Circulation

Xiuhua Zhu

Low Frequency Variability of the Meridional Overturning Circulation

Dissertation zur Erlangung des Doktorgrades der Naturwissenschaften
im Departement Geowissenschaften der Universität Hamburg
vorgelegt von
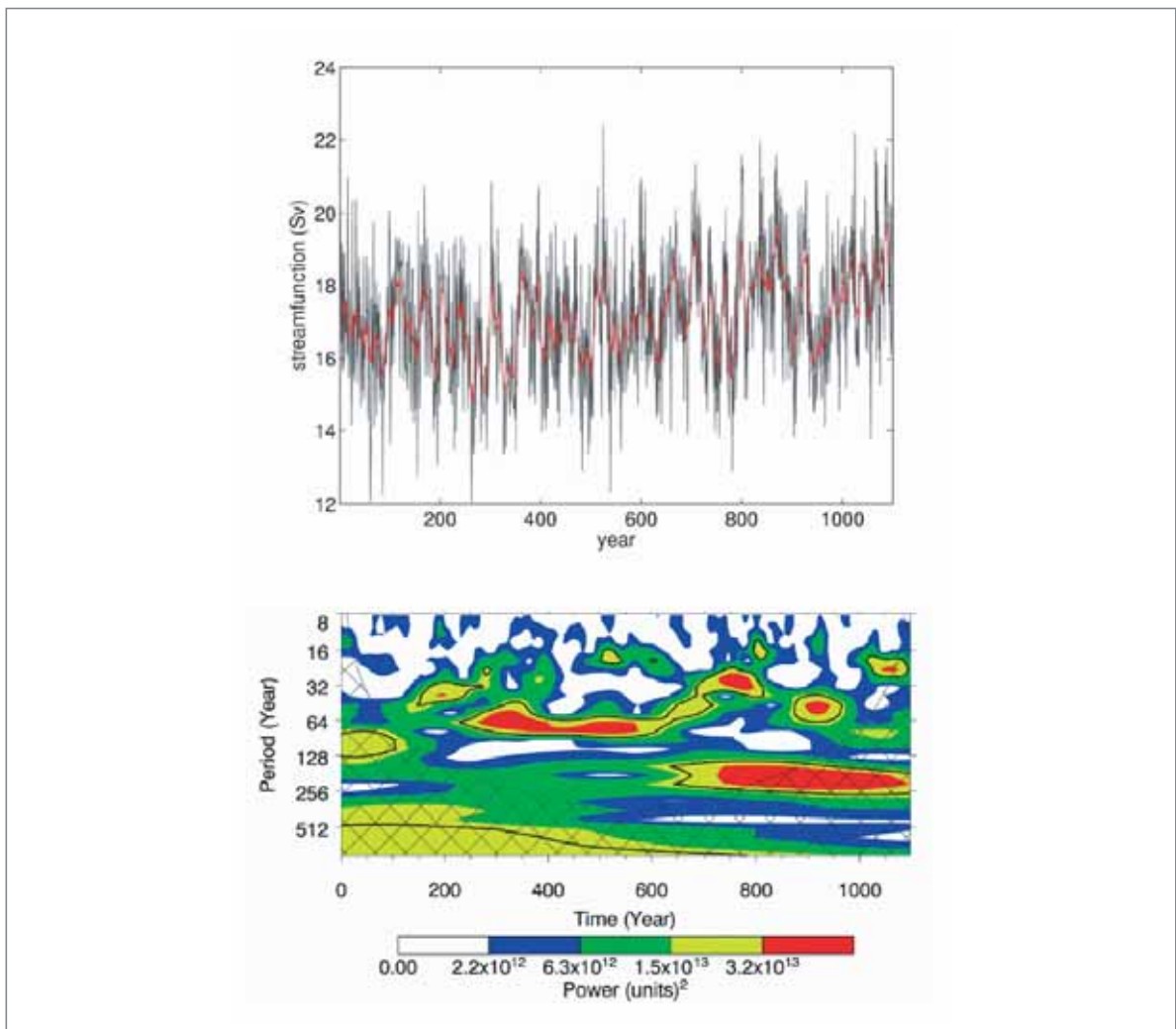
Xiuhua Zhu
aus China

Hamburg 2007

Xiuhua Zhu
Max-Planck-Institut für Meteorologie
Bundesstrasse 53
20146 Hamburg
Germany

Low Frequency Variability of the
Meridional Overturning Circulation

Xiuhua Zhu

Hamburg 2007

Contents

Abstract

The purpose of this thesis is to investigate the variability of the Meridional Overturning Circulation (MOC) using state-of-the-art GCMs, with a special interest on interdecadal to multidecadal time scales. We start from the general spectral behavior of the simulated MOC variability which is followed by detailed discussions on the low frequency variability of the MOC.

Though most of the current studies focus on specific periodicities of the MOC, no consensus has been reached on its general spectral behavior. Results from two coupled climate models are analyzed. A general consistency in the MOC spectrum exists between two coupled models, which, however, differ from the type often assumed with the MOC in previous studies. A comparison between two simulations of the same model with different resolution reveals substantial deviation on the MOC low frequency variability. These results suggest that caution is required concerning the MOC behavior at low frequencies which certainly should be considered to test model performance.

Analyses of a suite of sensitivity experiments suggest the coexistence of the inter- and multi-decadal variability (IDV and MDV), which are associated with an ocean self-sustained mode and an air-sea coupled mode respectively. This provides a new interpretation to the wide-spread time scales associated with the low frequency variability of the MOC.

The IDV is investigated using the ocean-only model driven by climatological surface fluxes. The important role of ocean dynamics in the North Atlantic subpolar gyre is highlighted. The IDV of the MOC is characterized as a geostrophic process, thus tightly associated with the horizontal density gradients. Our results provide a strong support to those derived from less complex models in previous studies.

The air-sea coupling is shown of great importance for the MDV of the MOC. While the MDV bears similarity to the mechanism associated with the IDV, our results show that presence of the air-sea coupling is critical to the existence of a significant MDV mode. This air-sea coupling involves a fast response of the ocean gyre to the anomalous wind stress, which enhances the density anomalies in the deep convection sites in the Labrador Sea and hence the associated MOC anomalies. The MOC-related variability in the North Atlantic also affects the North Pacific via atmosphere teleconnection through which the MOC variation at low frequencies impacts the North Pacific and potentially interacts with ENSO.

Chapter 1

Introduction

Introduction

1.1 Motivation

Observational studies show that the North Atlantic sea surface temperature (SST) dating back to the 19th century exhibits substantial decadal to multidecadal variability (Fig. 1.1, from Knight et al., 2005). It is often referred to as 'Atlantic Multidecadal Oscillation' (AMO) (Kerr, 2000; Enfield et al., 2001; Knight et al., 2005). It has been linked with the occurrence of Sahel drought, variability in Northeast Brazilian rainfall, North American and European summer climate and the frequency of Atlantic hurricanes (Knight et al., 2006), thus it is a large-scale mode. It is suggested that the AMO as a natural variability of the climate system mixes with the anthropogenic global warming signals (Andronova and Schlesinger, 2000), both of which with comparable amplitude (Knight et al., 2005). Therefore, to reduce the uncertainty in estimating the global warming signals, it is important and necessary to better understand the natural climate variability on the decadal to multidecadal time scales.
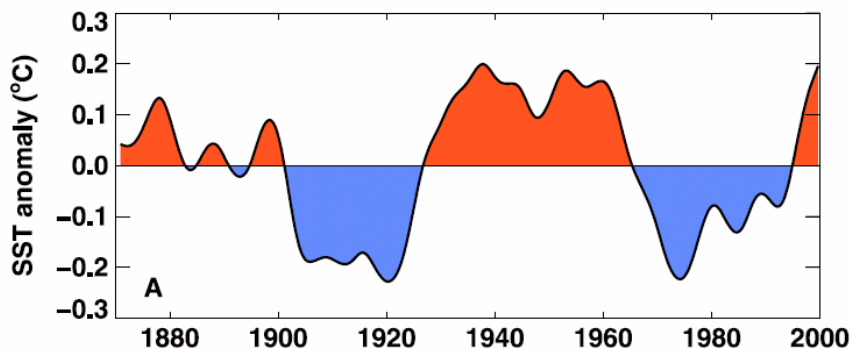
Fig. 1.1: AMO index derived from detrended area-weighted mean North Atlantic SST anomalies by using a Chebyshev filter with a half-power period of 13.3 years. SST data are from the HadISST data set (from Knight et al. 2005, Fig. 1a).

The forcing of the natural climate variability includes the interactions within and between the Earth's subsystems, such as the interaction between the atmosphere and oceans. The other source of forcing includes the variation of solar variability, volcanic eruptions, and orbital changes (Milankovitch cycles) which are often termed as 'external' forcing. The connection between the 'external' forcing and the climate variability are often hard to establish (e. g., Rind et al. 2002). In this thesis, we consider the climate variability on decadal to multidecadal time scales in a system comprising the ocean, the atmosphere and sea ice components which are dynamically interacting with each other.

Numerical models highlight a tight link between the North Atlantic SST variability and the meridional overturning circulation (MOC) composed of a wind-driven and a thermohaline-driven part (Delworth et al. 1993; Vellinga and Wu, 2004; Latif et al. 2004). The associated time scales of the MOC variability vary considerably among models, from 25 years in the coupled HadCM3 model (Dong and Sutton, 2005), 35 years in the coupled ECHAM-3/LSG model (Timmermann et al., 1998), to the 70-100 years oscillation in the Geophysical Fluid Dynamics Laboratory (GFDL) model (Delworth and Greatbatch, 2000). Three hypotheses have been proposed to explain the underlying mechanism of the MOC variability:

1) A self-sustained mode of ocean dynamics (e. g., Weaver et al. 1991; Te Raa and Dijkstra, 2002, 2003; Te Raa et al., 2004). Baroclinic wave dynamics (Colin de Verdiere and Huck 1999; Eden and Willebrand 2001) and advective processes (Marotzke and Klinger 2000; Goodman 2001: Eden and Greatbatch 2003) have been suggested to be associated with the ocean adjustment processes.

2) An oceanic response to stochastic forcing (e.g., Delworth and Greatbatch 2000). Delworth and Greatbatch (2000) reveal a 70-100 years oscillation in the GFDL model driven by stochastic atmospheric forcing. The dynamic

atmosphere-ocean coupling is not essential but acts to modify the amplitude. Similar conclusions have also been found in other studies (e. g., Griffies and Tzipermann 1995; Capotondi and Holland 1997).

3) An atmosphere-ocean coupled mode. The interaction between the North Atlantic Oscillation (NAO) and the ocean have been intensively discussed (Bjerknes 1964; Deser and Blackmon 1993; Kushnir 1994; Timmermann et al. 1998; Eden and Jung 2001; Eden and Willebrand 2001). The role of the ocean gyre and the thermohaline circulation (THC) in coupling with the atmosphere is often discussed separately (e.g., Wu and Liu 2005; see review of Latif 1998), though these two are often strongly coupled (Hátún et al., 2005; Dong and Sutton, 2005; MacMynowski and Tziperman, 2006). It is also suggested that other ocean basins may actively interact with the variability in the North Atlantic, for example, the interaction between the tropics and the North Atlantic (Latif et al. 2000; Hoerling et al. 2001) and the coupling between the North Pacific and the North Atlantic via atmospheric teleconnection (Timmermann et al. 1998; Wu and Liu 2005) and/or ocean wave adjustment (Timmermann et al. 2005).

Therefore, general consensus has not been achieved on the mechanism of the MOC variability on decadal to multidecadal time scales; details about how the ocean dynamics work and how the atmosphere and the ocean are coupled on the time scale concerned are not well understood. Besides, a probably more fundamental question is whether the model simulates the 'correct' general behavior of the MOC in terms of its spectrum. The MOC is generally assumed to follow a red-noise spectrum (Lorentzian), $1/[f_0^2 + f^2]$, with a damping time scale $1/f_0$ (e. g., Frankignoul et al. 1997; Von Storch et al. 2001), which was suggested by Hasselmann (1976) as a model for a damped, linear ocean forced by stochastic atmosphere. The spectral energy increases towards longer time scales and is limited by negative feedbacks in the climate system, thus leveled

off as white noise. However, this red-noise spectrum cannot explain the statistically significant spectral peaks superimposed on the red background. Further, this red-noise spectrum also cannot explain the long term memory (LTM) in the Greenland Ice Core $\delta^{18}O$ time series during the Holocene, featured as increasing spectrum energy with decreasing frequency up to millennial time scales (Blender et al. 2006). This LTM in the ice core, however, is well explained in the coupled CSIRO atmosphere-ocean model by the LTM in the MOC near Greenland and the Arctic Ocean (Blender et al. 2006). It is important to note that, though the LTM itself requires further evaluation, the LTM behavior has been found in various fields, such as atmospheric humidity (Pelletier and Turcotte 1997), river runoffs (Kantelhardt et al. 2006), surface temperature (Huybers and Curry, 2006) and sea level (Barbosa et al, 2006). The following interesting question is whether the observed periodicities are an inherent property of the nonstationary stochastic processes. This aspect should certainly be considered to test the model performance.

Therefore, we are still at a relatively early stage in understanding the North Atlantic decadal-to-multidecadal variability. The major problem is the lack of an adequate observational database, which inhibits us from verifying the mechanisms proposed.

1.2. Objective and outline of the thesis

The main objective of this thesis is to investigate the variability of the MOC on interdecadal to multidecadal time scales using state-of-the-art coupled GCMs which don't employ flux adjustment. The central questions addressed in this thesis are:

1) What are the spectral characteristics of the simulated MOC variability? Do they depend on the model set-ups?

2) What are the dominant time scales of the MOC variability?

3) What are the physical mechanisms behind the MOC variability?

To answer the first question, we analyzed the output from ECHAM5/MPI-OM and GFDL CM 2.1 in chapter 3. While general consistency is present between two different models, considerable differences also exist. Results from two simulations of ECHAM5/MPIOM with different resolution differ from each other mainly in the low frequency part. Results from § 3.1 of this chapter have been published in Geophysical Research Letters[1].

The second question is discussed in chapter 4. The fully coupled ECHAM5/MPIOM is analyzed together with a suite of ocean-only sensitivity experiments. There are two oscillations coexisting: an interdecadal (25-40 years) and multidecadal (45-80 years) variability (IDV and MDV). They can be traced back to different physical mechanisms as explained in chapters 5 and 6. This coexistence provides a new explanation for the wide-spread time scale of the simulated MOC variability in different numeric models.

The discussion for question 3 is presented in chapters 5 and 6. In chapter 5, the IDV is presented as an ocean internal mode sustained by the interaction between the deep water formed in the Labrador Sea and the subpolar gyre. Results of chapter 5 are prepared for a paper ready to be submitted[2]. Chapter 6 presents the MDV as an air-sea coupled mode. This chapter is in preparation for a publication[3].

──────────────────────

1 Zhu, X. H., K. Fraedrich, and R. Blender (2006), Variability regimes of simulated Atlantic MOC, Geophys. Res. Lett., 33, L21603, doi: 10.1029/2006GL027291.

2 Zhu, X. H., J. Jungclaus (2006), Low frequency variability of the MOC Part I: Interdecadal variability as an ocean internal mode, to be submitted.

3 Zhu, X. H., J. Jungclaus (2006), Low frequency variability of the MOC Part II: Multidecadal variability as an air-sea coupled mode, in preparation.

- 12 -

Chapter 2

Model description

Model description

The aim of this chapter is to introduce the numerical models used in this study. The main tool is the fully coupled atmosphere-ocean general circulation model — ECHAM5/MPIOM with two simulations with different resolution. Both simulations are analyzed with respect to the MOC variability regimes (chapter 3); the coarse-resolution simulation is the reference run with which results from the ocean-only experiments are compared (MPIOM only, chapter 4-5). It is also the base run for studying the air-sea coupled MOC variability (chapter 6). Output from the Geophysical Fluid Dynamics Laboratory (GFDL) CM 2.1 simulation is also analyzed for studying the MOC variability regimes (chapter 3), in comparison to the results of the high-resolution simulation of ECHAM5/MPIOM. The data set from GFDL model is freely available at *http://nomads.gfdl.noaa.gov/CM2.X/CM2.1*. All simulations in this thesis do not employ flux adjustment. My work involves performing ocean-only experiments using MPIOM, thus the following introduction of the ECHAM5/MPIOM focuses mainly on the ocean component.

ECHAM5/MPIOM:

The high-resolution coupled ECHAM5/MPIOM model, like the GFDL model introduced below, is prepared for the fourth Assessment Report (AR4) of the Intergovernmental Panel on Climate Change (IPCC). It consists of the atmospheric component ECHAM5, which has a horizontal resolution of 1.875^{o} $\times 1.875^{o}$ (T63) and 31 vertical levels. For more descriptions of ECHAM5, readers are referred to Roeckner et al. (2003).

The ocean/sea ice component of the model, MPIOM (Marsland et al., 2003), has a 1.5 ^{o} $\times$ 1.5 ^{o} horizontal resolution on a curvilinear grid with 40 vertical

levels. The primitive equations for a hydrostatic Boussinesq fluid are formulated with a free surface. The vertical discretization is on z-levels and the bottom topography is resolved by way of partial grid cells (Wolff et al., 1997). Using the formulation of Arakawa and Lamb (1977) the spatial arrangement of scalar and vector variables is formulated on a C-grid. The along-isopycnal diffusion is based on the work of Redi (1982) and is implemented following Griffies (1998). The effect of horizontal tracer mixing by advection with the unresolved eddies is parameterized following Gent et al. (1995). For the vertical eddy viscosity and diffusion the Richardson-number dependent scheme of Pacanowski and Philander (1981, PP hereafter) is applied. Since the PP scheme in its classical form underestimates the turbulent mixing close to the surface, an additional wind mixing parameterization is included. The wind stirring near the surface is proportional to the cube of the 10 m wind speed and decays exponentially with depth.

In the presence of static instability, convective overturning is parameterized by greatly enhanced vertical diffusion. A slope convection scheme has been included that allows for a better representation of the flow of statically unstable dense water over sills, such as in Denmark Strait or in the Strait of Gibraltar (see Marsland et al. (2003) for details) and off shelves, such as on the Arctic and Antarctic shelves.

The simulation analyzed in this thesis uses the same curvilinear grid setup as in Jungclaus et al. (2006, their Fig. 1). To avoid the singularity at the North Pole, the model's North Pole is shifted to Greenland and the South Pole is moved toward the center of the Antarctic continent. One advantage of the placement of the grid poles is a relatively high resolution in the deep-water formation regions of the Greenland Sea, Iceland Sea and Norwegian Sea (GIN), the Labrador Sea, and the Weddell Sea. A dynamic–thermodynamic Hibler-type (Hibler 1979) sea ice model is embedded in the ocean model code (see Marsland et al. 2003 for

details). The atmosphere and the sea ice–ocean models are coupled by means of the Ocean Atmosphere Sea Ice Soil (OASIS) coupler (Valcke et al., 2003). The ocean passes the sea surface temperature (SST), sea ice concentration, sea ice thickness, snow depth, and the ocean surface velocities to the atmosphere. River runoff and glacier calving are treated interactively in the atmosphere model and the respective fresh water fluxes are passed to the ocean as part of the atmospheric freshwater flux field. Various aspects of internal variability have been discussed by Jungclaus et al. (2006).

In the coarse-resolution simulation of ECHAM5/MPIOM, the atmosphere model has a horizontal resolution of $3.875^{o} \times 3.875^{o}$ (T31) and 19 vertical levels. The ocean component has $3^{o} \times 3^{o}$ average horizontal grid spacing but keeps the same vertical resolution as in the high-resolution simulation, with 40 unevenly spaced vertical levels. The poles are shifted in the same manner as in the high resolution ECHAM5/MPIOM.

The parameterization that accounts for the effects of ocean currents on surface wind stress is implemented in the high resolution model but not applied in this coarse resolution simulation. Without this parameterization an unrealistically strong westward propagation of SST anomalies in the tropical Pacific is simulated. The reasons for the changes in variability are linked to changes in both the mean state and to a reduction in atmospheric sensitivity to SST changes and oceanic sensitivity to wind anomalies (Jungclaus et al. 2006). Another difference is that both simulations employ different cloud schemes.

GFDL:

The coupled GFDL model is run in the version CM2.1 (Delworth et al., 2006). The atmosphere horizontal resolution is $2^{o} \times 2^{o}$ and 24 vertical levels. The ocean model formulation and physical parameterizations are described in detail in Gnanadesikan et al. (2006) and Griffies et al. (2005) and are based on the

Modular Ocean Model code (MOM4; Griffies et al. 2003). The ocean resolution is $1^{\circ} \times 1^{\circ}$, with a meridional resolution equatorward of 30 becoming progressively finer, such that the meridional resolution is 1/3 at the equator. There are 50 vertical levels in the ocean, with 22 evenly spaced levels within the top 220 m. The ocean component has poles over North America and Eurasia to avoid polar filtering (Murray, 1996). Atmosphere and ocean are coupled through the Flexible Modeling System coupler for calculating and passing fluxes between its atmosphere, land, sea ice, and ocean components. For a detail description, readers are referred to Delworth et al. (2006), Gnanadesikan et al. (2006).

Chapter 3

Variability regimes of the Meridional Overturning Circulation

§ 3.1 Variability regimes of the MOC in high resolution models[1]

3.1.1. Introduction

Climate variability is present on many time scales, ranging from seasons to millennia (Huybers and Curry, 2006). In the northern North Atlantic available instrumental records of sea surface temperature (SST) show low frequency variability (LFV, i.e. increasing power with decreasing frequency) in terms of power-law scaling up to decades (Fraedrich and Blender, 2003) revealing $1/f$ spectra (flicker noise) in particular regions. The $1/f$ spectra of SST can be explained by an ocean energy balance model with vertical diffusion forced by stochastic atmospheric surface and advective ocean heat fluxes (Fraedrich et al., 2004). These advective processes in the North Atlantic, which are related to the dynamics of the subpolar gyre, have also been identified as a source of oscillations (Eden et al., 2002; Eden and Greatbatch, 2003) and LFV (Junge and Fraedrich, 2006).

Defining the MOC as a circulation of mass, heat and salt, its variability is subject to processes which lead to changes of the mass, heat and salt transport, such as surface buoyancy forcing, wind forcing and internal ocean dynamics. For high frequency (intra-annual and annual) time scales, the spectrum is white. On these time scales, wind forcing dominates the MOC fluctuations (see e. g. Jayne and Marotzke, 2001), which is related to linear, barotropic dynamics

---

1 Zhu, X., K. Fraedrich, and R. Blender, 2006: Variability regimes of simulated Atlantic MOC, Geophys. Res. Lett., 33, L21603, doi: 10.1029/2006GL027291.

(Willebrand et al., 1980). In the transitional frequency regime, the scaling behavior is associated with the ocean's self-adjustment of the density field. The east-west density gradient can be induced by both wind stress and buoyancy forcing (Sturges and Hong, 1995; Delworth and Greatbatch, 2000). Frankignoul et al. (1997) found that this 'reddening' process is related to the westward propagation of the baroclinic Rossby waves and determined by the wave speed and basin width. They also identified the characteristic slop of the log-log spectrum is -2 $(1/f^2)$. For low frequencies, the ocean responds to the low frequency part of the stochastic atmosphere forcing and appears in the spectrum as white-noise plateau (Hasselmann 1976). In addition, oscillations have been identified in the North Atlantic at periods from decadal to centennial time scales (Mikolajewicz and Maier-Reimer 1990; Delworth and Greatbatch 2000, Eden and Jung 2001, Eden and Willebrand 2001; Eden and Greatbatch 2003).

The first generation of dynamic ocean models reproduced LFV, which, however, was not unique for all models. This leads to the conjecture that LFV is possibly due to model deficiencies since the oceanic circulation was assumed to be white on long time scales (von Storch et al., 2000). Relevant model deficiencies are too coarse resolutions and the parameterization of the vertical diffusion. However, it was shown that a 10ky simulation with a first generation AOGCM exhibits spectral scaling up to millennia in the North Atlantic in agreement with the reconstructed temperature variability in Greenland ice cores during the Holocene (Blender et al., 2006).

MOC power spectra are generally assumed to follow a red-noise spectrum (Lorentzian), $1/(f^2 + f_0^2)$, with a damping time scale $1/f_0$, which was suggested by Hasselmann (1976) as a model for a damped, linear ocean forced by a white stochastic atmosphere. This cannot explain either long term memory or white high frequency response. Thus the aim of this chapter is to revisit the spectral behavior of the MOC variability in the Atlantic on monthly to decadal

time scales. Emphasis lies on regime behavior, scaling properties and possible long term memory. Two 500 year control-runs with different state-of-the-art coupled AOGCMs (GFDL and ECHAM5/MPIOM) are analyzed to investigate the main characteristics of the monthly MOC fluctuations. The simulated mean states and analysis tools are described in Section 3.1.2. Results for particular levels and latitudes are compared (Section 3.1.3). Section 3.1.4 follows with a discussion and conclusions.

3.1.2. Simulated mean state and methods

Although the two integrations differ from each other in various aspects, the gross features of the Atlantic overturning are quite similar, i.e. northward inflow in the upper 1000-1500m, the subsequent deep-water formation in the North Atlantic and southward spreading in the deep Atlantic, and Antarctic inflow from still deeper layers. The maximum meridional streamfunction is located around 40N, between 1000 and 1500m (Fig. 3.1). The models tend to produce two regions of large standard deviation, one in the North Atlantic (45° N, 1500 to 2000m depth), and a second one in the South Atlantic (20° S, 1000m to 4500m), which is more intense in MPIOM.
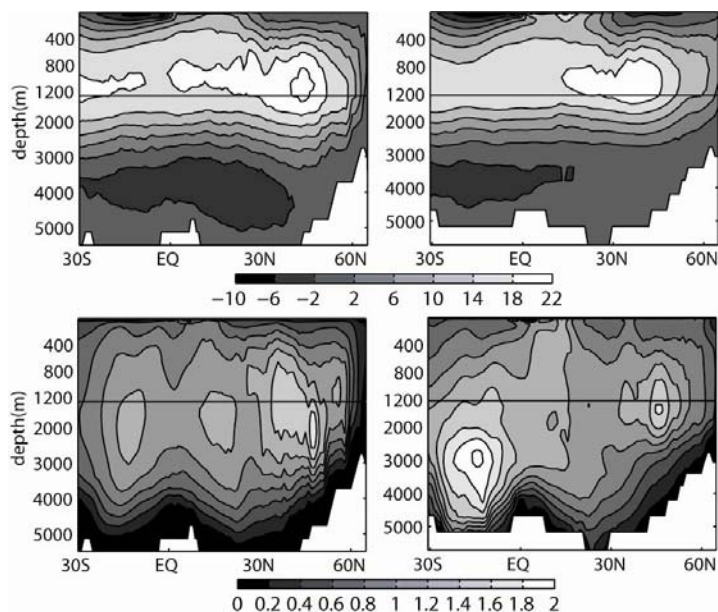

Fig. 3.1: Mean (upper) and standard deviation (lower) of the zonally averaged stream function (Sv) in the Atlantic for the GFDL model (left) and ECHAM5/MPIOM (right).

All time series are analyzed using power spectrum package of MATLAB, with 5 overlapping windows and Detrended Fluctuation Analysis (DFA). Power spectrum is often used to display spectrum of climate variables. However, it has a disadvantage that the interpretation of the 'low frequency part' (the longest frequency the time series could contain) depends on whether there are trends present in the variables. This shortcoming is well resolved in Detrended Fluctuation Analysis as explained in the following.

The DFA determines time scale dependent fluctuations in stationary anomaly sequences (Peng et al., 1994). This method yields the fluctuation function *F(t)* which measures fluctuations of the time series on time scales *t*. First, the anomaly time series, calculated by subtracting the monthly annual cycle, are integrated to the so-called profile. To determine the fluctuation function *F(t)*, the profile time series is partitioned in segments of duration *t*, and linear fits are calculated separately for each segment. The fluctuations *F(t)* are the means of the variances of the profile with respect to the fits. If the original time series shows trends or higher order polynomial growth types, then, instead of linear fits, polynomials of order *N* are fitted and subtracted in the segments; the method is then denoted as *DFA-N*. Here we apply *DFA-2* to eliminate linear trends. Thus the DFA is ideally suited to detect low frequency spectral power-law scaling in stationary time series when slow changes are present, for example, as a result of incomplete spin-up in the model (Fraedrich and Blender, 2003; Blender and Fraedrich, 2003). Here we apply *DFA-2* to eliminate linear trends, as a support to the results of the spectral analysis.

For power-laws in the power-spectrum, $S(f) \sim f^{-\beta}$, the DFA fluctuation function scales as $F(t) \sim t^{\alpha}$ with $\beta = 2\alpha - 1$. The autocorrelation function of the time series decays as $C(t) \sim t^{-\gamma}$ with $\alpha = 1 - \gamma / 2$. A time series has long term memory, if the integral of the autocorrelation function *C(t)* diverges. In this case $\gamma < 1$ and the related exponents are $\alpha > 1/2$ and $\beta > 0$. Stationarity of the time series is guaranteed for $0 < \beta < 1$. A stochastic process is denoted as white

for $\beta = 0$, while $\beta = 1$ is denoted as flicker or 1/f noise (acceptable for β from 0.7 to 1.3).

3.1.3. Variability regimes and scaling

The MOC is analyzed at two levels, near 1200m and 4000m, and at the latitudes 20° S, EQ, 20° N, 40° N, and 60° N, in both model runs. The upper level at 1200m depth sits inside the MOC cell associated with the spreading of North Atlantic Deep Water whereas 4000m depth sits inside the cell associated with the spreading of Antarctic Bottom Water. Note that in ECHAM5/MPIOM (GFDL) there are 3 (4) model levels below 4000m.

In order to illustrate the main properties of the time series and to compare the power spectrum with the DFA fluctuation function, the MOC at 40N and 1200m depth from the ECHAM5/MPIOM model is chosen (Fig. 3.2). The time series (a) shows that the MOC has become stationary; the remaining parts of this figure and the analyses are based on anomalies (annual cycle subtracted). Stationarity is checked for all time series (including lower levels) and the low frequency power spectra show no differences to the trend-eliminating *DFA-2*. The histogram (b) indicates that the MOC can be considered as Gaussian. The DFA fluctuation function (c) displays three regimes, identified with $\alpha \approx 0.5$ for both short and long time scales, and with $\alpha \approx 1$ in an intermediate range. The exponents in the power-spectrum (d) are related by $\beta = 2\alpha - 1$ and hint to $\beta = 0$ and $\beta = 1\ldots2$ in the corresponding time scale ranges. The intermediate range spectrum can either be interpreted as a Lorentzian (red-noise, with f^{-2}), or as a reminiscent of f^{-1} noise.
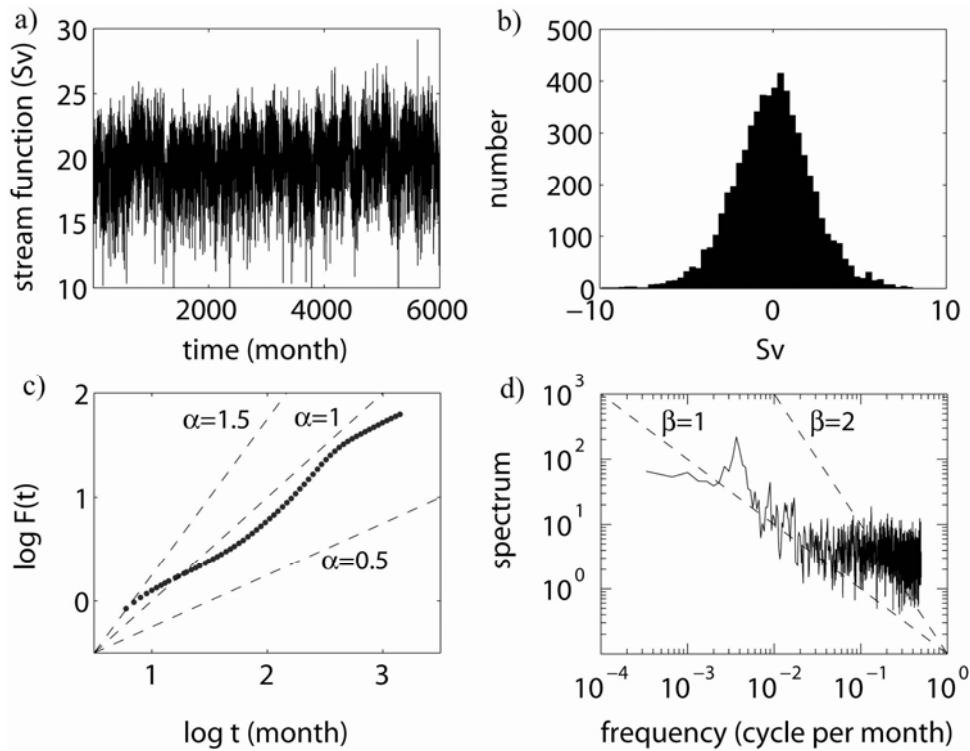
Fig. 3.2: MOC at 40° N, 1200m for the ECHAM5/MPIOM model: (a) time series, (b) anomaly frequency distribution, (c) fluctuation function by DFA-2, (d) power spectrum (5 overlapping windows). Dashed lines in (c, d) denote power-laws for exponents α and β as indicated.

In the upper ocean (near 1200m depth), GFDL and ECHAM5/MPIOM give consistent results on MOC scaling regimes (Fig.3.3-4). In the North Atlantic (at 40° N, 60° N), three frequency regimes appear: (i) for the highest frequencies (months to ~ 3 years), white noise dominates in almost all upper level time series. (ii) In the transition range (3 to 30 years) power-law scaling takes place, with $\alpha \approx 1$ ($\beta \approx 1$) in both models. An exception is at 40N in GFDL, with $\alpha \approx 1.5$ ($\beta \approx 2$). (iii) At periods of about 30 years an oscillation is superimposed. (iv) For low frequencies (beyond 30 years) white background fluctuations occur. At 60N in GFDL, the spectrum shows a weak long term memory. In the tropical and South Atlantic between 20° S and 20°N, both models reveal a white noise spectrum (consistent with a *DFA-2* scaling $\alpha \approx 0.5$), besides a peak with a period of 2 to 3 years. The white spectrum is even more pronounced in the equatorial region. However, GFDL reveals long term memory at 20ºN
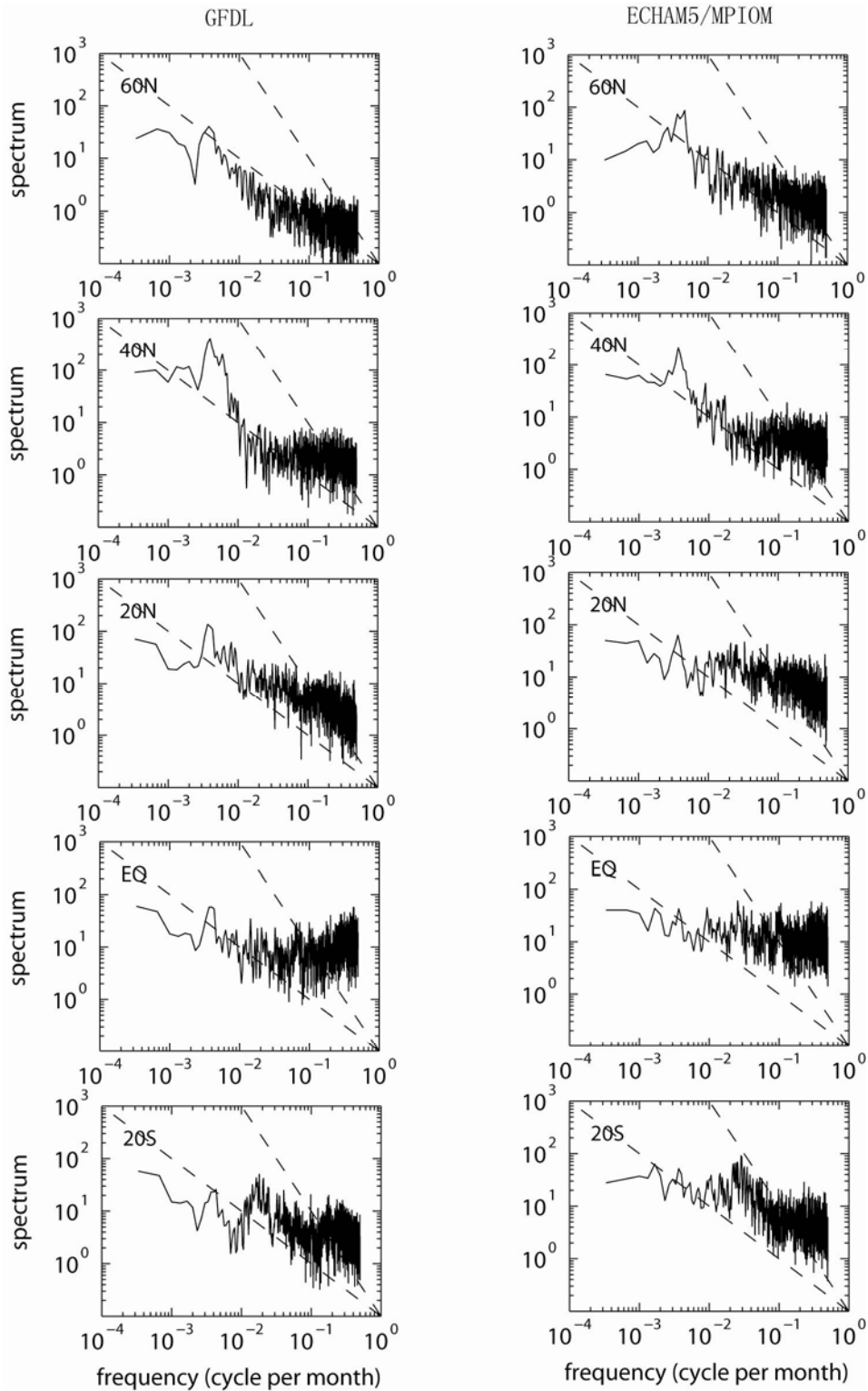
suggested by $\alpha \approx 1$ (Fig. 3.3-4).

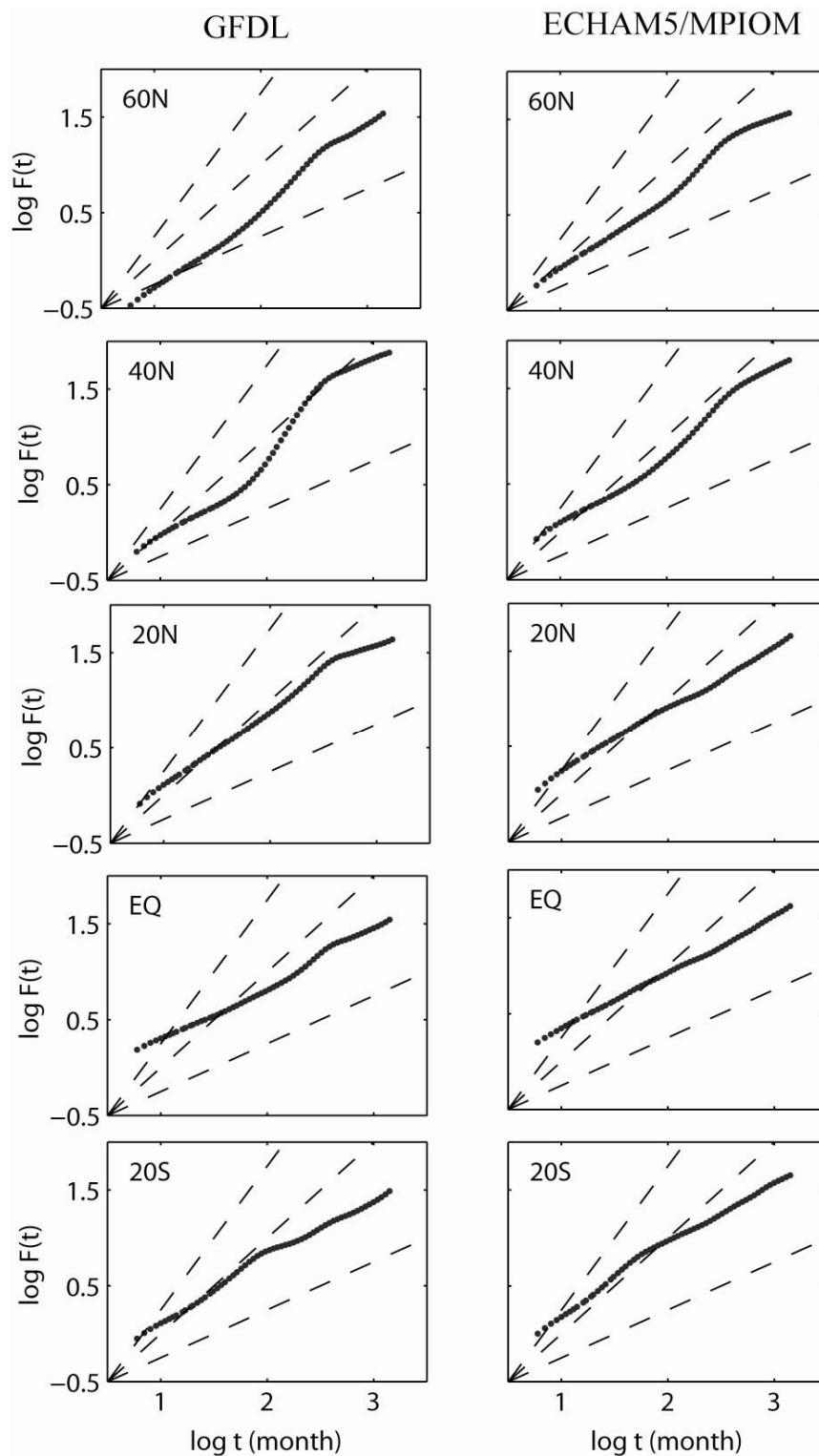Fig. 3.3: Power spectra of the upper MOC (near 1200m) in the GFDL (left) and ECHAM5/MPIOM model (right).

Fig. 3.4: DFA-2 of the upper MOC (near 1200m) in the GFDL (left) and ECHAM5/MPIOM model (right).

In the deep ocean (near 4000m depth) the spectral behavior is less clear since the spectra differ largely between different latitudes and between the two

models (Fig. 3.5 and Fig. 3.6). The following results are noted: (i) In the North Atlantic (40° N), the three-regime characteristics existing at 40N in the upper ocean in both models appear only in GFDL, while in ECHAM5/MPIOM the spectrum reveals white noise for high frequencies and damped energy with decreasing frequencies for low frequency. (ii) At 20° N, GFDL shows f^{-1} long term memory throughout the accessible range of months to hundred years, while ECHAM5/MPIOM spectrum shows damped energy at low frequencies. (iii) At the equator, both models show increasing energy for high frequencies (blue noise), white noise for low frequencies, and a superimposition of a 3-yr oscillation. (iv) At 20° S, a very pronounced oscillation with a period of 3 years is superimposed on the white background noise.
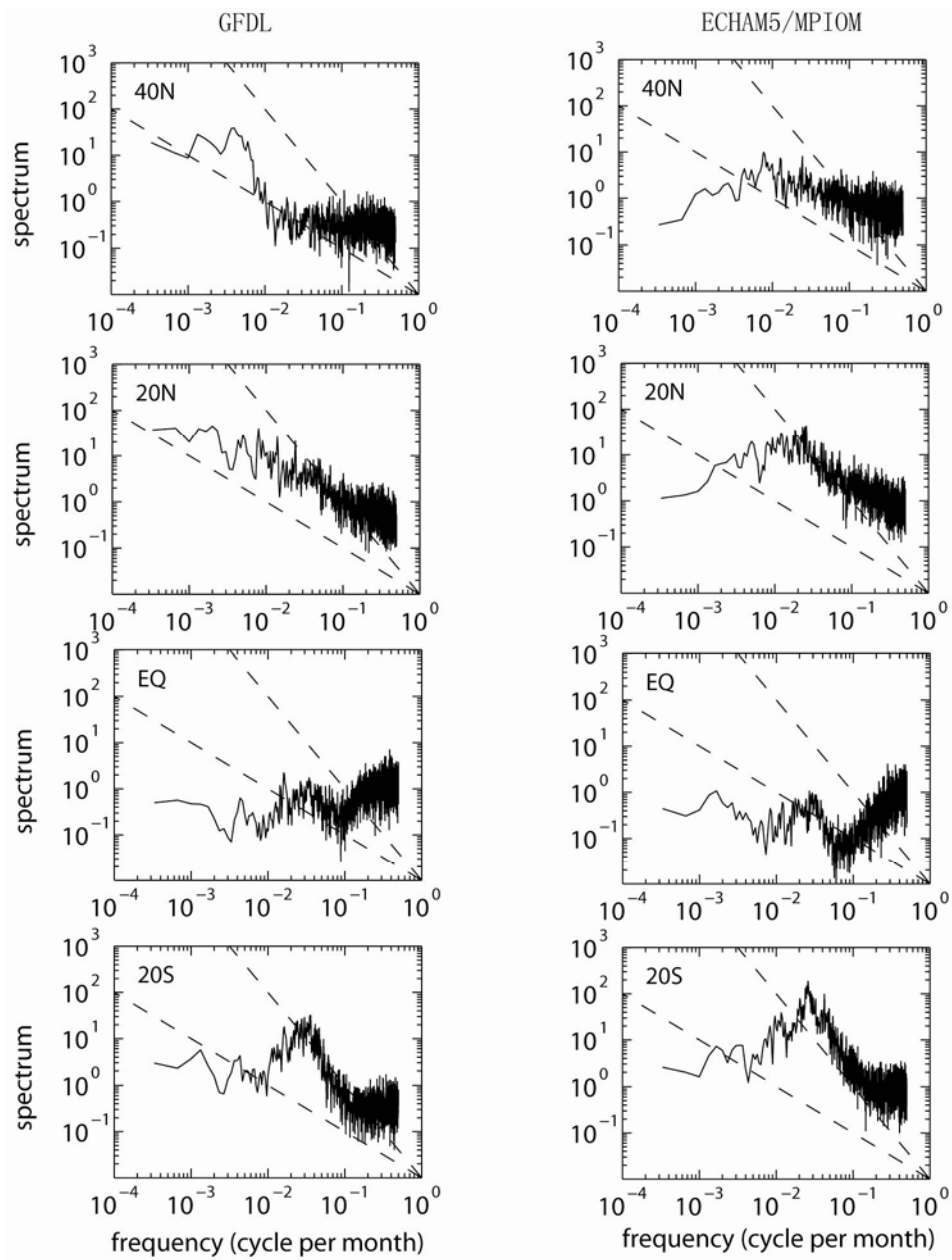
Fig. 3.5: Power spectra of the lower MOC (near 4000m) in the GFDL (left) and ECHAM5/MPIOM model (right).
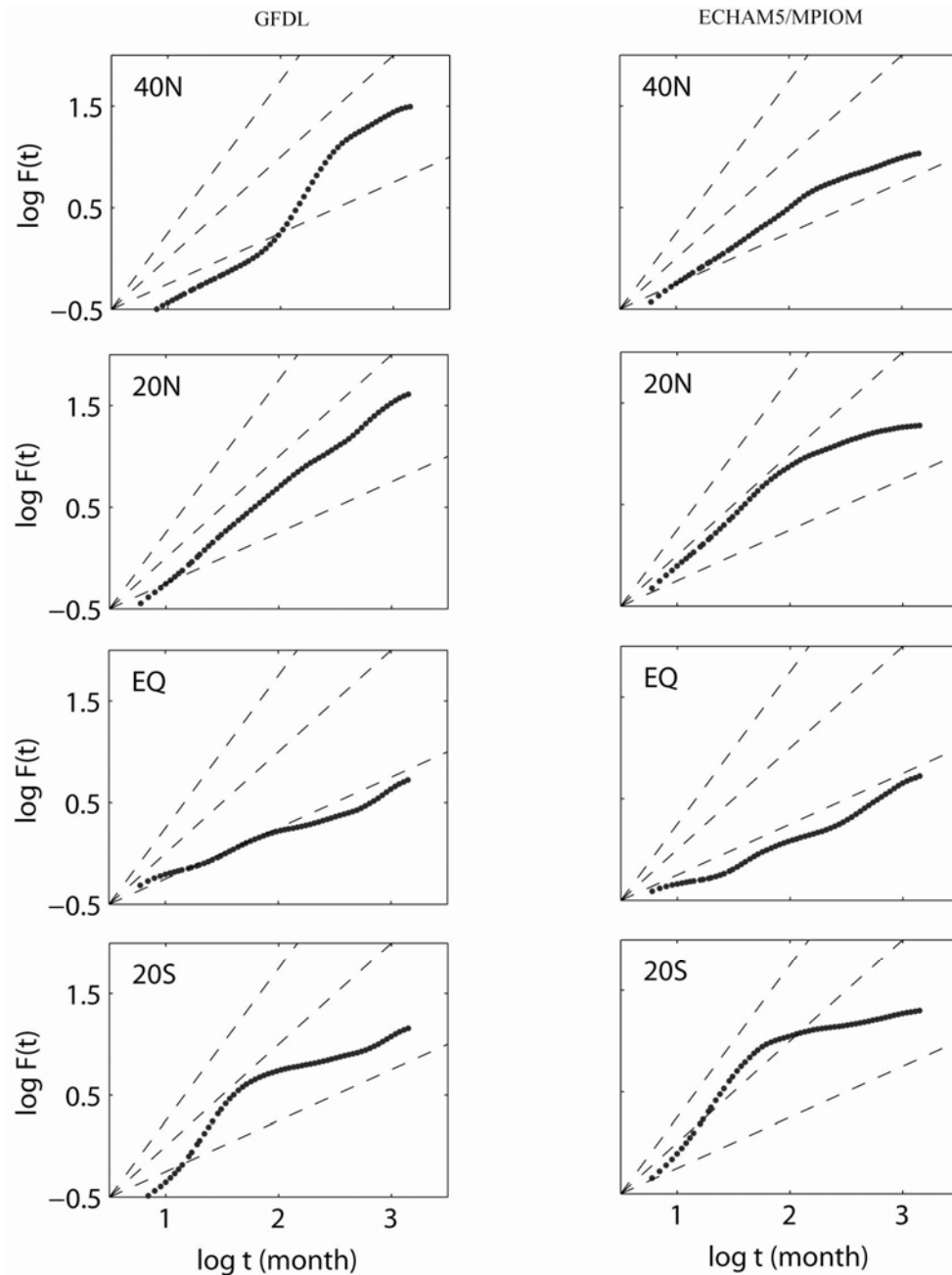
Fig. 3.6: DFA-2 of the lower MOC (near 4000m) in the GFDL (left) and ECHAM5/MPIOM model (right).
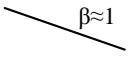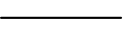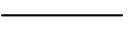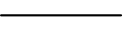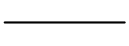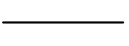
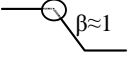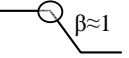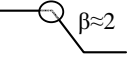## 3.1.4. Summary and discussions

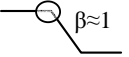Regime behavior of the variability of the Atlantic MOC is analyzed in two state-of-the-art coupled atmosphere-ocean general circulation models, GFDL and ECHAM5/MPIOM, which are used for IPCC simulations. The simulations

are designed as preindustrial control runs with durations of 500 years for which oceanic spin-up can be neglected. The variability of the monthly data is determined by power-spectra, which are supported by Detrended Fluctuation Analysis (DFA-2, which eliminates superimposed trends). The central aims of the analysis are the scaling properties of the spectra.
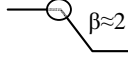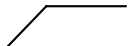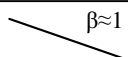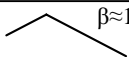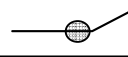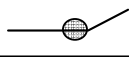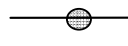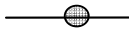
Table 3.1: sketch of main types of MOC power spectra found in the upper and lower level with ranges for the spectral exponent β. β is only given for the case of increasing energy with decreasing frequency.

Table 3.1-1: in the upper ocean

	GFDL	ECHAM5/MPIOM
60N	β≈1	β≈1
40N	β≈2	β≈1
20N	β≈1	
EQ		
20S		

○   indicates 30 yr oscillation

Table 3.1-2: in the lower ocean

	GFDL	ECHAM5/MPIOM
40N	β≈2	
20N	β≈1	β≈1
EQ		
20S		

◍   indicates the 3 yr oscillation

The main result is the existence of regimes of variability with distinct power-law relationships in the spectra (see table 3.1 for spectra sketch) demonstrating a general agreement between the two models. At high frequency, the spectrum in the upper ocean is white, which is very different from the

Hasselmann model. This is because, at short time scales, the MOC reflects the projection in the vertical plane (after zonal averaging) of the Topographic Sverdrup response of the ocean to the wind forcing, thus with barotropic structure, which can be seen from the leading EOFs of high pass filtered monthly MOC (Fig. 3.7, accounting for 81% of total variance). The strongest high frequency variability takes place near the equator (Fig. 3.8), mainly contributed by direct Ekman pumping. The absence of the white noise at high frequencies in the deep ocean is conjectured due to the frictional damping at the bottom levels.

EOF-3:
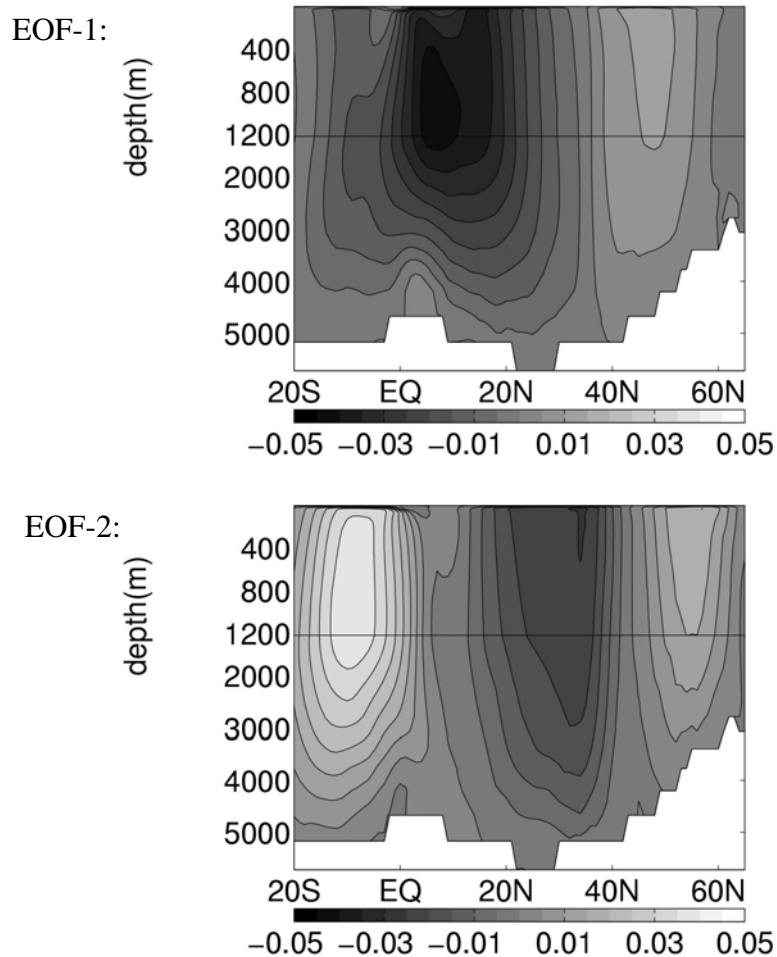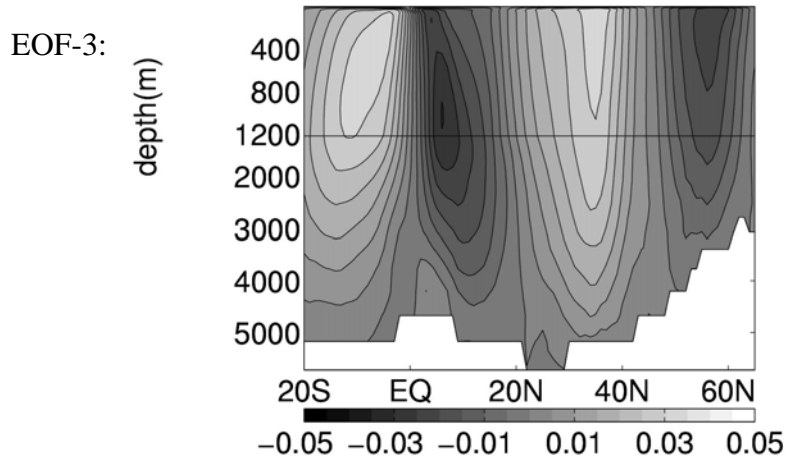
Fig. 3.7: The first three leading EOFs of the high pass filtered MOC from ECHAM5/MPIOM, with 3 years cut-off. The explained variance is 35%, 22%, and 24% respectively. Annual cycle is removed before the high pass filtering.

a

b
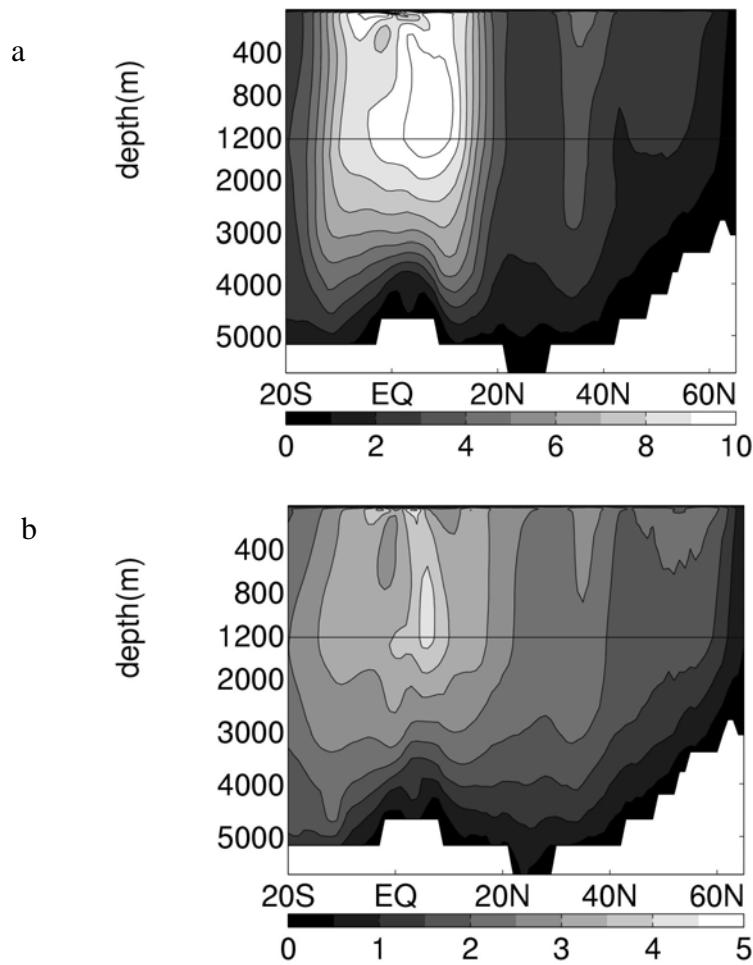
Fig. 3.8: standard deviation (Sv) of the high pass filtered MOC from ECHAM5/MPIOM, with 3 years cut-off in the case of with (a) and without (b) annual cycle. Note that the scale in two plots is different.

The most frequent spectral power-law, $S(f) \sim f^{-\beta}$, is found with $\beta \approx 1$, which is denoted as $1/f$ or flicker noise. Although red-noise $(1/[f_0^2 + f^2])$ is one of the most frequently used types of power-spectrum, this functional relationship appears to be more an exception than the rule. These types are hints to conceptual theories of the underlying mechanisms of MOC variability (see Fraedrich et al. (2004) for a stochastically forced vertical diffusion model and for references to other models).

In the low frequency range, both models show the presence of white noise. Discrepancy is found in the deep ocean, mainly in the North Atlantic: GFDL produces white noise while ECHAM5/MPIOM shows damped energy with decreasing frequency. This discrepancy at low frequencies hasn't been found before. It concerns model performance at low frequencies and hence should be considered in future studies.

In the North Atlantic an oscillation of about 30 years is found in both models. This oscillation may be accompanied by the ocean adjustment via baroclinic Rossby waves (Frankignoul et al. 1997), or geostrophic advection (e. g., Eden and Willebrand 2001; Eden and Greatbatch 2003). In the South Atlantic 2 to 3 years periodicity dominates, whose origin is still unknown.

The absence of the red-noise spectra has consequences for frequently applied significance tests. In some spectra increasing variability for lower frequencies described by exponents $\beta > 0$ is found. This indicates that the North Atlantic circulation possesses long term memory with consequences for the analysis of long term climate variability, trends, and the assessment of anthropogenic climate signals.

§ 3.2 Variability regimes of the MOC in a coarse resolution model

This section aims to investigate the changes of the simulated MOC variability, in terms of power-law scaling behavior. Both spectrum analysis and *DFA-2* are applied to the MOC of the coarse resolution ECHAM5/MPIOM experiment, referred to as C-EM. The high-resolution ECHAM5/MPIOM experiment analyzed in previous section is referred to as H-EM. Readers are referred to chapter 2 for details of C-EM set up.

3.2.1. Mean state and variability regimes in C-EM

The model run is 1099 years in total; the last 700 years are analyzed during which both the MOC and the SST have reached their equilibrium. The maximum of the simulated mean MOC is about 18 Sv (Fig. 3.9a). C-EM shows a stronger wind-driven cell in the south Atlantic with a maximum of ~ 24 Sv. The maximum mass transport of the Antarctic Circumpolar Current (ACC) is about 250 Sv (not shown). This is due to a strong wind bias within the equatorial and South Atlantic. It is not yet clear what causes the wind bias. Wind stress energy input to the ocean exerts strong high frequency variability in the equatorial and South Atlantic region (Huang et al. 2006), felt by the ocean over the whole depth (Fig. 3.9b), with a maximum at 400 meters. As shown below，this biased wind energy input is clearly detected in the spectrum of the MOC, even in the deep ocean.
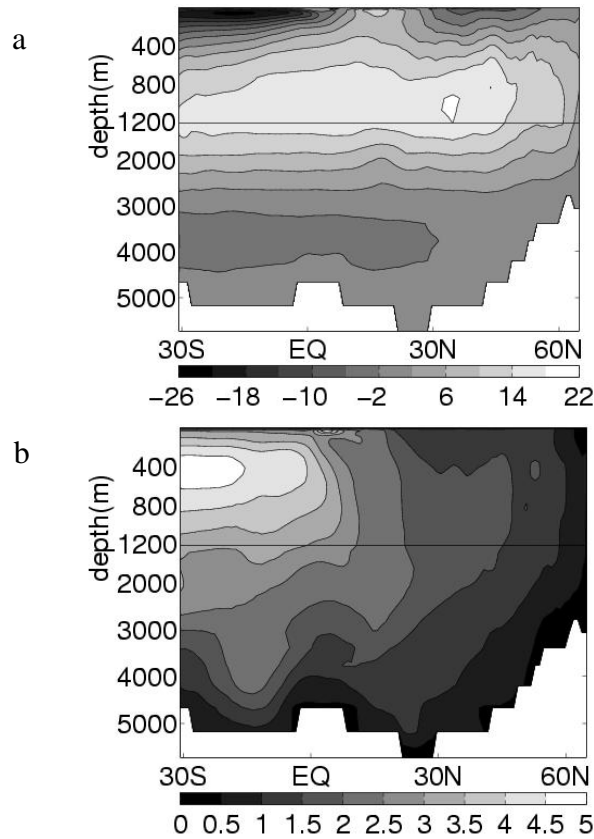
Fig. 3.9: Mean a) and standard deviation b) of the annual zonally averaged stream function (unit: Sv) in the Atlantic from C-EM (unit: Sv).

The time series of the MOC at selected depths, ~1200 m and 4000 m, at different latitudes are analyzed (Fig. 3.10-11). There is a general agreement between the high and coarse resolution simulation of ECHAM5/MPIOM on the spectral scaling, particularly in the range from months to decades. The main results are summarized as follows: (i) In the upper ocean (Fig. 3.10), white noise dominates from months to years, corresponding to $\beta \approx 0$ (Fig. 3.10, left panel) and $\alpha \approx 0.5$ (Fig. 3.10, right panel). The strong wind bias lifts up the spectrum energy level at this high frequency band, particularly pronounced at the equator and 20° S. A power-law scaling occurs from years to decades with $\beta \approx 1$ at all latitudes. (ii) In the deep ocean (Fig. 3.11), a) at 40° N, the spectra are similar in two models, with white noise from months to decades and decreased energy with decreasing frequency at low frequencies; b) at 20° N, in C-EM, white noise dominates from months to the largest resolvable time scale, while in H-EM spectral scaling occurs from months to decades with $\beta \approx 1$ and the

energy is damped at low frequencies (Fig. 3.5 right panel); c) at the equator and the south Atlantic (20° S), white noise dominates from months to near a decade on which a 3-yr oscillation is superimposed. The strong wind bias is also felt by the ocean at this depth, indicated as the higher spectrum energy at the high frequency band.
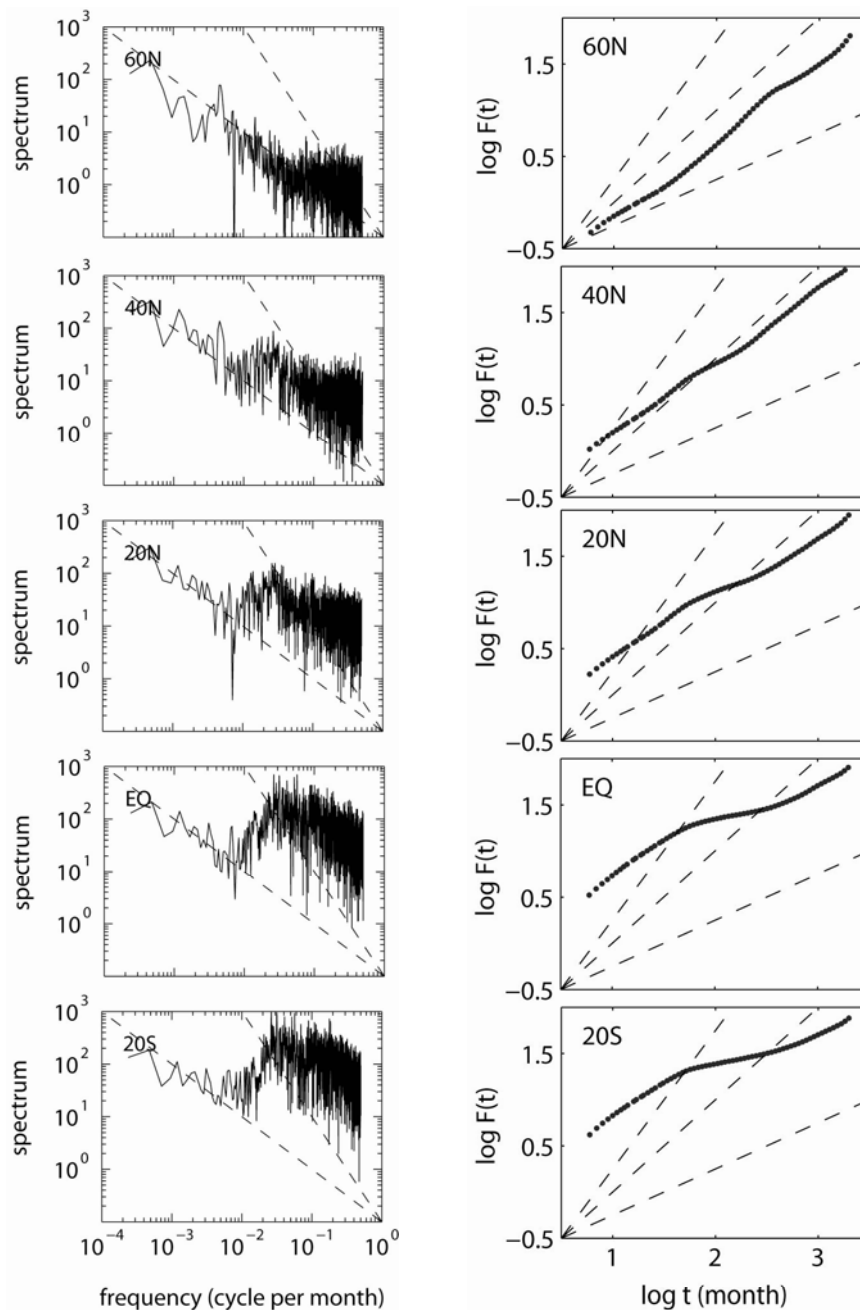
Fig. 3.10: Power spectrum (left panel) and DFA-2(right panel) of the upper MOC (near 1200m) in the coarse resolution ECHAM5/MPIOM model. 5 overlapping windows are used for spectrum calculation.
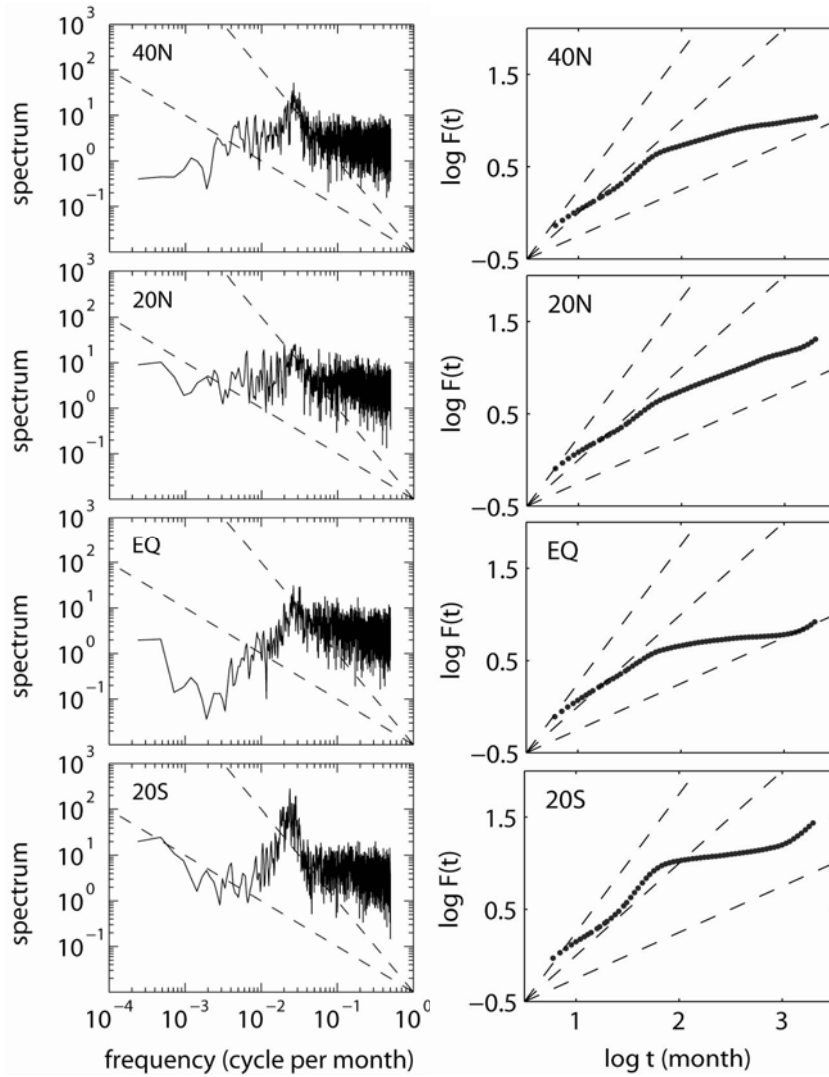
Fig. 3.11: Same as Fig. 3.10 but for the lower MOC (near 4000m)

The common feature between the two simulations is the white-noise spectra in the high frequency range (from months to years), reflected by $\beta \approx 0$ (in spectrum plots) and $\alpha \approx 0.5$ (in *DFA-2*). As explained in § 3.1, the variability at this high frequency part reveals the oceanic barotropic response to the white-noise wind forcing. A considerable difference occurs primarily in the low frequency range: in the upper ocean, the coarse-resolution simulation (C-EM) simulates a power-law scaling with β close to or slightly larger than 1 ($\alpha \approx 1$), while the finer resolution model shows a leveled – off spectrum ($\beta \approx 0$ and $\alpha \approx 0.5$) which is revealed by both the spectrum analysis and *DFA-2*. This discrepancy in the low frequency range is also visible in the lower ocean, particularly in the South Atlantic.

3.2.2. Summary and conclusions

Table 3.2: as in table 3.1, but with the coarse resolution ECHAM5/MPIOM experiment (C-EM) instead of GFDL. Results from the fine resolution ECHAM/MPIOM run (H-EM) are listed for comparison.

Table 3.2-1: in the upper ocean

	C-EM	H-EM
60N	$\beta \approx 1$	$\beta \approx 1$
40N	$\beta \approx 1$	$\beta \approx 1$
20N	$\beta \approx 1$	
EQ	$\beta \approx 1$	
20S	$\beta \approx 1$	

○ indicates 30 yr oscillation

Table 3.2-2: in the lower ocean

	C-EM	H-EM
40N		
20N		$\beta \approx 1$
EQ	$\beta \approx 1$	
20S	$\beta \approx 1$	

◉ indicates the 3 yr oscillation

In this section, the spectral behavior in the coarse resolution ECHAM5/MPIOM run (C-EM) is investigated. Results are compared with those from the high resolution ECHAM5/MPIOM run (H-EM). There is a general agreement in spectral behavior between the two simulations (table 3.2), particularly in the range from months to decades. Considerable disagreement is present in low frequency range, from decades to hundred years: the upper MOC in the coarse resolution experiment reveals more often *1/f* spectral scaling while

the finer resolution experiment shows a white plateau. The 30-yr peak in the C-EM is embedded in the scaling as part of the long term memory. The considerable difference in the lower MOC results from the strong wind bias in the coarse resolution simulation which lifts up the spectral energy from months to one decade. The 3-yr oscillation is still present.

The spectral power-law scaling of the MOC is also found in a coarse resolution atmosphere-ocean model – CSIRO/Mark 2 (Blender et al. 2006), thus it may arise as a common feature among coarse-resolution models. But we also note that in our studies, besides different resolution, the two simulations of ECHAM5/MPIOM employ different cloud schemes. Also, the influence of the ocean current on wind stress is implemented in the high-resolution simulation but not in the coarse-resolution simulation. These three factors will need to be considered when investigating what leads to the discrepancy between the two simulations with ECHAM5/MPIOM.

The possible presence of the long term memory (LTM) poses the following question: are numeric models able to represent high frequency variations (e. g., from years to decades) able to adequately represent the physics of multidecadal and longer-time scale climate variability? The answer to this question is of great importance for paleo-climate modeling, in which coarse resolution models are often used and their performance on very-long time scales becomes very important. The presence of LTM in the ocean, if it exists, might enable long-term climate predictability. The LTM should also be considered for trend-detecting issues related to climate change, because the 'trend' may come as part of the natural variability on 'long' time scales, as suggested by the higher power energy of the very low frequency variability.

Chapter 4

Coexistence of the inter- and
multi-decadal variability

4.1 Introduction

Decadal to multidecadal climate variability receives a lot of attention because it intermingles with the greenhouse warming signals in the present climate record and increases the difficulty in detection and prediction of global warming signals (e.g., Schlesinger and Ramankutty, 1994). It also has strong impacts on regional climate, particularly in the European sector (Sutton and Hodson 2005) and thus is crucial for climate predictions (Griffies and Bryan, 1997; Pohlmann and Latif 2005; Collins et al. 2006; Latif et al. 2006; Pohlmann et al. 2006).

The low frequency variability of the climate system has been observed in the Earth's natural archives in the form of proxy records, for instance, Mann et al. (1995) find variability on a 15-35 yr, as well as a 50-150 yr time scale in a study of several proxy data; Gray et al. (2003, 2004) found oscillations with a time scale of 30-70 yr and 60-100 yr in drought-sensitive tree-ring records.

Low frequency variability has also been detected in many oceanic variables. Using the historical hydrographic observations for two pentads, 1955-1959 and 1970-1974, Levitus (1989) identified coherent interdecadal differences from the sea surface down to 2000m. Displacements of isopycnals were found associated with these changes, but the reason for the displacements remains uncertain. Kushnir (1994) analyzed more than 100 years of data from the Comprehensive Ocean-Atmosphere Data Set and reported that negative SST anomalies prevailed from about 1900 to 1920 and from about 1970 to 1980, whereas the 1930-1960 period was characterized by warm anomalies. Associated with these temporal SST changes is a basin-scale spatial pattern with maxima in the Labrador Sea and northeast of Bermuda. This work was extended by Tourre et al. (1999) and a spectral peak around a period of 50-60 years was found. Low frequency variability with a period of 50-70 yr was also observed in instrumental data over the North Pacific, North America and the tropical oceans and reconstructed climate records for North America (Minobe 1997).

The natural climate variability can be caused by 'external' factors, such as changes of solar irradiance forcing (e. g., van Der Schrier et al. 2002), and volcano eruptions (e. g., Kirchner et al. 1999). However, the statistically significant relationships between external factors and climate proxy data are often hard to establish (e. g., Rind et al. 2002). Most likely, the low frequency variability of the climate arises within the climate system, as a result of the interaction between different subsystems, for example, atmosphere-ocean-sea ice coupling, or internal dynamics of one subsystem, such as ocean dynamics. Numerical models with different complexity are the main tools to investigate the related mechanisms.

It was found that the low frequency variability in the North Atlantic is closely related to the changes of the Meridional Overturning Circulation (MOC) (e. g., Delworth et al. 1993; Hakkinen 1999, 2000; Jungclaus et al. 2005). Three hypotheses have been proposed to explain the low frequency oscillation of the MOC:

1) An oceanic self-sustained oscillation (e.g., Weaver et al. 1991). The ocean adjustment signals may be carried by (viscous) boundary waves (Döscher et al. 1994; Winton 1996；Greatbatch and Peterson 1996; Eden and Willebrand 2001). Colin de Verdière and Huck (1999) suggest that a more general type of waves, with propagation speed depending on the background stratification. Baroclinic instability of the western boundary current is mentioned as the energy source of these waves. Other processes suggested involved in the ocean adjustment at low frequencies include the baroclinic Rossby waves (Frankignoul et al. 1997) and ocean advection (Marotzke and Klinger 2000, Goodman 2001, Eden and Greatbatch 2003).

2) An oceanic response to stochastic atmospheric forcing. Delworth and Greatbatch (2000) describe a 50-70 years oscillation in the Geophysical Fluid Dynamics Laboratory (GFDL) Modular Ocean Model (MOM). They

find this oscillation exist in the ocean model driven by stochastic atmosphere forcing, but not in the experiment when the variability of the atmosphere forcing is excluded. Thus they conclud that the low frequency variability (named as 'Multidecadal Variability' in their paper) is an oceanic response to stochastic atmospheric forcing. A two-way atmosphere-ocean coupling is not essential to the low frequency variability but acts to modify the amplitude. This is consistent with the results of previous studies (e. g., Griffies and Tzipermann 1995, Capotondi and Holland 1997).

3) An atmosphere-ocean coupled mode. In this 'two way' interaction, the ocean not only responds, but also feeds back, via SST anomalies, to the atmosphere. The North Atlantic Oscillation (NAO) is involved by a) directly changing the evaporation and the oceanic heat losses in the deep convection sites, and b) changing the subpolar gyre and the MOC (Timmermann et al. 1998, Wu and Liu 2005; Dong and Sutton 2005).

One thing to note is that the role of the gyre and the thermohaline circulation (THC) are often discussed separately. For example, Wu and Liu (2005) suggest that the coupling between the NAO and the ocean gyre is responsible for generating the North Atlantic decadal variability. The SST forces a NAO-like atmospheric response, which provides a negative feedback associated with the adjustment of the subtropical Atlantic to anomalous wind stress curl in the subtropics. However, the wind-driven gyre and the THC are strongly coupled (Macmynowski and Tziperman 2006). The dynamics of the subpolar Atlantic gyre are particularly important (Hátún et al. 2005), which affects the freshwater transport from the Arctic Ocean (Jungclaus et al. 2005) to the Labrador Sea and the location, intensity, and composition of the NAC and consequently its efficiency in transporting mass and heat from the tropics (Latif et al. 2000).

In summary, the origin of the low frequency variability of the MOC is still under debate and answers from different models are quite divergent. This work

aims to reinvestigate the low frequency variability of the MOC using the low resolution coupled general circulation model − ECHAM5/MPIOM. One advantage of using this model is that it does not employ any flux adjustment. It is found that in the coupled atmosphere-ocean model, there are two low frequency oscillations, one as an ocean self-sustained mode, and the other as a result of dynamic atmosphere-ocean coupling. This chapter is constructed as follows. The experiment design is introduced in section 4.2. Section 4.3 describes the features of the mean state and the low frequency variability in the coupled model. Main results are presented in section 4.4 and 4.5. This chapter is concluded by summary and discussions in section 4.6.

4.2 Experimental design

Since all processes are inherently coupled, it is difficult to confirm the speculations about the mechanisms responsible for the low-frequency variability within the context of a fully coupled model. Therefore, in addition to the fully coupled model, we have conducted a suite of experiments using the ocean component of the coupled model, MPIOM, driven by suitably chosen time series of surface flux forcing in a similar way as described in Delworth and Greatbatch (2000).

All model parameters in the ocean-only experiments are identical to those in the fully coupled model. Monthly surface fluxes from the coupled model integration are interpolated into daily data which are then used to drive the ocean model. In some experiments, climatological mean surface fluxes taken from the coupled model integration are used in stead, in this manner, variability of the atmospheric forcing term(s) concerned at time scales longer than the seasonal cycle is excluded. This design also allows us to evaluate the relative role of the atmosphere forcing terms in generating the MOC variability. In all ocean-only experiments, sea ice thickness is restored to climatology calculated

from the coupled run. This helps to reduce model drift. The suite of experiments is listed in Table 4.1.

Table 4.1

Experiments	Surface fluxes applied	Length of runs (yr)
CPL	atmosphere-ocean fully coupled	1099
CTR	Full surface fluxes from the fully coupled model (CPL) applied in the same sequence as they occurred in CPL	391
CLIM*	Climatological surface fluxes from CPL	1700
RAND*	Same as CTR, but the year of surface fluxes is randomly selected	1700
RAND-CLIMHEAT[+]	As in RAND, but with climatological surface heat fluxes	840
RAND-CLIMWATER[+]	As in RAND but with climatological surface freshwater fluxes	840
RAND-CLIMMOM[+]	As in RAND but with climatological surface wind-stress	840

*   the last 1100 years are analyzed.

[+]   All experiments start from the ocean conditions at the end of year 1408 from RAND.

In experiment CTR, the ocean model is driven by the surface fluxes in the same sequence as they occurred in the fully coupled model (CPL). In experiment RAND, for each year, one year of forcing is randomly selected from the coupled model output (from year 709 to year 1099). The forcing thus keeps its month-to-month variability every year as in the coupled model, but is randomly arranged from year to year. In this manner, there is no feedback from the ocean to the atmosphere and hence the ocean cannot change the atmospheric state and the air-sea fluxes. To evaluate whether oscillations are self-sustained by the

ocean, the ocean model is driven with climatological surface fluxes (CLIM), which are extracted from CPL year 700-750.

These three experiments (CTR, RAND, and CLIM) all start from the oceanic conditions at the end of year 708 from CPL. Experiment RAND and CLIM (see table 4.1) are in total 1700 years long. The last ~1100 years are analyzed. For reasons becoming clear later, three additional experiments are performed (Table 4.1). The ocean model is driven in the same way as in RAND, but one of the surface flux items is set to the corresponding climatological field. These three experiments start from the ocean condition at the end of year 1408 from RAND. They are 840 years long in total.

It should be noted that in all ocean-only experiments, there is no damping of SST anomalies through the surface heat flux term, since the surface heat fluxes are specified independently of SST. However, the restoring of sea-ice thickness to a climatological seasonal cycle provides an effective large-scale damping on the system. Negative (or positive) SST anomalies at higher latitudes will create positive (negative) anomalies of sea-ice thickness. As the sea-ice thickness is restored to its climatology, heat is effectively added to (removed from) the system. In this manner, there is no substantial model drift in all experiments.

4.3 Synopsis of the Inter- and multi-decadal variability

In the Atlantic the maximum of the simulated annual mean MOC (Fig. 4.1a) is about 18 Sv (1 Sv=10^6 m^3/s), located between 30° N and 40° N, at 1000 m. The model reproduces relatively weak Antarctic Bottom Water (AABW) Circulation, ~ 3 Sv, in comparison to observational data (4.3 Sv by Zemba, 1991; 6.9 Sv by Hogg et al. 1999). Compared to the finer horizontal resolution version of the ECHAM5/MPIOM (Fig. 3.1), CPL shows a stronger Deacon cell in the South Atlantic with a maximum of ~ 25 Sv and a maximum mass transport of the Antarctic Circumpolar Current about 250 Sv (not shown). This is due to a

strong wind bias in this model in the southern hemisphere, reflected in the MOC as the strong variability south of the Equator (Fig. 4.1b). The reason for this bias is unknown. To highlight the low frequency variability concerned, an 11-yr running mean is applied to the MOC at each grid point. The standard deviation has its maximum approximately 1.4 Sv at ~45° N, at 800m depth (Fig. 4.1c). The influence of the wind bias on the filtered field is negligible.
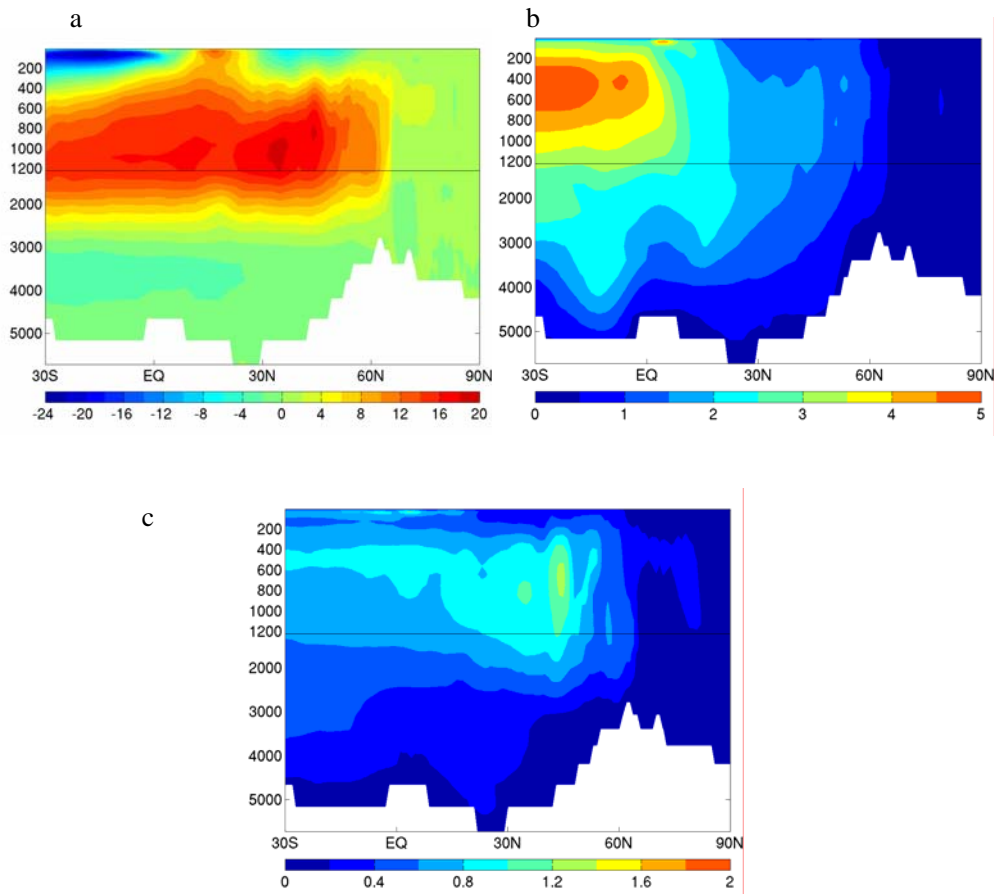
Fig. 4.1: Mean state (a), standard deviation (b,c) of the zonally averaged steamfunction in the Atlantic from the coupled run between year 400 and year 1099 (Units: Sv). In c, an 11-year running mean is applied before calculating the standard deviation.

The model simulates two deep convection sites in the North Atlantic (Fig. 4.2), one in the Greenland, Iceland, and Norwegian (GIN) Sea, with maximum Mixed Layer Depth (MLD) ~ 2500m, the other in the Labrador Sea, about

1500m deep. The convection center in the subpolar gyre is located near the southern tip of the Greenland, near the exit of the Labrador Sea, not in the interior Labrador Sea basin as observed (Lilly and Rhines 2002; Pickart et al. 2002). However, we still refer to this as the Labrador Sea (Basin) convection center. This simulated location implies that in our model the convection in the Labrador Sea is more sensitive to changes in the Irminger Sea and in the eastern subpolar gyre, such as East Greenland Current, overflows and the Irminger Current. At the same time, we notice that deep convection also takes place in the Irminger Sea though with a relatively shallower mean MLD, ~ 600-900m. The presence of deep convection in the Irminger Sea has been noted by Pickart et al. (2003). They found that it results from a local atmospheric structure and is closely related to the NAO.
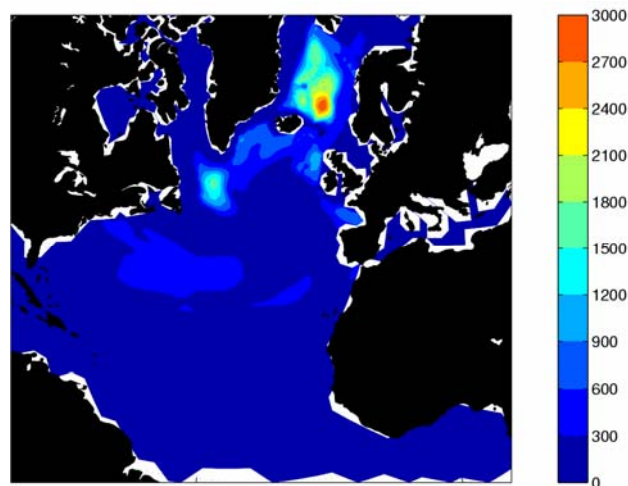

Fig. 4.2: Mean Mixed Layer Depth (Unit: m) in March in the coupled run from year 400 to year 1099.

The mean global SST experiences time-dependent drift (Fig. 4.3), about 0.1°C/centry for the first 400 years, and 0.03°C/ceutury for the last 700 years. Thus we regard the ocean reaches equilibrium in the last 700 years.
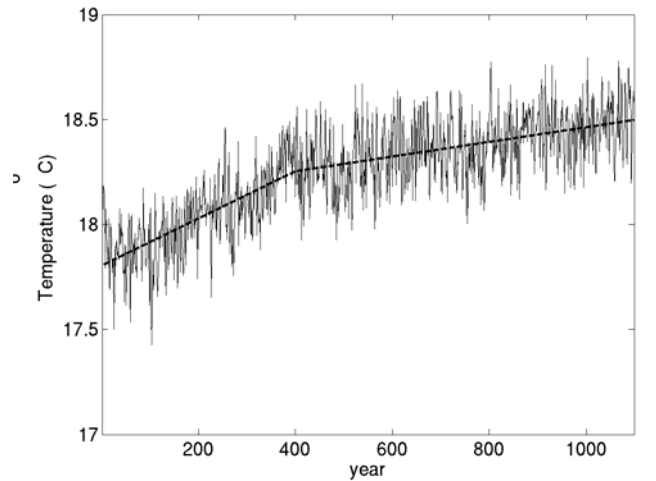
Fig 4.3: Time series of global mean sea surface temperature (6m deep) in CPL. Two linear trends are fit to the time series, plotted as thick dashed line. The drift is 0.1 °C/century in the first 400 years and 0.03 °C / century for the last 700 years.

The streamfunction at 30° N, 960m is selected as the MOC index, if not specified otherwise. It is quite stable through the entire time series (Fig. 4.4a) and exhibits considerable variability at timescales ranging from 20 to 100 years (Fig. 4.4b). We notice that between year 200 and year 600 the MDV signal is strong while the IDV signal is damped; and the IDV signal is strong between year 700 and year 1000 whereas the MDV signal is weak. This indicates that there is possibly energy transfer between the IDV and the MDV.

The spectrum of the MOC index is estimated by averaging spectra of 5 data subsets each of which contains 500 to 700 points and is randomly taken from different ranges of the time series. Consistently with the wavelet analysis (Fig. 4.4b), the spectrum shows concentrated energy in the periods between 25-40 years and 45-80 years (Fig. 4.5), which we refer to as Inter- and Multi- Decadal Variability (IDV and MDV) respectively. The spectrum of the last 700 years of the time series is calculated (red line in Fig. 4.5). The IDV and MDV are still captured in the spectrum. This allows us to limit our analysis of the coupled run to the last 700 years when the ocean has reached its equilibrium.
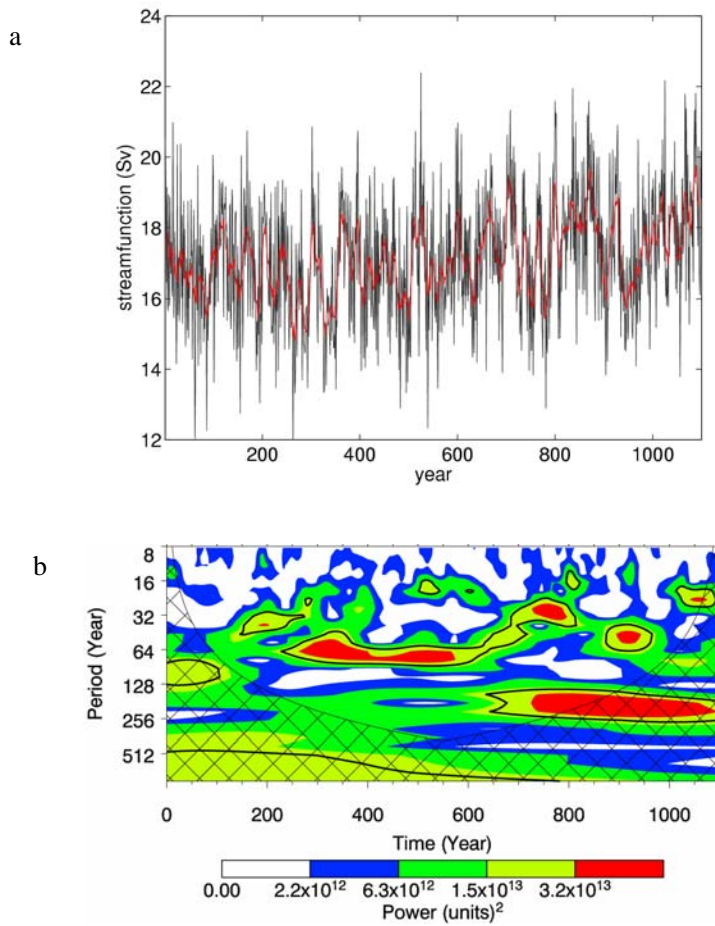
Fig 4.4: a) time series and b) wavelet analysis of the MOC index in the CPL. the red line in a) is the 11-yr running mean of the MOC index.
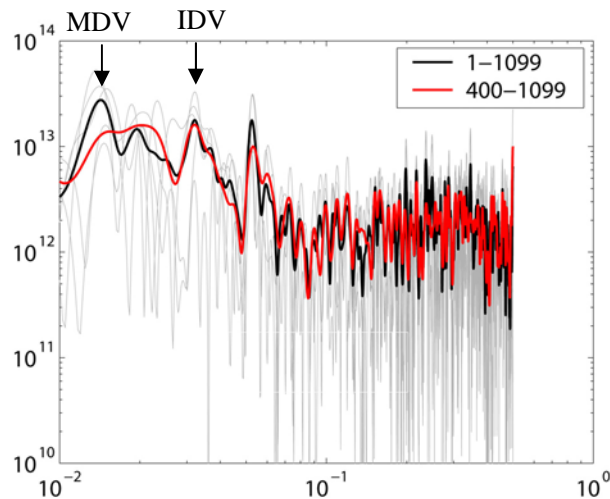
Fig 4.5: power spectrum density of the MOC index in the CPL. Gray lines show the spectrum for different periods of the time series in Fig. 4.3a for which one window is used. Black line is the mean of the gray lines. Red line shows the spectrum for the period between year 400 and year 1099; 5 window are used, with 3/4 window length as overlapping length.

The coexistence of the IDV and MDV provides a new interpretation for the widely-spread time scales associated with 'interdecadal' or 'multidecadal' variability reported in previous studies (e. g., 70-100 years in Delworth and Greatbatch, 2000; 35 yrs in Timmermann et al. 1998; 25 yrs in Dong and Sutton 2005). In the following it will be shown that IDV and MDV can be attributed to different physical mechanisms.

4.4 Are the inter- and multi-decadal variability coupled modes?

As introduced in the introduction, three hypotheses have been proposed responsible for the low frequency variability of the MOC. To evaluate which one takes effect on the inter- and multi-decadal time scales in our model, a suite of experiments using the ocean component of the coupled model – MPIOM are conducted (refer to table 4.1 for experiment set-up).

Experiment CTR almost fully reproduces the oscillations in CPL in the first ~ 100 years (Fig. 4.6). Afterwards the MOC gradually weakens by about 2 Sv relative to CPL. The weaker mean state of the MOC in CTR is possibly due to the reduced noise level. It has been found that the simulated mean state of the MOC will be considerably greater when daily variability of the forcing is considered in a coupled model (Balan, 2006). On the other hand, CTR still captures to a large extent the low-frequency oscillatory behavior of the MOC. This confirms that the strategy of using only the ocean component of the coupled model is appropriate for analyzing the MOC low frequency fluctuations.
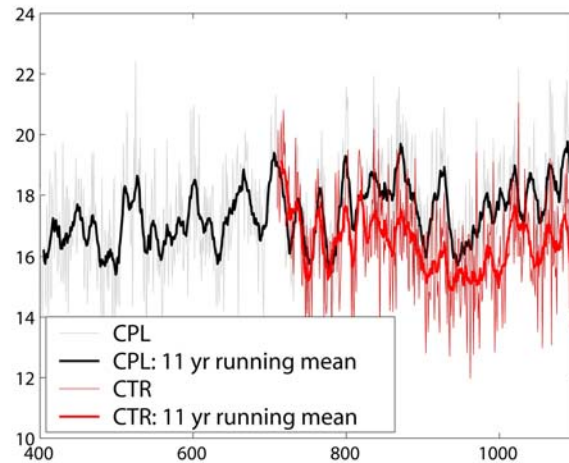
Fig. 4.6: time series of the MOC at 30° N, 960m depth from CTR and CPL (Units: Sv). CTR starts from year 709 to 1099. Thin gray and red lines denote raw MOC time series, and the thick lines denote the corresponding 11 running mean.

We regard 'coupling' as a process in which the state of the ocean (SST) strongly influences the large-scale state of the atmosphere, which in turn feeds back coherently upon the state of the ocean. In experiment RAND, each year the surface forcing is randomly arranged from year to year, thus there is no feedback from the ocean to the atmosphere. In experiment CLIM, atmospheric variability on time scales longer-than seasonal is excluded. Thus ocean dynamics are responsible for any present low frequency variability.

The mean state of the MOC index in RAND and CLIM is ~ 15 Sv, 3 Sv smaller than in CPL and 1 Sv smaller than CTR; the MOC in RAND is nosier than the one in CLIM (Fig. 4.7a). Considerable low frequency variability is present in RAND, which is also simulated in CLIM, however, with smaller amplitude of 0.8 Sv (Fig. 4.7b). The spectra of the MOC indices (Fig. 4.7c) reveal considerable variability centered at 30 yrs in both RAND and CLIM. The spectral energy at multidecadal time scales is considerably damped in CLIM and RAND compared to CPL. The same message can also be derived from the autocorrelation of the MOC indices (Fig. 4.8), CPL has two significant

harmonic frequencies with time scales of 30 and 60 years respectively (shown as the negative minima at +/- 15 and +/- 30 years), whereas CLIM and RAND both have only one 30 year oscillation. Therefore we conclude that IDV is an ocean internal mode which can be sustained by ocean dynamics; and the MDV is a result of dynamic air-sea coupling. Thus when the ocean is driven by stochastic or even climatological atmospheric forcing, the MDV signal is much damped.
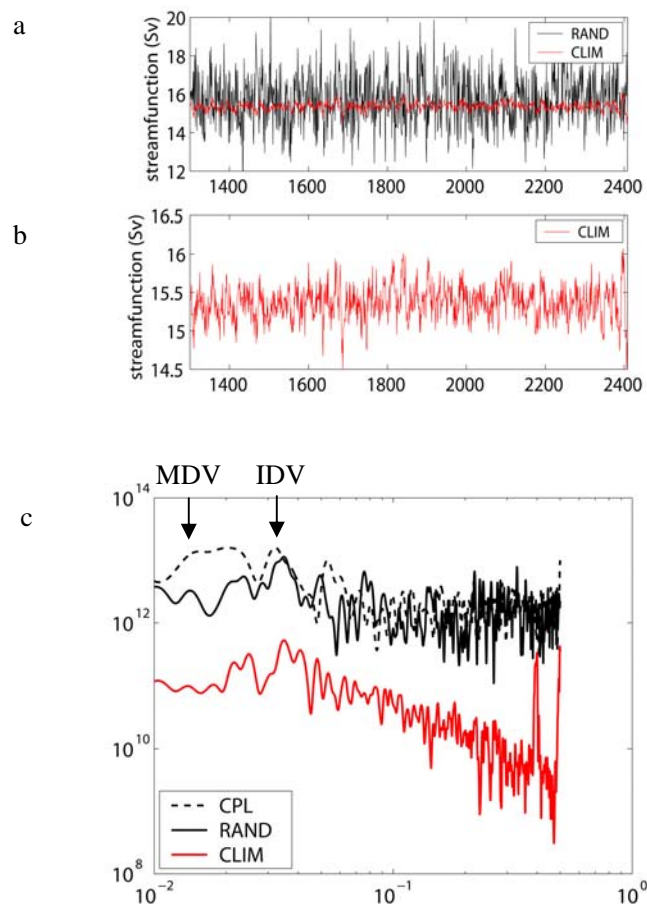
Fig. 4.7: time series (a,b) and spectrum (c) of the MOC time series at 30° N, 960m depth in CLIM (red line), RAND (black line). The spectrum of CPL is also shown in c) as the black dashed line. For spectrum calculation, 5 windows are used, with 3/4 of the window length as the overlapping length.
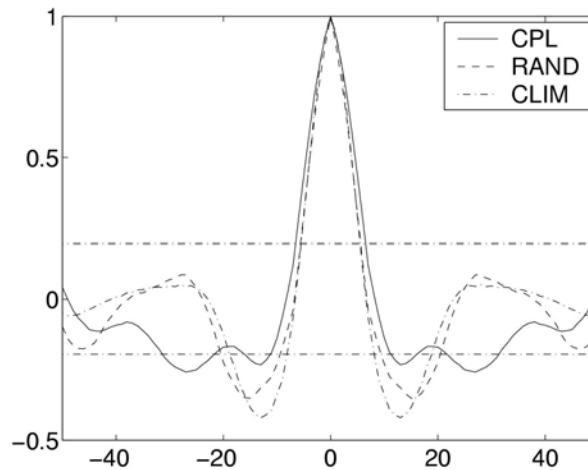
Fig 4.8: autocorrelation of 11 yrs running mean of the MOC indexes. The horizontal dashed line denotes 90% confidence level.

Our results provide a new view of the results from Delworth and Greatbatch (2000) (Fig. 4.9 from their Fig. 5). The oscillation exists in their fully coupled run is with a time scale of 70-100 yrs, however, the oscillation exists in their RANDOM (comparable to our RAND) is with a period of 50 yrs. Given the limited length of their experiments (400 years), the 50 and 70-100 scales cannot be differentiated, thus the shifting of the frequency associated with the 'multidecadal' variability of the MOC was not addressed in their work and they conclude that the 'multidecadal' oscillation of the MOC exists as an oceanic response to stochastic forcing. Our results suggest that the 50yr and 70-100 yr oscillation are possibly related to different physical modes. It is important to note that their model employs flux adjustment which reflects the model is incapable of simulating a proper mean state, which may be responsible for the much-damped low frequency variability in their experiment 'CLIM' (similar to our CLIM) .
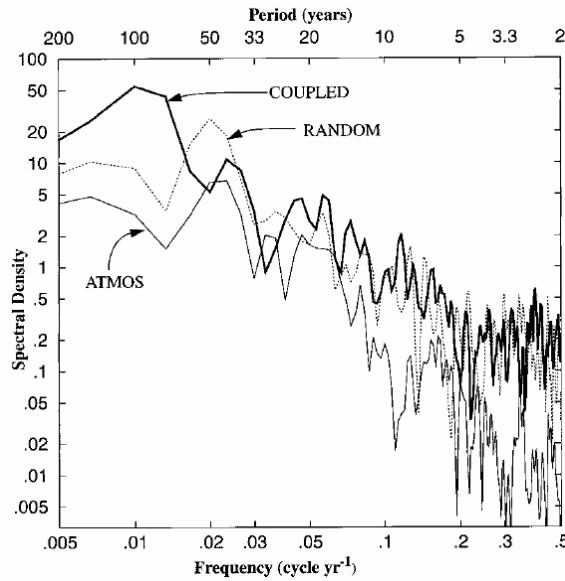
Fig 4.9: Spectra of time series of THC from three experiments, with 'COUPLED' similar to our CPL, 'RANDOM' similar to our RAND, and 'ATMOS' denoting the THC when the ocean model is driven by the low frequency variability of the atmosphere. There were 400 points in each of the input time series (discussed in Delworth and Greatbatch 2000, Fig. 5)

4.5. Role of surface wind stress

There are two notable differences between RAND and CLIM (Fig. 4.7c): firstly, RAND has a higher spectral energy level; Secondly, in RAND white noise dominates from years to one decade, whereas the MOC in CLIM shows decreasing spectrum with increasing frequency. Three additional experiments are designed (table 4.1) to investigate the role of surface fluxes leading to the difference. Each experiment is driven in a similar way as in RAND, but one of the surface flux items is set to climatology.

When the variability of the surface heat fluxes is excluded (RAND_CLIMHEAT), the MOC index has a mean of about 14.8 Sv, ~ 0.7 Sv smaller than the other experiments, whereas the exclusion of the variability of the surface freshwater fluxes (RAND_CLIMWATER) or wind stress (RAND_CLIMMOM) does not affect the simulated mean state of the MOC (Fig. 4.10a).

When the variability of surface wind stress is excluded, the MOC shows damped spectral energy from years to about one decade (Fig. 4.10b). Thus at this frequency range the wind stress dominates the MOC variability. But it can not fully explain the difference in the spectrum energy level between CLIM and experiment RAND_CLIMMOM, thus the other two surface fluxes also contribute positively to the lift-up of the MOC spectrum.
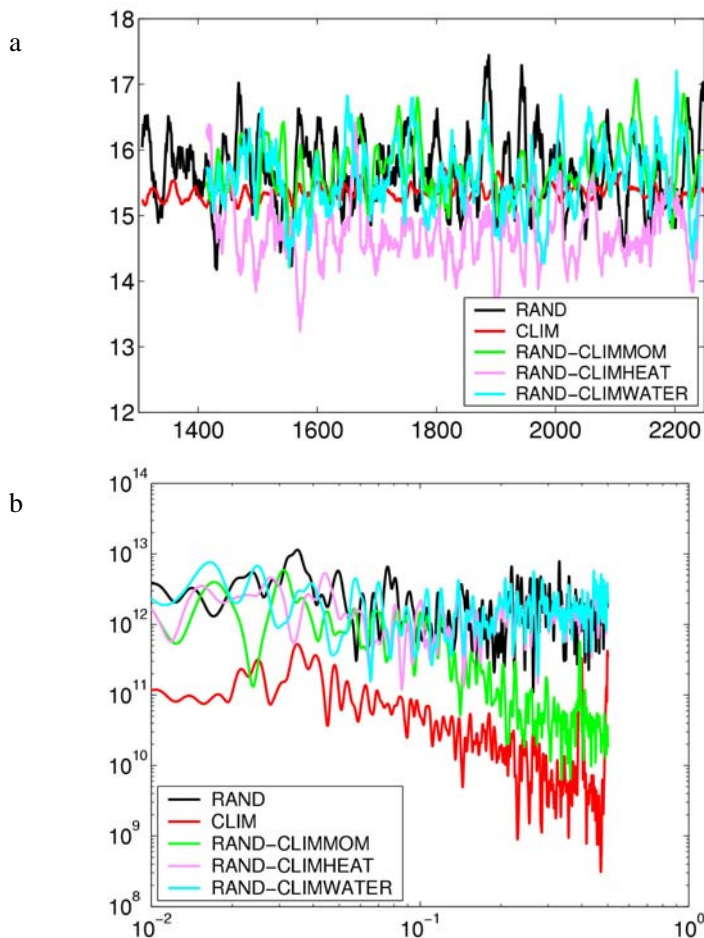
Fig 4.10: a) time series (with 11-yr running mean) and b) spectra of the MOC indices. Time series are detrended before spectrum calculation. 5 windows are used, with 3/4 of the window length as overlapping length.

At time scales longer than one decade, switch-off of one of the surface fluxes only shows minor impacts on the MOC spectrum (Fig. 4.10 a, b). Therefore three surface fluxes all contribute to the low frequency variability of the MOC; and damping of any one flux is not able to damp the low frequency variability of the MOC as in CLIM.

4.6. Summary and discussions

We present modeling results on the low-frequency variability of the MOC. Two different frequencies are identified, interdecadal variability ranging from 25-40 years (IDV) and multidecadal variability ranging from 45-80 years (MDV). The experiments we present here provide a relatively long sample of low-frequency oscillations. The IDV in all experiments and the MDV which exists only in the fully coupled run remain robust with different window length and overlapping window length used for spectrum calculation. IDV exists as an ocean self-sustained mode and MDV as an air-sea coupled mode.

Previous studies favored one of the three hypotheses: an ocean self-sustained mode, an oceanic response to stochastic forcing, and an air-sea coupled mode, to explain the low frequency variability of the MOC. Rivin and Tziperman (1997) suggest that the decadal/interdecadal climate variability is near the bifurcation point between the ocean self-sustained oscillation and the air-sea coupled mode. However, all these studies couldn't provide a satisfactory explanation for the wide-spread time scale associated with the low frequency MOC variability. Our results suggest that, in fact, several modes can coexist; further, there is possibly energy transfer between these modes which may be responsible for the varying time scales.

Wind stress plays an important role in shaping the spectrum of the MOC to white noise on the time scale from years to about one decade. This is because, at short time scales, the MOC reflects the projection in the vertical plane (after zonal averaging) of the topographic Sverdrup response of the ocean to the wind forcing (see Jayne and Marotzke 2001; Eden and Willebrand 2001), which determines the characteristic barotropic structure at high frequencies (not shown) and its white spectrum. At low frequencies, surface heat, freshwater and momentum fluxes all contribute to the high low-frequency white-noise plateau. Moreover, our results suggest that switch-off of any of the three surface fluxes

doesn't reproduce the damping spectrum in CLIM. Therefore, most likely these three items work together to lift-up the spectrum energy at the low frequency time scales, none of the three surface fluxes plays a dominant role as suggested by Weisse et al. (1994), Delworth and Greatbatch (2000).

Chapter 5

Interdecadal Variability as an ocean internal mode

5.1. Introduction

As shown in the last chapter, interdecadal variability of the MOC is maintained by ocean dynamics and multidecadal variability of the MOC as an atmosphere-ocean coupled mode. This chapter focuses on the interdecadal variability of the MOC.

Interdecadal variability of the MOC as an ocean internal mode has been found in previous studies (e. g., Weaver and Sarachik, 1991). They describe a near-decadal oscillation associated with the propagation of warm and saline water generated between the subtropic and subpolar gyre which initiates the anomaly development in ocean models forced with mixed boundary conditions. However, such boundary conditions have been shown to lead to idiosyncratic behavior (Zhang et al. 1993) and do not represent properly the large-scale atmosphere-ocean interactions (e.g., Capotondi and Saravanan 1996). In an idealized ocean basin forced by constant freshwater and heat fluxes, Greatbatch and Zhang (1995) successfully reproduce a decadal oscillation and reveal that a dynamical atmospheric component does not seem necessary to reproduce this decadal oscillation. The relatively long timescale of interdecadal oscillations compared to atmospheric thermal inertial timescales suggests a fundamental oceanic contribution.

Greatbatch and Peterson (1996) suggest that frictional boundary waves are sufficiently slowed along the weakly stratified polar boundaries, where convection takes place, to give rise to decadal periods. Huck et al. (1999) argue that, in stead of boundary-trapped waves, internal potential vorticity waves are important and that the phase difference is caused by both advection and adjustment, which is basically consistent with the results of Te Raa and Dijsktra (2002). This advective origin of the low frequency variability in the North Atlantic has also been noted by Marotzke (1990), Weaver and Sarachik

(1991), and Eden and Greatbatch (2003).

From the results of previous studies, it seems that an uncoupled, single-hemispheric ocean basin is the simplest model configuration in which interdecadal thermohaline variability resembling the one described by Delworth et al. (1993) can be found. TeRaa and Dijkstra (2002, 2003) used a hierarchy of models and found that the interdecadal variability controlled by geostrophic processes in their idealized model also exist in more complex models, thus established a good connection between the results from models with different complexity.

This variability is caused by a phase difference between changes in the meridional heat transport and a zonal redistribution of density anomalies. The oscillation is linked to the weakening and strengthening of the high–latitude deep water formation and the subsequent generation and removal of east-west steric height gradients which cause the MOC to intensify and weaken over decadal-to-multidecadal timescale. The variation of the east-west steric height gradient is associated with the propagation of temperature and salinity anomalies along the subpolar front to the eastern boundary. Horizontal advection sets the oscillation timescale which is given by the length of time it takes a particle to be advected from the western boundary to the eastern boundary along the subpolar front, and then, as subsurface flow, towards the polar boundary. Salinity, wind forcing, continental geometry, and bottom topography are all nonessential (Te Raa et al. 2004). The heat flux is sufficient to drive the variability, while the active salinity reduces the amplitude of the oscillations. This dominant role of surface heat fluxes has already been found in observations that temperature anomalies in the North Atlantic are often associated with salinity anomalies of the same sign, but the temperature influence on density prevails (e.g., McCartney et al. 1996). However, some numeric models have suggested the possibility that salinity may play a

dominant role (Delworth et al. 1993; Timmermann et al. 1998).

The purpose of this work is to investigate the ocean internal mode using the complex ocean model – MPIOM. We focus on the physical mechanism that leads to interdecadal oscillations in the North Atlantic region.

The chapter is organized as follows. A detailed discussion on IDV in the ocean model driven by climatological surface forcing (CLIM) is presented in section 5.2. Section 5.3 presents the results on the IDV in the ocean model driven by stochastic atmospheric forcing (RAND). We end this chapter with summary and conclusions in section 5.4.

5.2. Interdecadal variability in CLIM

In chapter 4 we have shown that IDV exists as an ocean internal mode. In this chapter, results from experiment CLIM are analyzed. A short description about the IDV in experiment RAND is also presented.

5.2.1 Dominant role of temperature

It is anticipated that fluctuations of the MOC are related to changes in the density, temperature and salinity structure of the North Atlantic. This relation is investigated by calculating linear regressions of the time series of density, thermal- and haline-component of density onto the MOC index at grid points in the Labrador Basin where the mean MLD in March exceeds 1200m (Fig. 5.1). These regressions are calculated at various lags in order to provide an evolution picture as the MOC varies. The regression coefficients are averaged horizontally and vertically over the selected ocean domain. The density anomalies lead the maximum MOC by 3 years, suggesting variation of the density induces changes of the MOC. The density anomalies attributable to temperature changes dominate the density changes, leading the MOC by ~ 2 yr, whereas the haline part of the density anomalies vary almost out of phase
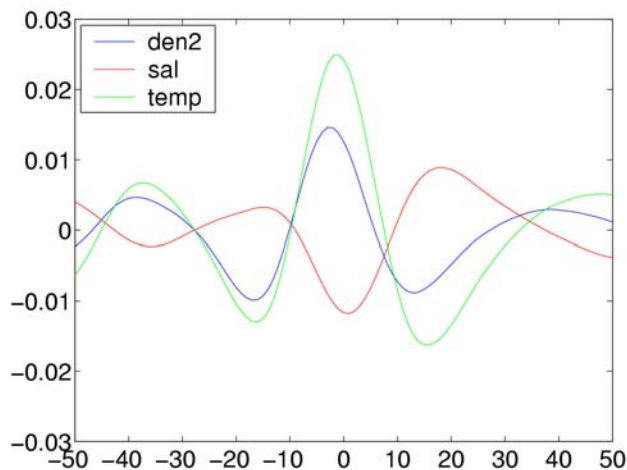
with the MOC, counteracting the thermal effects.

Fig. 5.1: regression coefficients between various quantities and the time series of the MOC index at 30° N in CLIM (kg/m^3 / Sv). The blue, red, and green line denotes the regression of potential density, its haline and thermal part onto the MOC index. The reference depth is at 2000 m. The regression coefficients were averaged vertically and horizontally over the region where the mean MLD in March larger than 1200m in the Labrador Sea. X-axis denotes time lags; positive lags mean the MOC leading.

To investigate whether the relative role of temperature and salinity varies with depth, the vertical structure of the density anomalies is shown by averaging the regression coefficients horizontally (Fig. 5.2). The density anomalies and its thermal parts are homogeneous over the upper 2000m (Fig. 5.2, left and middle panel), while the saline part has a baroclinic structure: fresh (saline) anomalies are capped by saline (fresh) anomalies in the upper 400m (Fig. 5.2, right panel). That is to say salinity's role differs with depth: at intermediate depths salinity weakens temperature-contributed density anomalies while near the surface it enhances the thermal effects. This out-of-phase vertical structure of salinity field is typical of deep convection events in which cold and fresh water moves down and relatively warm and saline deep water is brought up. For instance, near lag 0, strong deep convection brings more relatively saline water up to the surface and leads to the positive near-surface salinity
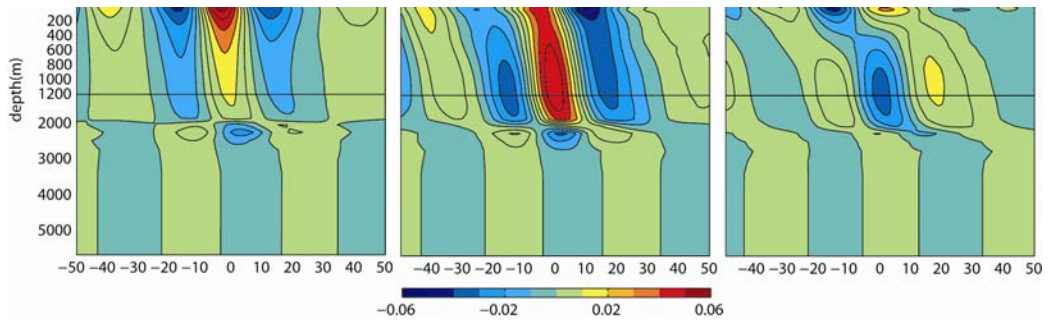
anomalies (Fig. 5.2, right panel).

Fig. 5.2: same as Fig. 5.1 but regression coefficients were averaged horizontally over the selected region. Full density anomalies (left), its thermal (middle) and haline (right) part.

5.2.2 Associated ocean condition

To display the 3-D picture of the ocean conditions associated with the MOC change on interdecadal time scale, the zonally averaged steamfunction, temperature and salinity are regressed onto the MOC index, shown in Fig. 5.3; the corresponding pattern of the upper ocean heat content and barotropic streamfunction are shown in Fig. 5.4. Here 'heat content' is defined as the mean temperature averaged over the upper 560m.

At lag -15, the MOC is at its minimum (Fig. 5.3a). The minimum MOC corresponds to the occupation of warm anomalies in the Labrador Sea seen near 60° N between 400-2000m. From lag -15 to lag 0, the MOC evolves to its maximum, which is accompanied by the invasion of cold and fresh anomalies into the Labrador Sea (Fig. 5.3b, c). At lag 0, warm and saline anomalies appear between 48° N and 75° N near the surface, while cold and fresh anomalies occupy the intermediate depth corresponding to the maximum MOC (Fig. 5.3). The ensuing weakening of the MOC from lag 0 to lag 15 is accompanied by the downward propagation of warm and saline anomalies (Fig. 5.3b, c)
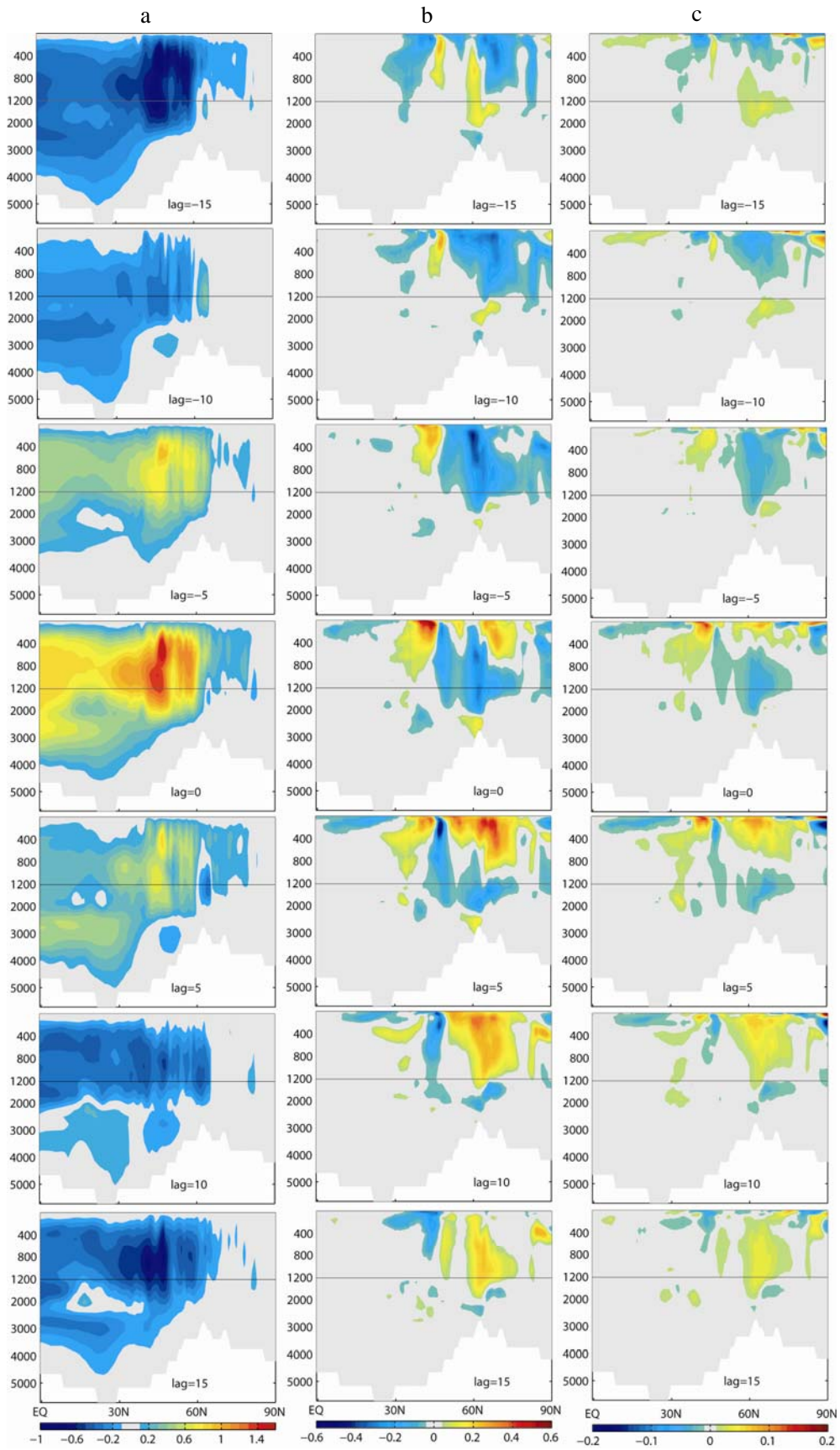
Fig. 5.3: regression coefficient of zonally averaged a) streamfunction (Sv/Sv), b) temperature (°C/Sv), and c) salinity (psu/Sv) in the Atlantic onto the MOC index.

a   b

Fig. 5.4: Regression coefficient of a) the heat content in the upper 560m and b) barotropic streamfunction onto the MOC index (Units: C/Sv and Sv per Sv). Contour line is the long term mean barotropic streamfunction. The interval is every 10 Sv.

The recovery of the MOC from its minimum at lag -15 is accompanied by the eastward propagation of warm anomalies along the subpolar front (Fig. 5.4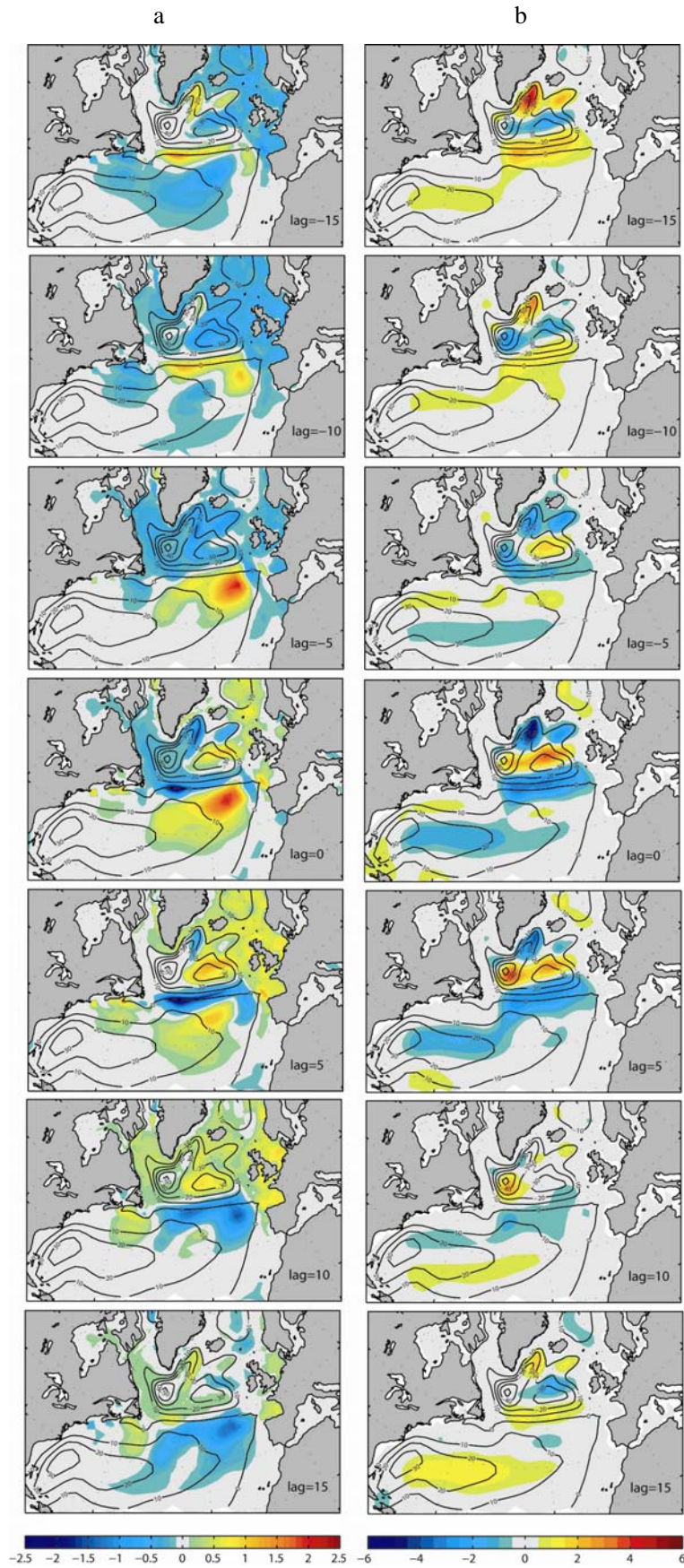a). The warm anomalies accumulate in the eastern subtropical basin, indicating weakened northward heat transport manifested as the large-scale cooling in the subpolar basin. Along the subpolar front, the eastward propagating warm anomalies are accompanied by an anomalous anticyclone across the mean zero barotropic streamfunction line (Fig. 5.4b), leading to a northward shift of the North Atlantic Current (NAC) axis (not shown). When cold anomalies appear east of Newfoundland at lag -5 and propagate eastward, they are surrounded by anomalous cyclone corresponding to a southward shift of the NAC axis (not shown). From lag 0 to lag 15 warm anomalies are released from the eastern subtropical basin and spread to the subpolar basin and finally to the Labrador Basin (Fig. 5.4a) leading to the weakening of the MOC (Fig. 5.3a). And one oscillation cycle is completed.

5.2.3 Geostrophic balance

The large-scale variation of the MOC is controlled by geostrophic relation (Colin de Verdiere and Huck 1999; Te Raa and Dijkstra 2002, 2003). To illustrate this relation, two density gradient indices are computed, Dns and Dew, indicating the north-south and east-west density gradient respectively. Density indices are computed over the following areas respectively, one located in the Labrador basin (Dn), one near the zonal band centered at 30° S in the south Atlantic (Ds), one near the British Islands (De), and one near Newfoundland (Dw), by averaging the density over each of the selected area and vertically over the upper 2000 m. Dn minus Ds equals Dns, and De minus Dw equals Dew. The density gradients are correlated with the MOC index, shown in Fig. 5.5. Dns leads the MOC by about 2 years; Dew is almost out of phase, but slightly lags behind the MOC change.
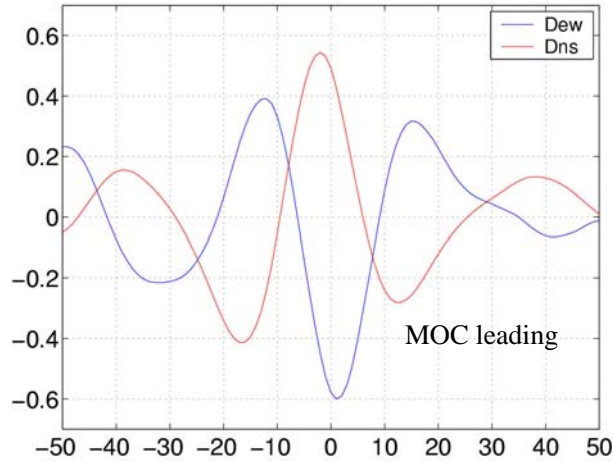
Fig. 5.5: Time-lag correlation of the east-west & north-south density gradient (Dew and Dns) with the MOC index.

In order to provide a picture of the associated changes in ocean mass transport, a north-south section across the NAC is chosen (Fig. 5.6) to capture the changes of the NAC as an indicator of the zonal streamfunction. Through this north-south section, there are two water masses passing which we define as the upper water (UW) with $\sigma_2 > 1036.4$ kg/m^3 and the Labrador Sea Water (LSW) with $\sigma_2 \sim [1036.4\ 1036.7]$ kg/m^3. The mean thickness of the two water masses and characteristic current patterns are shown in Fig. 5.6. Note that the UW may be absent in certain regions, such as the convection center in the Labrador Sea where the LSW is directly exposed to the overlying atmosphere. A detailed description of the mean state of the water masses in Fig. 5.6 follows in section 5.2.4.

The mean potential temperature and u-velocity across the selected section is given in Fig. 5.7. Two gray lines separate the water mass to three classes: near the surface, it is occupied by warm UW, in the intermediate layer it is featured as cold subpolar water, mainly the LSW; at the bottom, it is the lower North Atlantic Deep Water, mainly the overflow waters.
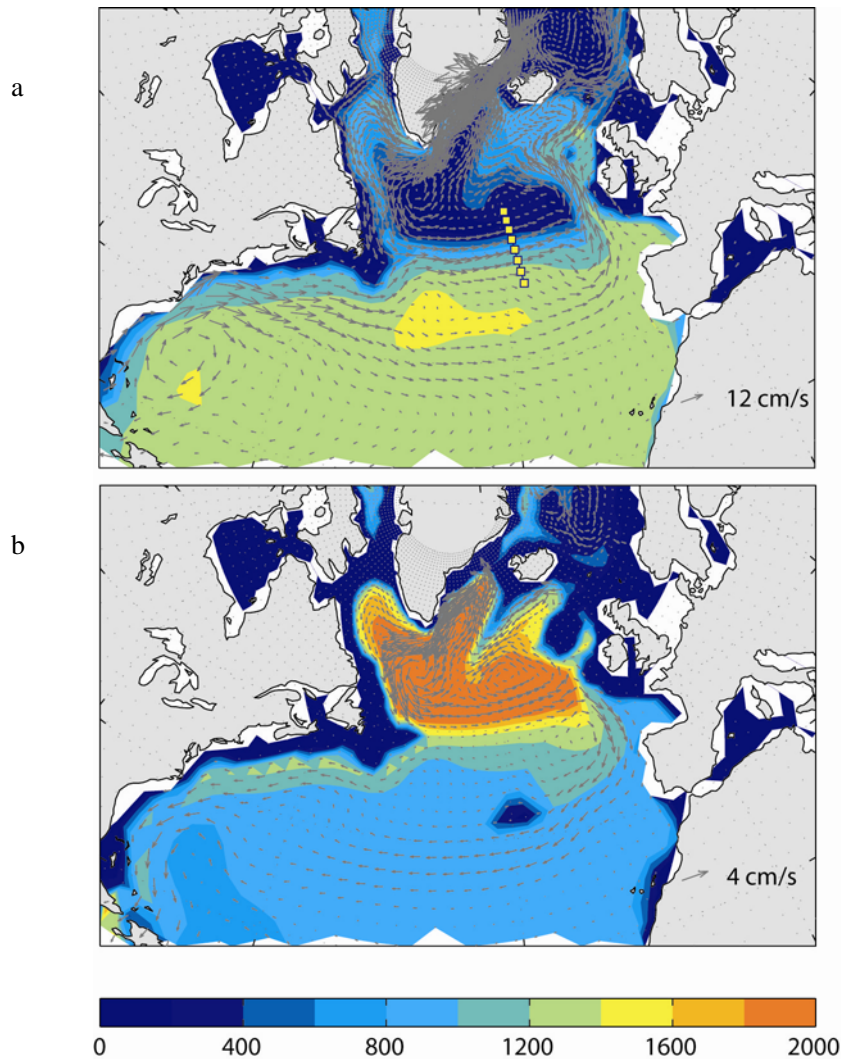
Fig.5.6: mean thickness (shade) of a) Upper Water and b) LSW (Units: m). Vectors shown are mean velocity field at 47m (upper panel) and 1525m (lower panel) (Units: cm/s). The yellow square in the upper panel denotes the selected section.

In the UW layer the NAC enters the section from its southern part, occupying the upper 1500m. The NAC is characterized by temperature higher than 8° C and strong eastward velocity with a maximum about 10 cm/s at the surface. At the northern part of this section, a mixture of cold subpolar water and the NAC flows through. Underneath the UW is the LSW, most of which moves eastward and reaches the eastern North Atlantic boundary. There the LSW splits into two branches entering the subpolar gyre and the subtropic gyre respectively (refer to the vector field in Fig. 5.6b). Part of the branch going to the subtropic gyre goes under the NAC and moves westward, separated from

the eastward NAC by the zero u-velocity line. The LSW is distinguished from the warm NAC by homogeneous temperature between 6° and 7°C. It should be noted that the characteristic physical attributes of water masses (such as temperature and density) are not meant to match the range in observational data (e. g., Pickart et al. 2002), because the experiment CLIM is an idealized case with the ocean model driven by climatological surface fluxes.
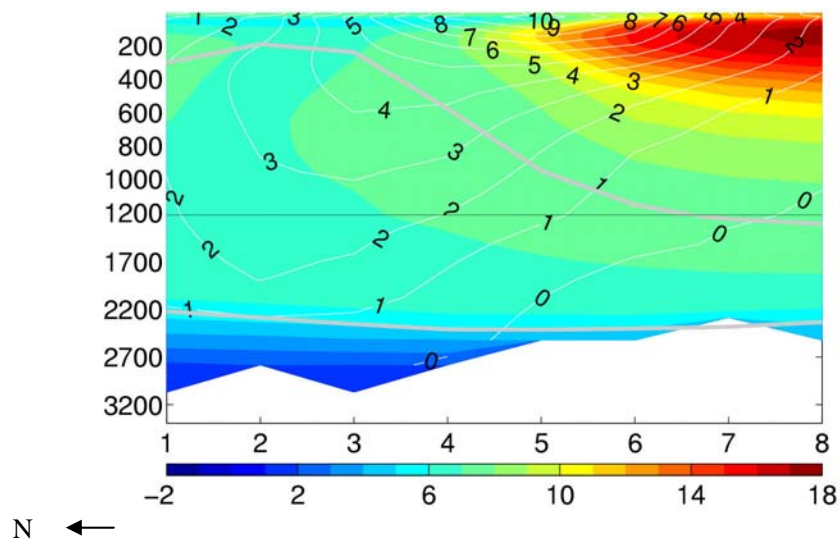

Fig. 5.7: mean potential temperature (shaded, unit: $^{\circ}$C) at the selected section. White contour is the mean zonal velocity (white contour, Units: cm/s), positive values mean eastward. Gray lines indicate the interface between the UW, the LSW, and the lower North Atlantic Deep Water. The x-axis interval does not correspond to the real distance between the selected points.
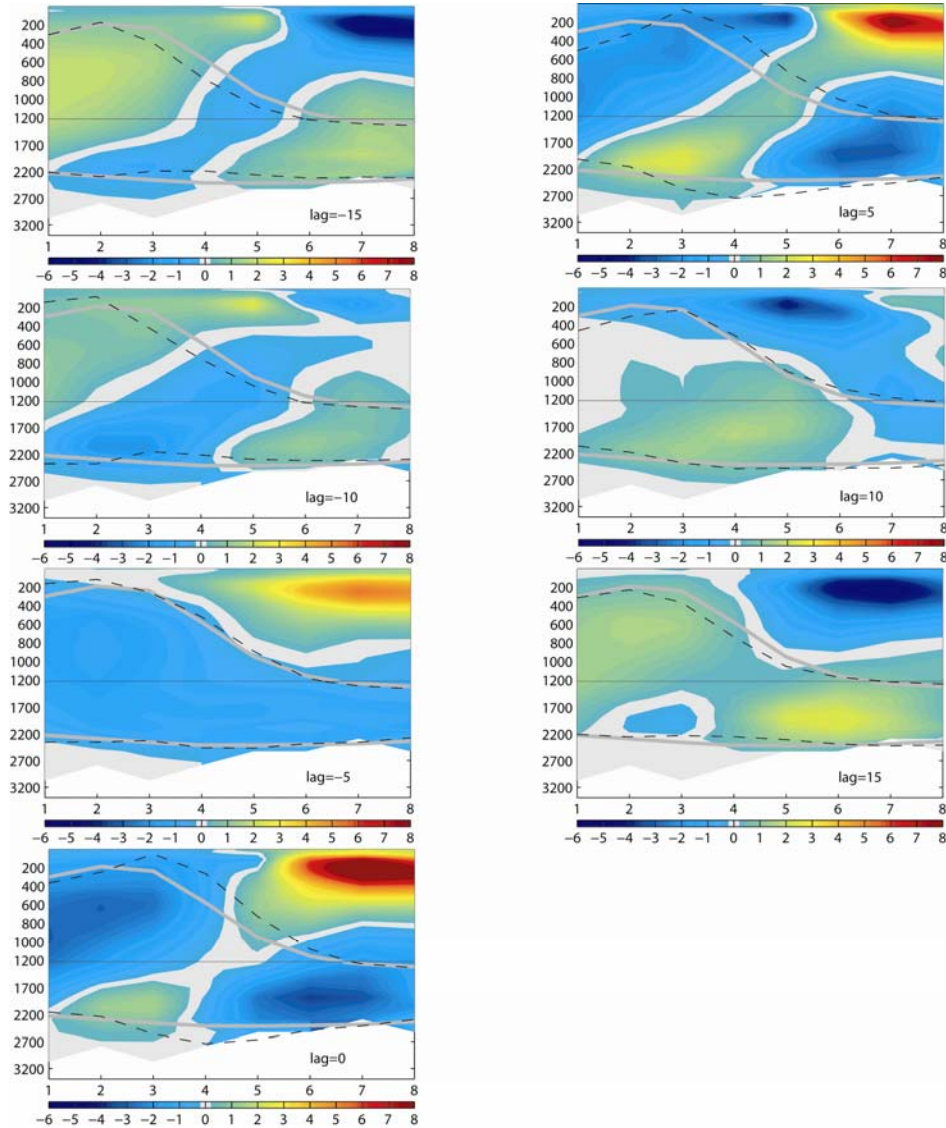
Fig. 5.8: Regressions coefficients of the advective heat transport through the selected section (Fig. 5.6a, squared dots) onto the MOC index. From up to down, the gray lines are the mean position of the UW-LSW interface and the LSW lower boundary. The black dash line is the mean position of the interface plus the associated depth change at interdecadal scale corresponding to per Sv change in the MOC. The x-axis interval does not correspond to the real distance between the selected points.

The advective heat transport through the selected section (Fig. 5.6a) is regressed onto the MOC index (Fig. 5.8), which resembles the corresponding mass transport pattern, indicating that this pattern is mainly contributed by u-velocity anomalies. From lag -15 to lag 0, the heat transport carried by the NAC evolves from its minimum to its maximum, accompanied by the

intensification of the slope of the UW-LSW interface (dashed line). At the same time, the eastward transport of the LSW weakens. At lag -15, the NAC is weak and the eastward LSW transport is strong (Fig. 5.8), corresponding to the anomalous anticyclone structure across the subpolar front (Fig. 5.4b). This anticyclone structure extends down to 1700m; below 1700m, a cyclonic structure is seen, indicating weakening of the eastward transport by the lower LSW layer and strengthening of the returning (westward) LSW. At lag 0, when the NAC transport reaches its maximum and the eastward LSW transport reduces, corresponding to an anomalous cyclone structure across the subpolar front (Fig. 5.4b); at the same time an anticyclone structure appears below 1700m. From lag 0 to lag 15, the NAC transport weakens and the eastward LSW transport strengthens; and the anticyclone structure below 1700m is gradually replaced by an anomalous cyclone.

The adjustment of the transport through this selected section is tightly related to the changes of Dns reflecting the geostrophic relation. At lag -15, the MOC is in its minimum. There are still a portion of warm anomalies in the Labrador basin (lag -15, Fig. 5.4a); and Dns reaches its minimum (Fig. 5.5). Dns increases when the warm anomalies in the Labrador Sea are replaced by cold anomalies from the eastern subpolar basin and the GIN Sea (from lag -15 to lag 0). This is in geostrophic balance with the enhancement of the NAC transport which lasts from lag -15 to lag 0 (Fig. 5.8). The strong NAC carries a large amount of heat to the eastern North Atlantic, reducing the density in the eastern basin (De). When cold anomalies from the Labrador Sea enter east of Newfoundland, Dew reaches its maximum (Dw at its maximum due to cold anomalies and De at its minimum due to the warm anomalies), leading to anomalous strong northward transport, manifested as speeding-up of the MOC (from lag -15 to lag 0, Fig. 5.3a) and the following large-scale warming of the subpolar gyre (from lag 0 to lag 10, Fig. 5.4). Subsequently, the subpolar gyre carries the warm anomalies into the Labrador basin and moves cold anomalies

to the eastern North Atlantic along the subpolar front, responsible for the decreasing Dns and the increasing Dew. The opposite half of the cycle starts.

Maximum Dns leads the minimum Dew by about 4 years (Fig. 5.5), corresponding to the advection time of the LSW from the convective center in the Labrador basin to near Newfoundland. This time is consistent with the time estimated in other models (Cooper and Gordon, 2002; Eden and Greatbatch, 2003).

In summary, the interdecadal cycle of the MOC is associated with a geostrophic advective process. The propagation of temperature anomalies along the subpolar front is tightly related to the change of Dew which controls the northward heat transport; the westward propagation of temperature anomalies in the subpolar gyre is crucial to the transition of Dns which controls the changes of the eastward NAC transport. This result provides encouraging support to results drawn from less complex models (e. g., Huck and Vallis 2001; Te Raa and Dijkstra 2002, 2003).

5.2.4 Interaction between water masses

The interaction between the UW and the LSW are tightly related to the interdecadal variability of the MOC. The mean thickness and current patterns at 47m and 1525m are plotted in Fig. 5.6.

The UW originates from the warm subtropics (Fig. 5.6a). It has two branches in the subtropical North Atlantic, the Azores Current and the NAC which leaves the coast southeast of the Grand Banks and turns eastward. The UW loses heat to the overlying atmosphere on its way along the subpolar gyre and becomes heavier and denser. This cooling process is crucial to the preconditioning of the LSW (McCartney and Talley 1982; Curry and McCartney 2001). Note that the LSW outcrops in central Irminger Sea and

central Labrador Basin where the UW is not present, thus the UW is confined only within the boundary region.

The simulated LSW spreads over the entire subpolar basin (Fig. 5.6b). It splits into two branches at the exit of the Labrador Basin near Newfoundland, one along the deep western boundary corresponding to the classical Deep Western Boundary Current (DWBC), and the other entering the eastern North Atlantic basin. The latter splits into two parts, one returning to the subpolar gyre and the other turning southward from both sides of the Middle Atlantic Ridge (MAR), which can be seen clearly from the integrated transport over the LSW layer (not shown). It has been suggested that the interaction between the LSW and the NAC near the crossover (where the LSW flows below the NAC) might provide a source for low frequency variability (Spall et al. 1996 a, b). The simulated two pathways of the LSW, one along the DWBC and the other entering the eastern North Atlantic, are consistent with observational data (e.g., Schott et al. 2004). However, compared to the observations (Schott et al. 2004), the branch entering the eastern North Atlantic travels too far eastward in our model. This is a common shortcoming of coarse resolution models.
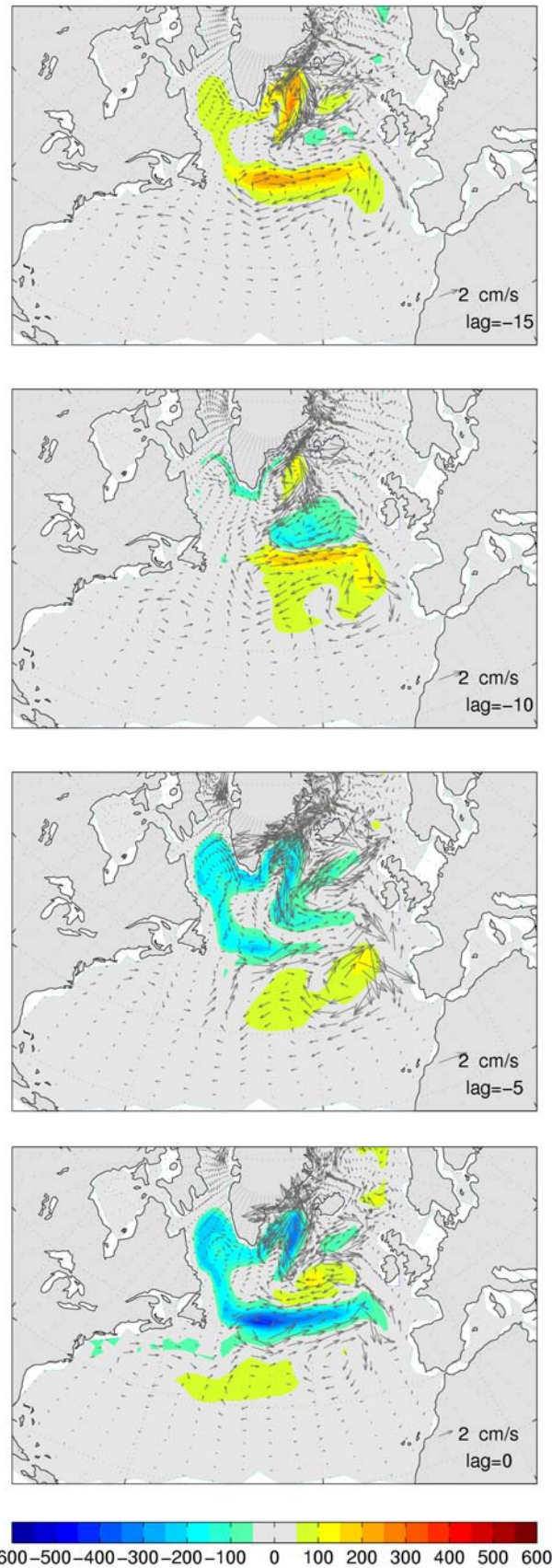
Fig.5.9a: regression coefficient of upper water thickness (shade, Units: m/Sv) and velocity at 47m (vector, Units: cm/s / Sv) onto the MOC index. Positive lags (at the lower right corner) mean the MOC index leading.
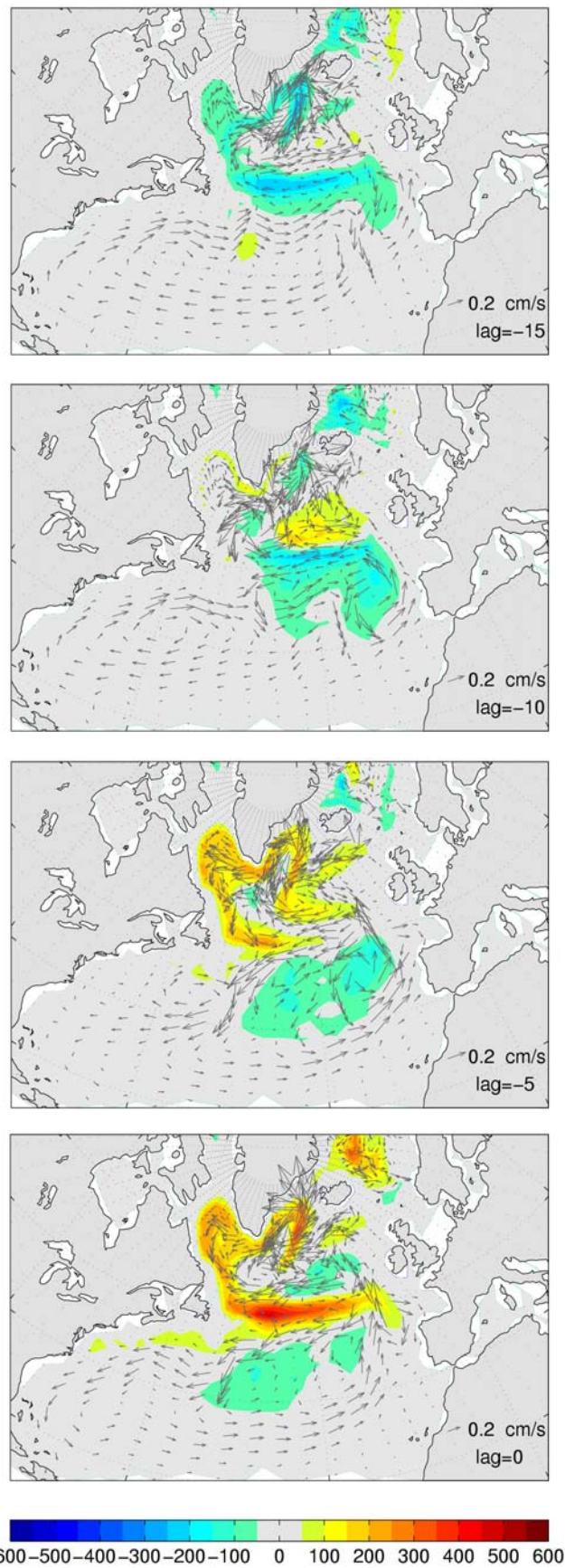
Fig.5.9b: same as Fig. 5.9a but for the LSW layer and velocity at 1525m.

The thickness of the UW and LSW layer are regressed onto the MOC index (Fig. 5.9a). The UW thickness anomalies (Fig. 5.9a) have a similar spatial pattern to the temperature anomalies (Fig. 5.4a): at lag -15, the UW expands in the Labrador basin and along the subpolar front where the warm anomalies prevail. The UW then experiences thinning from lag -15 to lag 0 (Fig. 5.9a) when cold anomalies resume control over the subpolar basin and the subpolar front region (Fig. 5.4a). The warm (cold) anomalies along the subpolar front are surrounded by anticyclonic (cyclonic) current anomalies.

The changes in the LSW (Fig. 5.9b) are of opposite sign to the one in the UW layer: expanding UW vs. thinning LSW, and anticyclonic (cyclonic) current anomalies in the UW layer vs. cyclonic (anticyclonic) anomalies in the LSW layer across the subpolar front, consistent with the picture shown in Fig. 5.8. This tight connection between the LSW and the UW thickness is suggested associated with the changes in the obduction rate (Haines and Old 2005). There are also associated changes in the LSW branch returning southward through both sides of the MAR: at lag -15 when the LSW thins across the subpolar front, more water goes via the eastern side of the MAR and less water via the western side of the MAR, indicated by the southwestward current anomalies east to the MAR and northeastward current anomalies west to the MAR.

We notice that the thickness anomalies are enhanced along the subpolar front (Fig. 5.9a), consistent with the enhanced temperature anomalies along the subpolar front (Fig. 5.4a). This enhancement is a result of local ocean dynamics, which is discussed in the following section (section 5.2.5).

It is important to point out that the transition from anticyclonic to cyclonic anomalies in the barotropic streamfunction from lag -10 to lag -5 (Fig. 5.4b) can be clearly seen by the reversed direction (from southward to northward) of the current anomalies near British Islands (Fig. 5.9a). This reversal of the

direction of the current anomalies corresponds to the transition of Dew from its positive to negative phase (Fig. 5.5), which leads to the release of the warm anomalies into the subpolar basin (Fig. 5.4a).

In summary, water masses interaction in the subpolar gyre is involved on interdecadal scales: when the surface subpolar gyre experiences cooling (warming), the UW layer experiences thinning (expanding) and the LSW expands (thins). The temperature and water mass thickness anomalies are enhanced along the subpolar front.

5.2.5 Ocean dynamics along the subpolar front

One noticeable feature in Fig. 5.4a and Fig. 5.9 is that temperature and thickness anomalies of both the UW and the LSW layer are enhanced along the subpolar front. This is contributed by the varying production of the LSW and the resulting current adjustment near its upper and lower boundary. For instance, during weak MOC, the LSW layer becomes thinner as a result of reduced deep water formation. It appears near the 'crossover' with lowering of the UW-LSW interface and the upward shoaling of the lower LSW boundary (denoted by the black dashed line at lag -15, Fig. 5.8). Changes in the slopes of the interfaces result in an anomalous anticyclone near the UW-LSW interface and an anomalous cyclone near the lower LSW boundary. The warm anomalies accompanied with reduced LSW formation are enhanced by entrainment of warm water from the warm NAC, and at the same time, being isolated from mixing with cold subpolar water by the anticyclone. Thus the strong north-south temperature gradient across the subpolar front favors the amplification of the LSW temperature anomalies.

The current anomalies generated in the lower LSW are of comparable amplitude to the mean speed at this depth (0-1 cm/s, Fig. 5.7 and Fig 5.9b) and hence very important in determining the eastward propagation of

temperature anomalies observed in the upper ocean (Fig. 5.4a), consequently the transition of the east-west density gradient.

The lower current anomalies are also important in influencing the preferred pathway of the LSW. An anomalous cyclone reduces mass transport from the western side of the MAR and consequently more water take the path from the eastern side of the MAR (Fig. 5.9b, at lag -15). In contrast, when an anomalous anticyclone is generated to compensate the cold-core cyclone in the upper ocean, it spins more water to the western side of the MAR (Fig. 5.9b, at lag 0).

5.2.6 Roles of the GIN Sea

In experiment CLIM, the Denmark Strait overflow exhibits considerable 30-yr oscillation (Fig. 5.10). To evaluate whether the oscillation of the MOC can be traced back to the overflow changes, one additional experiment CLIM_RESTGIN is designed. The ocean-only model is driven with climatology surface fluxes as in CLIM, but the temperature and salinity in the GIN Sea are restored to their 3-d climatological fields. In this manner, the variability of the overflows is suppressed according to the hydraulic theory (Whitehead et al. 1974; Whitehead 1989; Nikolopoulos et al. 2003). At the same time, the pathway of temperature anomalies through the GIN Sea entering the Labrador Sea is blocked. This experiment starts from the ocean condition at the end of year 708 from CPL and is ~ 950 years long. The last 560 years are shown (Fig. 5.11).
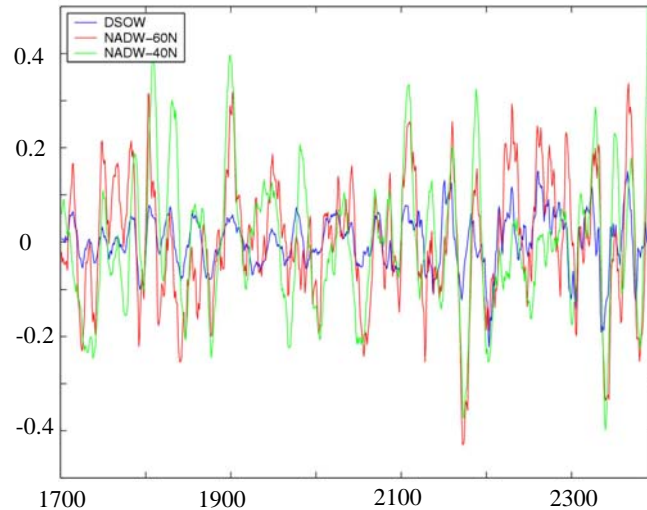
Fig.5.10: Time series of the Denmark Strait overflow and the zonally averaged streamfunction at 60° N and 40° N in CLIM (Sv). An 11-yr running mean is applied. The blue, red and green lines denote the mass transport carried by Denmark Strait overflow, the zonally averaged streamfunction at 960m but at 60° N and 40° N respectively.

With the 3-d temperature and salinity restoring in the GIN Sea, the MOC index has a mean of 18.5 Sv, ~ 3 Sv larger than CLIM (not shown). The simulated interdecadal variability is of comparable amplitude to that in CLIM (Fig. 5.11). The associated temperature anomalies resemble those in CLIM (not shown). This suggests that the changes in the overflows are not essential for the IDV of the MOC as long as the dynamics in the subpolar basin including the subpolar front area is allowed to evolve freely.
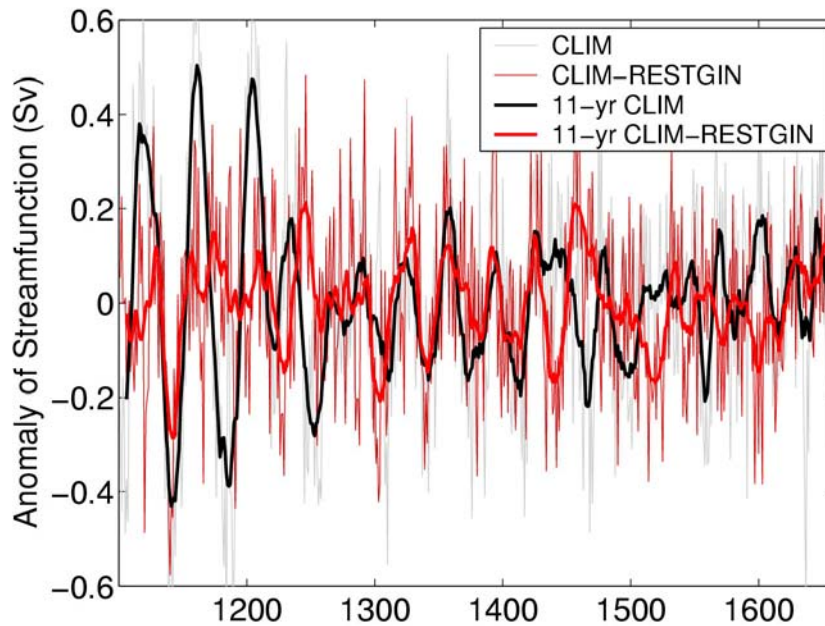
Fig. 5.11: time series of the anomaly of the MOC index from CLIM and CLIM_RESTGIN. Thick lines are the 11-yr running mean of the corresponding thin lines.

At the end, one thing to note is that in CLIM there is an out-of-phase relation in the deep convection between the Labrador Sea and the GIN Sea (Fig. 5.12). This is due to different advection time it takes the temperature anomalies to occupy the two basins. This result suggests that the ocean is able to contribute to the out-of-phase behavior in the deep convection between the GIN Sea and the Labrador Sea, which is a supplement of the results of Dickson et al. (1993). They find that the NAO minimum increases the accession of freshwater surface water to the Labrador Sea while minimizing its winter storminess and cyclonic circulation leading to the reduced winter heat-loss and suppressed convection. However, the NAO minimum leads to enhanced ventilation in the GIN Sea. Thus they suggest that the NAO is responsible for the out-of-phase between the deep convection in the GIN Sea and the Labrador Sea.
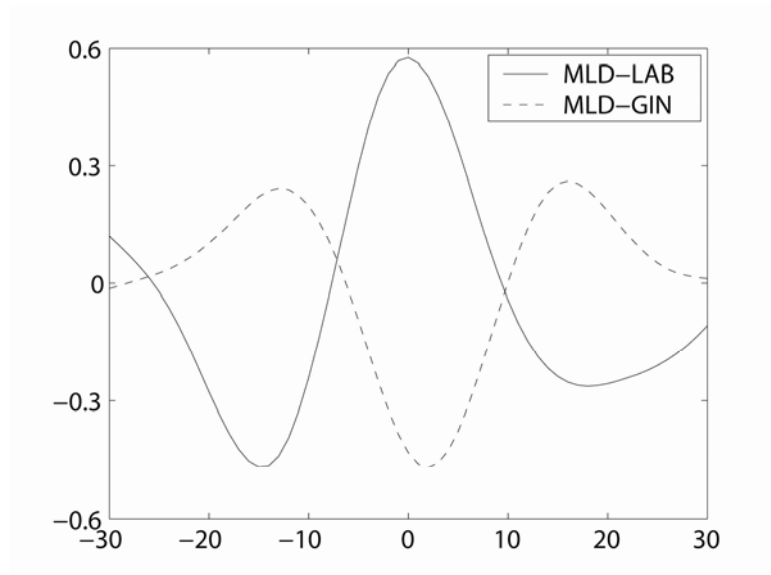
Fig. 5.12: time-lag correlation between the MLD in the GIN Sea and the Labrador Sea onto the MOC index in CLIM.

5.2.7 Interdecadal Variability in the South Atlantic

We have shown the interdecadal variability of the MOC as a geostrophic advective process with active interaction between different water masses. We notice that the associated temperature anomalies are confined to north of 30° N, however, the associated MOC anomalies spread to the whole Atlantic basin, with a variation center at 3000m deep, 30° S (not shown). This involves the interaction between the North Atlantic Deep Water (NADW) and the Antarctic Bottom Water (AABW) through the up- and down-ward displacement of the NADW-AABW interface (Fig. 5.13): strong NADW is accompanied by downward displacement of the interface, indicating weakening of the AABW, and vice versa. This provides evidence that the low frequency variability of the NADW has an impact on the AABW by the up- and down-ward displacement of the AABW-NADW interface. This result is reminiscent of those of Yin et al. (1992). They use a four-box ocean model to investigate the interaction between the deep water masses and find that changes in the formation rate of a deep-water source alter cross-isopycnal flows, especially along the related circulation route, thus altering the extent that the other

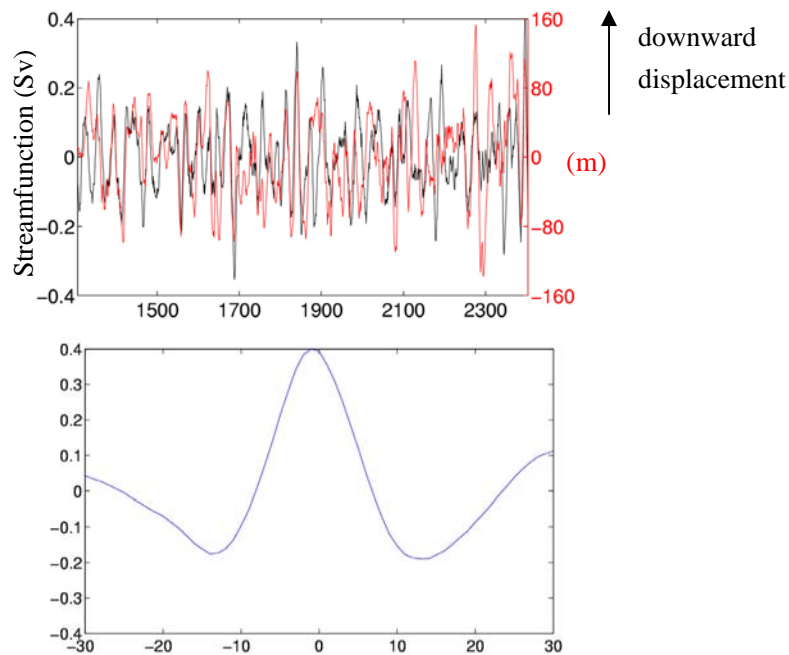source can travel before they detrain significantly.

Fig. 5.13: a) anomaly of the depth of zero-meridional streamfunction at 30S (red line) in CLIM and b) its correlation with the MOC index. The black line in a) is the MOC index, referred to the left y-axis, while the depth change is referred to the right y-axis. An 11-yr running mean is applied.

5.3. Interdecadal Variability in RAND

Interdecadal oscillation exists also in RAND, with bigger amplitude (Chapter-4, Fig. 4.7). To show that the same mechanism of the IDV found in CLIM also works in RAND, the same analyses are done with RAND. Some results are shown in Fig. 5.14-16 for comparison.
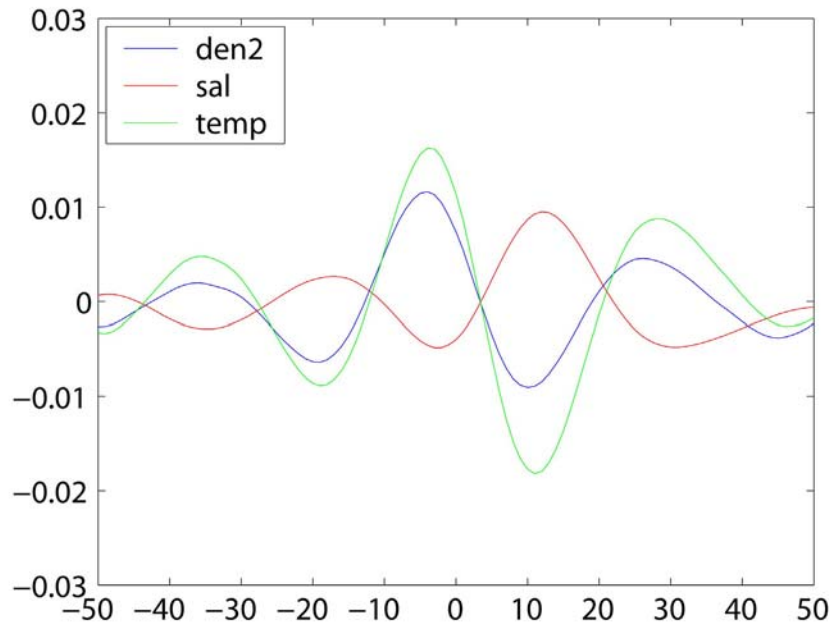
Fig. 5.14: same as Fig. 5.1 but for RAND

Fig. 5.14 shows that density anomalies lead the MOC variation by a few years; temperature dominates the density anomalies; salinity plays against thermal effects. The density anomalies and its thermal part lead the MOC index by about 5 years, slightly different from those in CLIM (Fig. 5.1).

The strengthening of the MOC from lag -15 to lag 0 is accompanied by cold and fresh anomalies taking over the Labrador Sea (Fig. 5.15). The large-scale density gradients (Fig. 5.16) show a similar behavior as in CLIM, not discussed in detail here. Thus the IDV in experiment RAND shares the same physical characteristics as the one in CLIM and is related to changes in the large-scale density gradients and the oceanic adjustment through geostrophic processes.
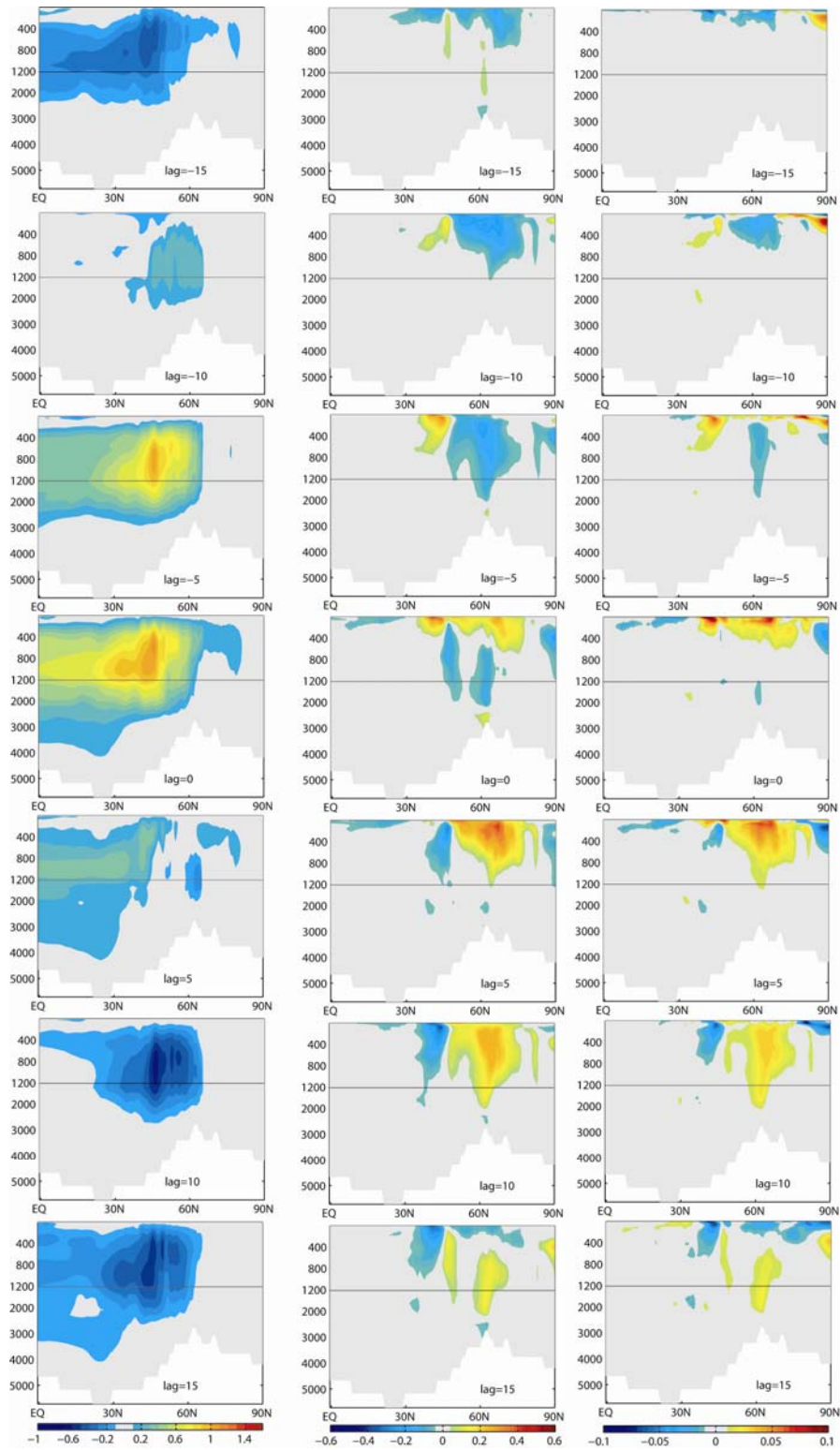
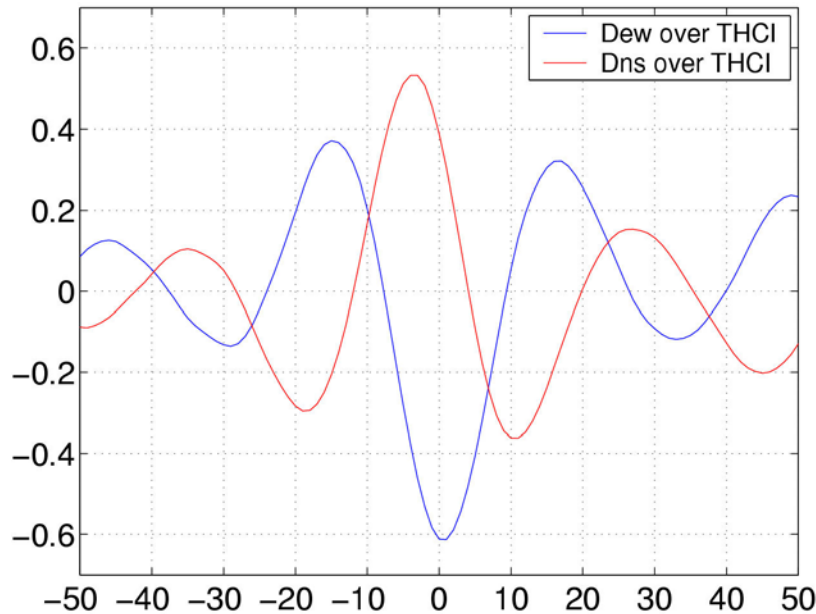Fig. 5.15: same as Fig. 5.3 but for RAND

Fig. 5.16: same as Fig.5.5 but for RAND

5.4. Summary and discussions

We present in this chapter the interdecadal variability of the MOC as an ocean internal mode, controlled by geostrophic processes. The IDV is related to the generation and removal of east-west density anomalies induced by temperature anomalies and increasing and decreasing of the northward heat transport which leads to weakening and strengthening of the deep convection in the deep water formation sites. Salinity changes oppose the temperature effects but play a subordinate role. This result provides an encouraging support to results from less complex models (e. g., Te Raa and Dijkstra 2002, 2003).

The IDV can be divided into a slow and a fast advection process besides the deep convection process in the Labrador Basin. The 'fast advection process' is related to the propagation of temperature anomalies from the eastern North Atlantic subtropics to the Labrador Basin, which are mainly carried by the surface current (~ upper 600m, not shown). In this process, the UW thickness changes out of phase with the LSW thickness. These thickness changes of the

UW and LSW are most likely associated with the temperature-induced circulation changes which lead to changes in the obduction from the LSW to the UW, as suggested by Haines and Old (2005). Further investigation of these connections is needed to fully understand the causal links.

The 'slow advection' corresponds to the process in which the temperature anomalies carried by the LSW join the NAC from east of Newfoundland and continue eastward. It takes approximately 4 years for the LSW-related temperature anomalies to reach east of Newfoundland, suggested by the time lag of maximum of Dew behind the minimum Dns (Fig. 5.5). The withdrawal of the temperature anomalies out of the Labrador Sea corresponds to changes in the north-south density gradient; their eastward propagation along the subpolar front determines the phase of the east-west density gradient. The temperature anomalies at the surface in Fig. 5.4a are a manifestation of the temperature anomalies in the deep LSW layer, thus the time scale of the surface temperature anomalies is determined by the slow movement of the lower LSW. This process is also observed in Hadley Centre coupled climate model (Cooper and Gordon 2002).

The interaction between the LSW and the NAC along the subpolar front is tightly related to the current anomalies which control the anomalous northward heat transport. For instance, from lag -15 to lag -5, warm anomalies accumulating near the eastern boundary of the North Atlantic induce anticyclonic current anomalies (Fig. 5.9a). During this period the current anomalies near the British Islands direct southward, which suggests reduced northward heat transport and accounts for the large-scale cooling in the subpolar gyre (Fig. 5.4). When the cold anomalies carried by the LSW reach the eastern boundary of the North Atlantic at around lag -5, the induced cyclonic current anomalies tend to direct northward the accumulated warm anomalies from the eastern subtropics, leading to the spreading of warm

signals in the subpolar gyre (Fig. 5.4a at lag 0).

The NAC responds to the varying thickness of the LSW by shifting north-/south-ward. This shifting has been observed in reality: Hátún et al. (2005) have noticed that the shift of the subpolar frontal zone is associated with changes of the northward salinity transport by the NAC which finally influences the intensity of the thermohaline circulation. As suggested by our results and previous studies (Spall et al.,1996a, b; Haines and Old, 2005), this swing of the subpolar frontal zone may reflect the interaction, mixing and transformation between the NAC and the LSW. Whether this interaction exists in reality needs to be further verified. However, our result suggests the possibility that information of the state of the MOC may be deduced from the knowledge of the water mass characteristics near the subpolar frontal zone which can be easily observed.

The current anomalies in the lower depth of the LSW along the subpolar front have a potential to influence the preferred pathway of the southward LSW. Corresponding to the anomalous cyclone (anticyclone) at the lower LSW layer, less (more) water is spun to the western part of the MAR (Fig. 5.9b). Though the simulated pathway of the LSW in our model is far too eastward, it does not hinder the same mechanism from taking effects in more realistic circumstances, such as near the Grand Banks where the deep water splits into one branch moving southward along the western boundary and the other branch entering the eastern North Atlantic basin (Fischer and Schott 2002).

The presence of the same mechanism in the ocean model driven by stochastic atmospheric forcing reveals that the IDV of the MOC is quite robust. Our results also indicate that though ocean dynamics in the subpolar gyre is responsible for sustaining the interdecadal signal, the ocean can transmit the oscillatory signal to other ocean basins through the displacement of the water mass interfaces. As suggested by Yin et al. (1992), this interaction between

two deep water sources may feedback to the thermocline circulation and the cross equatorial transports. This interaction may be related to Kelvin wave propagation (Johnson and Marshall 2002), which is not well resolved in our coarse-resolution integrations and remains an interesting aspect for further studies.

On the other hand, we acknowledge that the experiment we analyzed is an ideal integration without variability of the atmospheric forcing and atmosphere-ocean coupling. We know from chapter 4 that there are other physical mode(s) in the fully coupled model. Thus one concern is how much this interdecadal signal remains in a fully coupled run. This requires understanding about whether and how different physical modes interact which may give hints about different climate regimes (Raible et al. 2003).

Chapter 6

Multidecadal Variability as an air-sea coupled mode

6.1 Introduction

Observational studies show that the North Atlantic sea surface temperature (SST) exhibits substantial interannual to multidecadal variability (e.g., Bjerknes 1964; Deser and Blackmon 1993; Kushnir 1994; Hansen and Bezdek 1996; Sutton and Allen 1997; Delworth and Mann 2000; Czaja and Marshall 2001). These SST variations are associated with the North Atlantic Oscillation (NAO) and changes of the heat and moisture transport, as well as storm tracks over the North Atlantic (see reviews by Marshall et al. 2001; Hurrell et al. 2003; Czaja et al. 2003).

On interannual time scales, the SST variation is driven by NAO-like atmospheric variability (e.g., Bjerknes 1964; Battisti et al. 1995; Delworth 1996; Marshall et al. 2001; Visbeck et al. 2003). However, on decadal to multidecadal time scales, the SST variation is closely associated with ocean dynamics (e.g., Kushnir 1994; Hansen and Bezdek 1996; Latif and Barnett 1996; Sutton and Allen 1997; Halliwell 1998; Visbeck et al. 1998; Eden and Willebrand 2001; Eden and Jung 2001; Latif et al. 2004), and feeds back to the atmospheric circulation (Rodwell and Folland 2002; and Czaja and Frankignoul 2002).

The NAO actively couples with the Thermohaline Circulation (THC). Timmermann et al. (1998) reproduce a 35-yr oscillation in the northern hemisphere. The strengthening of the MOC is accompanied by enhanced northward heat transport tending to strengthen the NAO, which leads to the generation of negative sea surface salinity (SSS) anomalies off Newfoundland and east of Greenland by influencing the surface freshwater fluxes. These SSS anomalies weaken the deep convection in the ocean sinking regions and subsequently the strength of the THC, thus completing the cycle.

Eden and Greatbatch (2003) reproduce a coupled damped decadal oscillation

using a realistic North Atlantic Ocean model driven with NAO-related surface heat fluxes and wind stress anomalies. The subpolar gyre loses more heat during positive NAO leading to enhanced deep convection. This process works as a fast positive feedback. The delayed negative feedback involves the increased heat transport into the subpolar gyre due to strengthened Meridional Overturning Circulation (MOC); the consequent warming in the subpolar gyre tends to weaken the deep convection in the Labrador Sea. The positive feedback turns out to be necessary to distinguish the coupled oscillation from that in a model without an influence from the ocean to the atmosphere. Dong and Sutton (2005) suggest that a 25-yr oscillation of the MOC is forced by the NAO-related atmosphere pattern while the time scale is set by the ocean. The NAO affects the MOC by changing the strength of the ocean gyre and by directly forcing the region of active deep convection.

The coupling between the ocean gyre and the NAO can also generate a North Atlantic decadal oscillation (e.g., Wu and Liu 2005). The time scale and phase transition of the oscillation is set by the ocean dynamics. They argue that the atmospheric forcing can drive SST patterns similar to those in the fully coupled atmosphere-ocean model, but fails to generate any preferred decadal time scale.

The low frequency variability in the North Atlantic has significant impacts not only on the Atlantic region but rather on a global scale (e. g., Mysak et al. 1990; Schlesinger and Ramankutty 1994; Robertson et al. 2000; Raible et al. 2001; Latif 2001; Hoerling et al. 2001; Ogi et al 2004; Dong and Sutton 2005). Moreover, the other ocean-basins may not only passively respond to the low frequency variability in the North Atlantic, but can also actively interact with and hence affect the variability in the North Atlantic. An example of such cross-basin exchange is the tropical region which has been shown closely related to the state of the MOC (Latif et al. 2000; Schmittner et al. 2000; Hoerling et al. 2001). The North Pacific is suggested to respond passively to the

low frequency variability in the North Atlantic (e. g., Schlesinger and Ramankutty 1994; Ogi et al. 2004), but it may play an active role, as suggested by Wu and Liu (2005), who find that the low frequency variability in the North Atlantic is greatly weakened when the impact of the Pacific is eliminated.

Therefore, it is still not clear how the atmosphere and the North Atlantic Ocean are coupled on low frequencies. How other ocean basins are involved is even more elusive. Further studies are required to understand the mechanism.

In this work, we analyze the fully coupled atmosphere-ocean global circulation model - ECHAM5/MPIOM which exhibits two oscillations with time scales of 25-40 years and 45-80 years, termed as IDV and MDV respectively. The IDV exists as an ocean internal mode and is discussed in chapter 5. In this chapter, we focus on the air-sea coupled mode — MDV.

This chapter is organized as follows: section 6.2 describes the relative role of salinity and temperature in the Labrador Sea. Section 6.3 discusses the role of ocean dynamics and the air-sea coupling in generating the MDV. Section 6.4 presents results on the multidecadal variability in the North Pacific which is teleconnected with the North Atlantic via an atmospheric bridge, described by the Arctic Oscillation. The chapter is ended with a summary and discussions in section 6.5.

6.2 Role of salinity and temperature

It is anticipated that fluctuations of the MOC are related to changes in the density, temperature and salinity structure of the North Atlantic. This relation is investigated by calculating linear regressions of the time series of density, thermal- and haline-components of density onto the multidecadal component of the MOC index in the Labrador Basin at grid points where the mean MLD in March exceeds 1200m. These regressions are calculated at various lags in order

to provide an evolution picture as the MOC varies.

To highlight the multidecadal variability, a high-pass filter is applied to the MOC index with a cut-off frequency 100 yrs, then variability with period shorter than 40 yrs are subtracted from it to remove the high frequency component and the interdecadal variability. Therefore the regression patterns are anomalies associated with multidecadal variability of the MOC.

The regression coefficients are averaged horizontally over the selected ocean domain and vertically over the whole water column, shown in Fig. 6.1. The corresponding density anomalies lead the MOC by 15 years, suggesting that the density anomalies drive the MOC changes. Temperature contributes positively to the density anomalies, and salinity plays an opposite role.
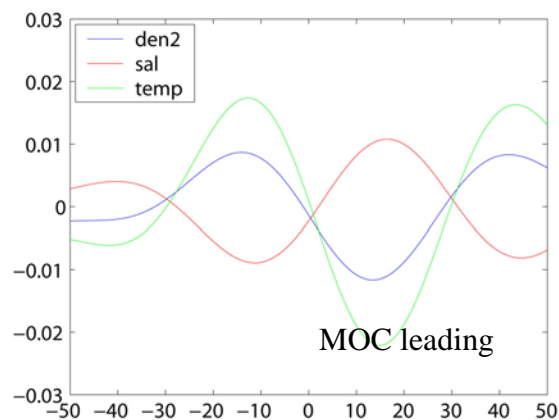

Fig. 6.1: regression coefficients between various quantities and the time series of the MOC index at 30° N in CPL (kg/m^3 / Sv). Blue, red, and green lines denote the regression of potential density, its haline and thermal part onto the MOC index. Reference depth is at 2000 m. Regression coefficients were averaged horizontally over the region where the mean MLD in March is larger than 1200m in the Labrador Sea and vertically over the whole water column.

However, the relative contribution of temperature and salinity varies with depth. Shown in Fig 6.2 are the corresponding regression coefficients averaged

vertically over the upper 150m in the same region. The density anomalies near the surface are contributed almost solely by salinity changes which leads the MOC also by 15 years. To illustrate the vertical structure of the density anomalies, the regression coefficients are averaged horizontally over the same region, shown in Fig. 6.3. The density anomalies are enhanced near the surface. In the upper 150m, positive (negative) density anomalies are associated with warm and saline (cold and fresh) anomalies, while in the intermediate depth (between 150m to 2200m), they are associated with cold and fresh (warm and saline) anomalies. Therefore, both temperature and salinity field have a baroclinic structure; salinity dominates the density changes near the surface, and temperature dominates in the intermediate depth.
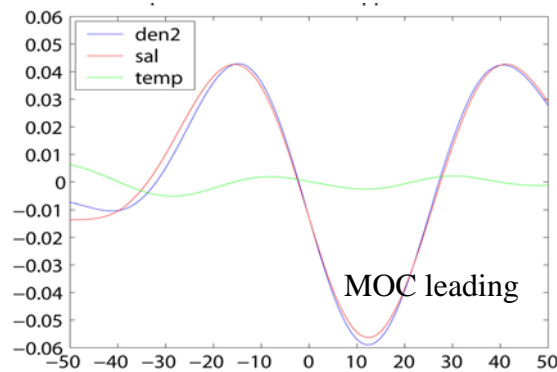

Fig. 6.2: the same as fig 6.1 but the regression coefficients are averaged over the upper 150m in the selected region.

The baroclinic structure in temperature and salinity field is a characteristic of deep convection: strong mixing brings down relatively denser water which is generally cold and fresh and at the same time moves up relatively lighter deep water which is relatively warm and saline. Thus the surface layer in the deep convection sites gains heat and salinity from deeper water; this heat gain will be consumed through heat loss to the atmosphere and oceanic advection, as will be shown later (Fig. 6.8b). The baroclinic structure is also present on interdecadal time scales but less clear in temperature field (Fig. 5.2); in stead, the surface temperature field on the interdecadal time scales shows only slightly weaker

signals compared to the deeper layer, which is due to the weaker surface heat loss given constant climatological surface heat fluxes in experiment CLIM than in a fully coupled case.
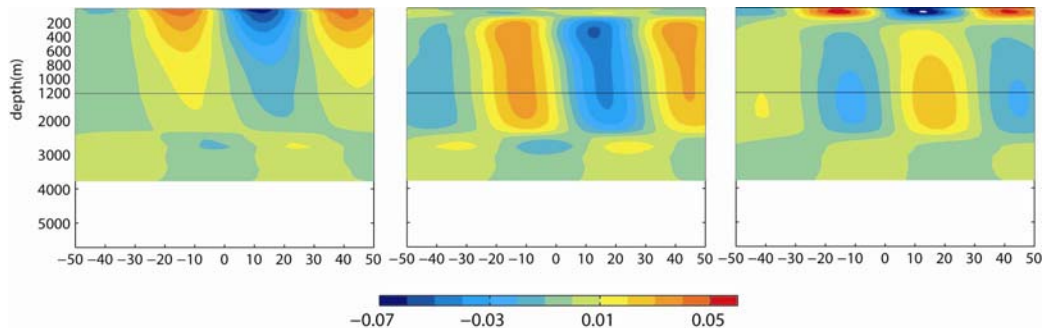

Fig. 6.3: time-lag regression of density in the LAB onto the multidecadal MOC index (Unit: kg/m^3 /Sv). Density (a) is divided into its b) thermal and c) haline part. The regression coefficients are calculated as in Fig. 6.1 at each grid point but averaged horizontally. Positive lags mean the MOC leading.

6.3 Mechanism of the Multidecadal Variability

The water mass characteristics in Labrador Sea are subject to changes in the following processes: the local air-sea exchange, deep convection; and nonlocal ocean dynamics. Dynamics of the subpolar gyre are tightly related with these processes above (Curry and McCartney 2001; Hátún et al. 2005) and are particularly important.

In this section we are going to show that the temperature anomalies in the intermediate depths in the Labrador Sea are associated with ocean dynamics, however, the dominant saline contribution to density anomalies near the surface reveals an important role of the air-sea coupling.

6.3.1 Geostrophic balance

On interdecadal time scales, the MOC variation is highly correlated with horizontal density gradients. To evaluate whether this geostrophic relation holds

on multidecadal scales, north-south and east-west density gradient, Dns and Dew, are calculated in the same way as in chapter 5 (refer to chapter 5 for details). The density gradients are correlated onto the MOC index (Fig. 6.4); the associated changes in the meridional mass, heat, and salinity transport in the Atlantic are shown in Fig. 6.5. Heat transport through a north-south section across the NAC is regressed onto the multidecadal MOC index to capture the variation in the zonal transport (Fig. 6.6). Refer to chapter 5 for the location of the section and its mean temperature and u-velocity structure (Fig. 5.6-7).

When Dns leads the MOC by 12 years, they have maximum correlation; and when the MOC leads by 17 years, they have the minimum correlation. Dew has a minimum correlation coefficient with the MOC when it leads the MOC by 9 years and a maximum coefficient when the MOC leads by 17 years. The maximum Dns slightly leads the minimum Dew by 3 ~ years.
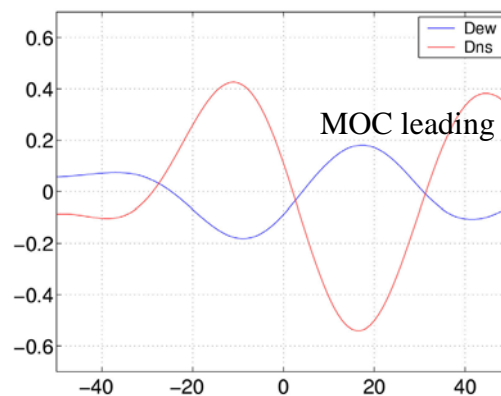

Fig. 6.4: as Fig. 5.5 but for the coupled integration (CPL).

The MOC recovers to its maximum from lag -25 to lag 0 (Fig. 6.5a) in response to cooling between 45° N and 75° N in the upper 2500m (Fig. 6.5b) which is partly counteracted by fresh anomalies (Fig. 6.5c). The maximum Dns near lag -15 (Fig. 6.4) corresponds to the penetration of the cold and fresh anomalies down to 3000m (Fig. 6.5b). At lag 0 warm anomalies appear near the surface between 45° N and 60° N which then become stronger and lead to weakening of the MOC (Fig. 6.5b).
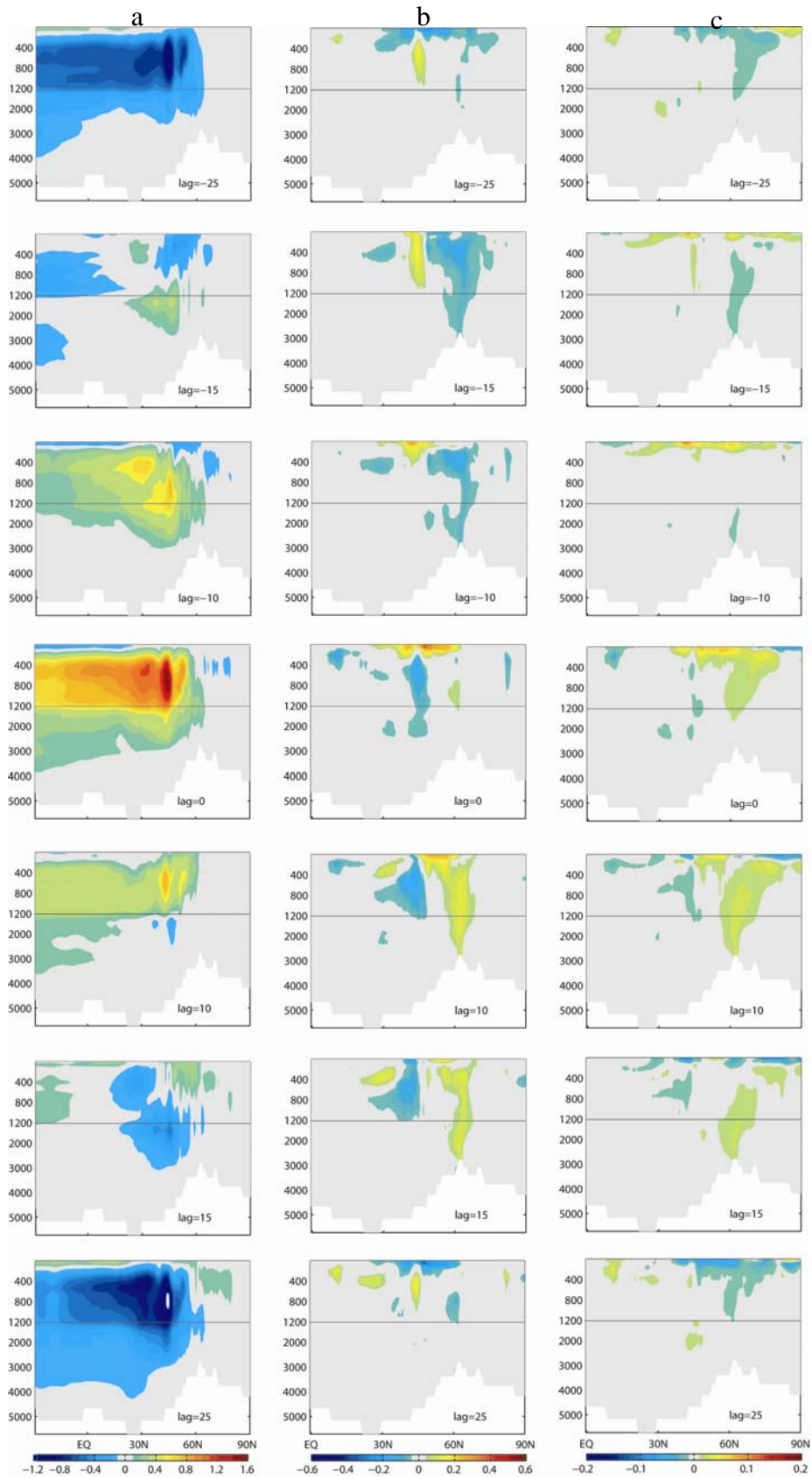
Fig. 6.5: Regression between various quantities with the multidecadal MOC index: zonally averaged a) streamfunction (Sv), b) temperature (^{o}C) and c) salinity (psu). Linear detrending and an 11-yr running mean are applied before regression calculation.
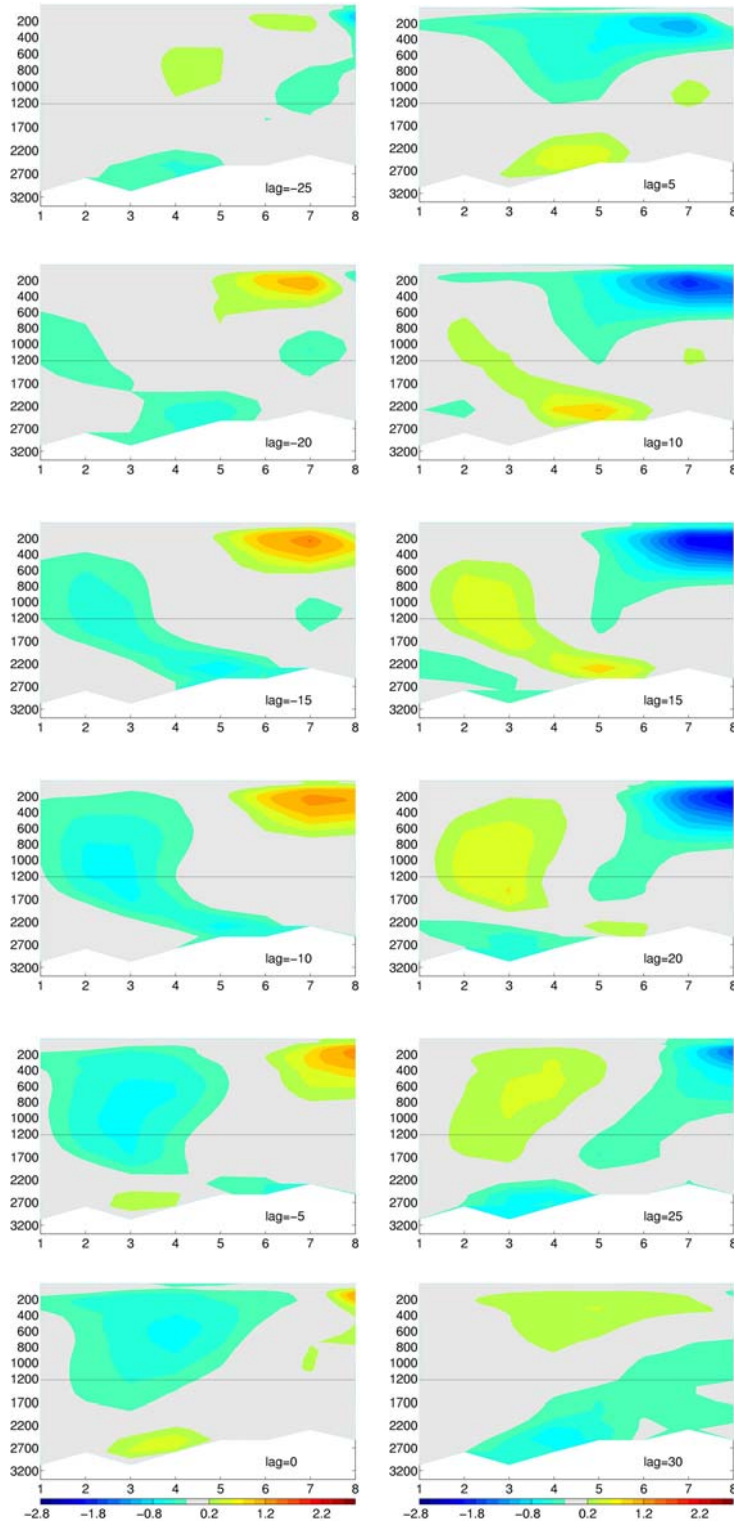
Fig. 6.6: Time-lag regression of heat transport through the section (defined in Fig. 5.6) onto the multidecadal MOC index (Unit: 0.001PW / Sv). The section goes from north to south from 1…8. The x-axis interval does not correspond to the real distance between the selected points. Numbers at the lower right corners indicate the lead-lag information, positive values meaning the MOC leading.

From lag -25 to lag 0, the NAC-related heat transport is in its positive phase (Fig. 6.6), with the maximum at lag -15 when Dns is at its maximum (Fig. 6.4). During the same period, the eastward transport of the subpolar water weakens. This suggests that the section is controlled by an anomalous cyclone, which is limited to the upper 1700m. An anomalous anticyclone is present below 1700m, seen clearly at lag -5 (Fig. 6.6). From lag 0 to lag 30, the condition is reversed: the section is controlled by an anomalous anticyclone in the upper 1700m and an anomalous cyclone below. The whole cycle is completed. The corresponding mass transport pattern has a very similar pattern, suggesting that this pattern is associated with anomalous u-velocity.

The current anomalies in the upper 1700 m at this section is associated with the cold (warm) anomalies carried by the newly formed deep water in the Labrador Sea, as shown in Fig. 6.7. At lag -25, cold anomalies first appear south of Iceland; later the cold anomalies spread to the Labrador Basin. At lag -15, the cold anomalies occupy the whole subpolar gyre (Fig. 6.7), corresponding to the maximum Dns at this time (Fig. 6.4). From lag -15 to lag 0, the cold anomalies move into the subtropics while warm anomalies appear in the northern subpolar gyre. Warm anomalies near Portugal at lag -5 (Fig.6.7) are related to changes of the Mediterranean Overflow. At lag 0, warm anomalies enter the Labrador basin from east of Greenland; cold anomalies have taken control of the whole subtropical basin. At lag 5, the Labrador Basin is fully occupied by warm anomalies and become stronger with time leading to the minimum Dns at lag -15 (Fig. 6.4). At lag 20, the warm anomalies spread to the subtropics via both sides of the Middle Atlantic Ridge.
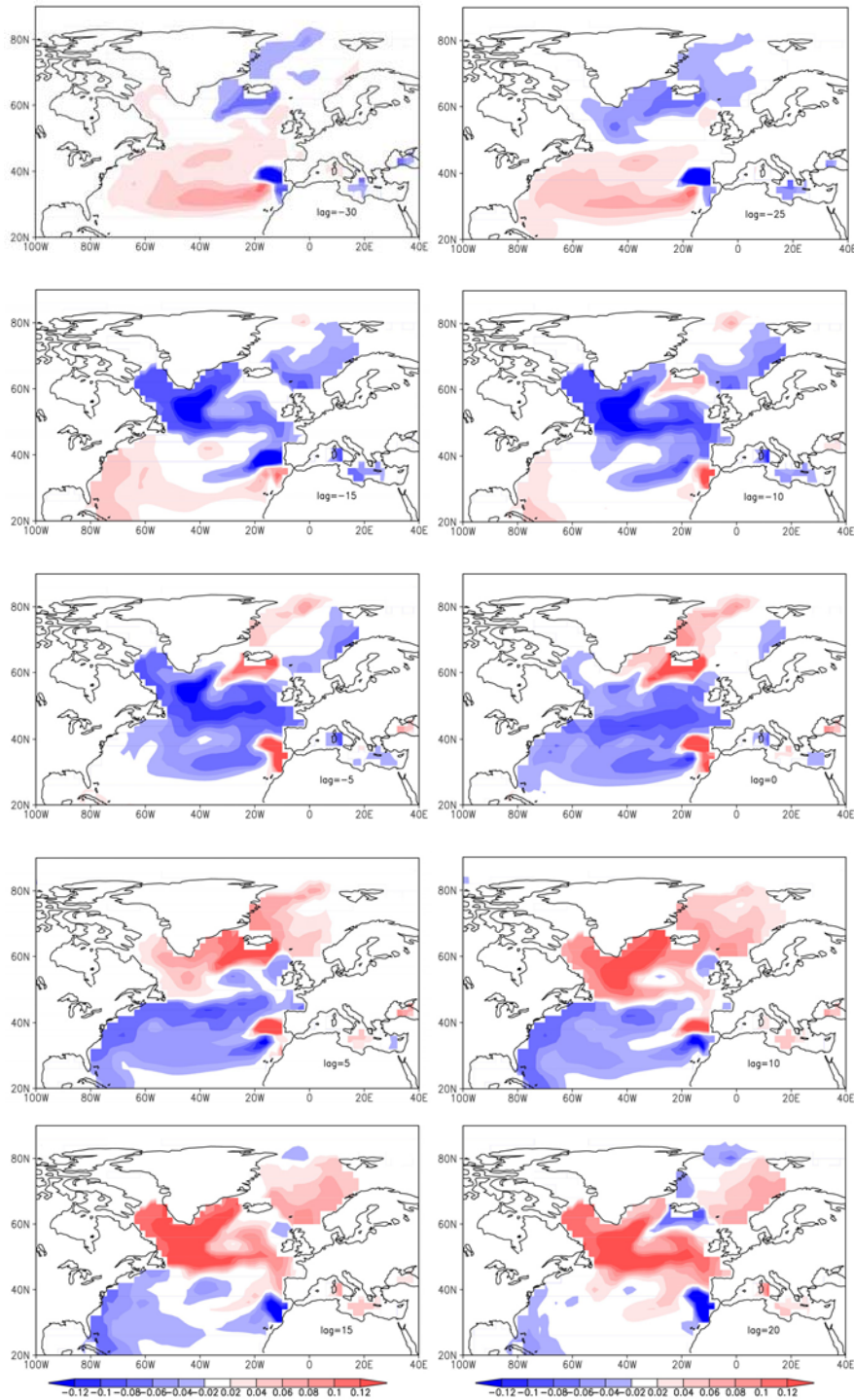
Fig. 6.7: regression coefficients of temperature anomalies at 1525m onto the multidecadal

MOC index at lag -30, -25, -15, -10,-5, 0, 5, 10, 15 and 20 (unit: $^{\circ}$C/Sv). Time lags are

shown at the lower corner of each panel. Positive lags mean the MOC leading.

In summary, the MOC variation on multidecadal time scale is tightly related to

the horizontal density gradients. The recovery of the MOC (from lag -25 to lag

0, Fig.6.5a) is accompanied by cooling in the deep convection sites. These cold anomalies penetrate to greater depth (Fig. 6.5b, from lag -25 to lag -15) leading to increased Dns (Fig.6.4); when the cold anomalies move out of the convection center (Fig. 6.5b and Fig. 6.7, from lag -15 to lag 0), Dns weakens (Fig. 6.4). The increasing and the following decreasing of Dns leads to strengthening and weakening of the eastward NAC transport (Fig. 6.6), revealing the geostrophic nature. The newly formed LSW moving out of the Labrador Sea to east of Newfoundland within ~ 3 years, connects the changes of Dns with the ones of Dew. The following eastward propagation along the subpolar front sets the rhythm of the Dew which controls the meridional heat and mass transport.

When the temperature anomalies move eastward along the subpolar front, they are surrounded by anomalous current anomalies. This process bears similar characteristics to the ones related to the interdecadal oscillation of the MOC discussed in chapter 5, thus not discussed detailed here. The results above suggest that the MDV of the MOC is associated with a geostrophic advective process.

6.3.2 Role of the atmosphere

In this section, we investigate how the air-sea coupling influences the near-surface salinity anomalies in the Labrador Sea. First, to evaluate what contributes to the near-surface salinity anomalies in the Labrador Sea, the freshwater budget is calculated; then presented are the results about how the atmosphere and ocean are coupled on multidecadal time scales. All the atmosphere data analyzed start from year 400; the SLP record is 600 years long whereas other records are only 574 years long due to damage in data storage. When linear regression is calculated between the atmospheric variables and the multidecadal MOC index, the MOC index is cut to the same length as the corresponding atmospheric variable.

i.   What contributes to the near-surface salinity anomalies in the Labrador Sea?

The following factors affect the surface salinity in the Labrador basin: freshwater exchanges with the overlying atmosphere, ocean advection bringing water masses originated from the subtropics or the Arctic, and communication with the deep ocean via convection and downwelling. To investigate which process is responsible for the near-surface salinity change in the Labrador Sea, we calculate the freshwater budget over the region with the strongest convection in the Labrador Sea (not shown, a bit larger than the region considered for regression calculations in section 6.2 for the upper 100m. The freshwater storage is defined by

$$FWC = \int\int\int (S - S_{ref})/S_{ref}\, dzdxdy$$

Where S_{ref} is the reference salinity, here taken as $S_{ref} = 35.14$. The budget equation describing the freshwater storage change term is given in a simplified form by

$$
\begin{aligned}
FWC_t = \ &\sum advective\ fluxes\ from\ all\ the\ boundaries\\
&+ \int\int surface\ fluxes\\
&+ \sum diffusion \qquad\qquad\qquad\qquad\qquad (1)
\end{aligned}
$$

The term on the left side of the equation (1), FWC_t, corresponds to the time derivative of the freshwater storage, denoted as 'DFWCDT' in Fig. 6.8a; on the right side, the first term is the advective fluxes (both lateral and vertical, denoted as 'ADV'); the second is the freshwater input through the surface freshwater fluxes, denoted as 'PEM'; and the third is the diffusion term, represented as the residue of other three terms, denoted as 'RDU'. The time series of these four terms are shown in Fig. 6.8a. The freshwater storage in this box is also shown as the blue line. The heat budget is calculated in the same way, i. e., heat content change equals to the input from the ocean advective,

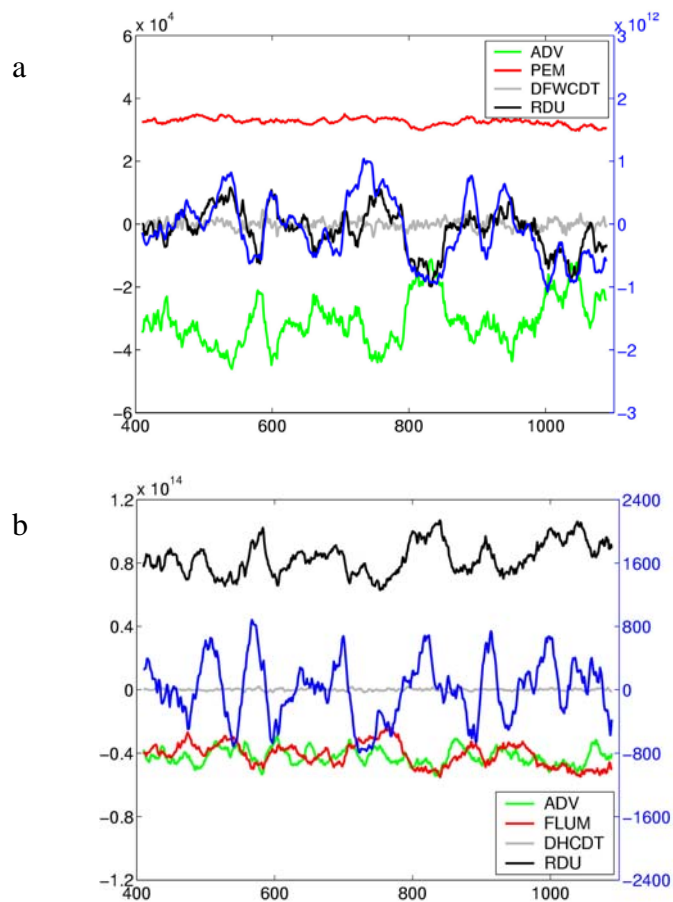surface heat fluxes, and diffusion term, termed as DHCDT, ADV, FLUM, and RDU in Fig. 6.8b.

Fig. 6.8: a). Time series of the freshwater budget terms for the upper 100m in a box in the Labrador Sea (unit: m^3/s, left axis): advective term (ADV, green line, sum of lateral and vertical advection at the bottom), surface freshwater fluxes (PEM, red line), freshwater storage change (DFWCDT, gray line), and the diffusion term calculated as the residue, denoted as 'RDU' (Unit: m^3/s). b). same as a) but for heat budget (left axis, unit: W).Blue lines in a) and b) (follow right y-axis) are the freshwater content (unit: m^3) and detrended mean MLD averaged in the Labrador Sea where the mean MLD in March is larger than 1200m (unit: m) respectively.

The surface freshwater fluxes are a freshwater source (with a positive sign in Fig. 6.8a); and the ocean advects freshwater away from the selected box. While the RDU term and the advective term exhibit considerable low frequency

variability, the surface freshwater fluxes remain relatively stable. The diffusion term is almost in phase with the freshwater content, but out-of-phase with the advective term. The heat budget shows that the heat source is the diffusion term which is balanced by ocean advective term and surface heat fluxes which move heat away from the selected box (Fig. 6.8b). The heat gain through the diffusion term is almost in phase with deep convection events indicated by the mixed layer depth, but out-of-phase with the surface heat fluxes. In other words, enhanced (weakened) deep convection is associated with increased (reduced) heat gain through the diffusion term and increased (reduced) heat loss through surface heat fluxes.

It is reasonable to assume that the diffusion term is mainly determined by deep convection (vertical mixing) in the Labrador Basin. Therefore, Fig. 6.8 shows such a picture: increased surface heat loss leads to strong deep convection, which is responsible for increased heat and salinity gain from the deep ocean. This process is accompanied by reduced salinity input through ocean advection.

ii. Air-sea interaction

We show in this section what leads to the strong surface heat loss and enhances deep convection in the Labrador Sea. Because surface heat fluxes are tightly related to the atmospheric circulation pattern, to obtain a large-scale picture, time-lag linear regressions are calculated between various atmospheric variables, SST and the multidecadal MOC index. The mean SLP and surface wind stress are shown in Fig. 6.9 and the regressions are shown in Fig. 6.10-14. For brevity, pictures from lag -30 to lag 0 when the MOC evolves from its minimum to its maximum are shown. For the opposite half of the oscillation, the associated ocean conditions are with opposite signs.

The subpolar low is centered south of Greenland and extends northward to the southern part of the GIN Sea (Fig. 6.9). The subtropical high is centered near

the Sahara. Thus strong southwestlies prevail in the North Atlantic between 40° N and 60° N.
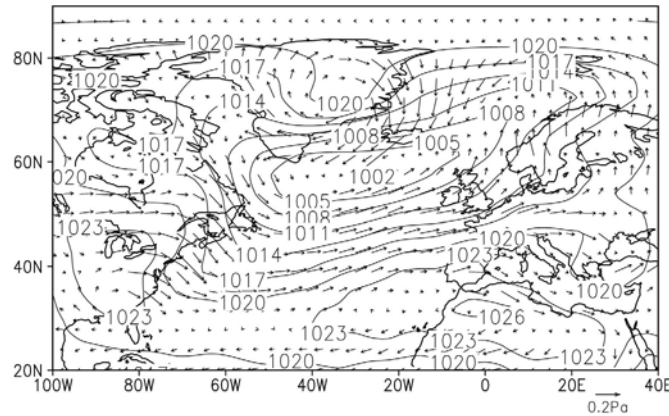

Fig. 6.9: mean wintertime SLP and surface wind stress (unit: hPa)

The associated SLP pattern (Fig 6.10) shows an east-west dipole structure at lag -30, with low pressure overlying the Labrador Basin and high pressure centered in the GIN Sea. From lag -30 to lag -15, the low pressure becomes even lower when it moves over Greenland while the high pressure becomes even higher and shifts to the Azores region. At lag -15, the SLP anomalies resemble a positive NAO pattern. From lag -15 to lag 0, the high pressure center shifts to east of Newfoundland and the Labrador Basin; the low pressure shifts from Greenland to the GIN Sea. Half of one multidecadal cycle is completed.
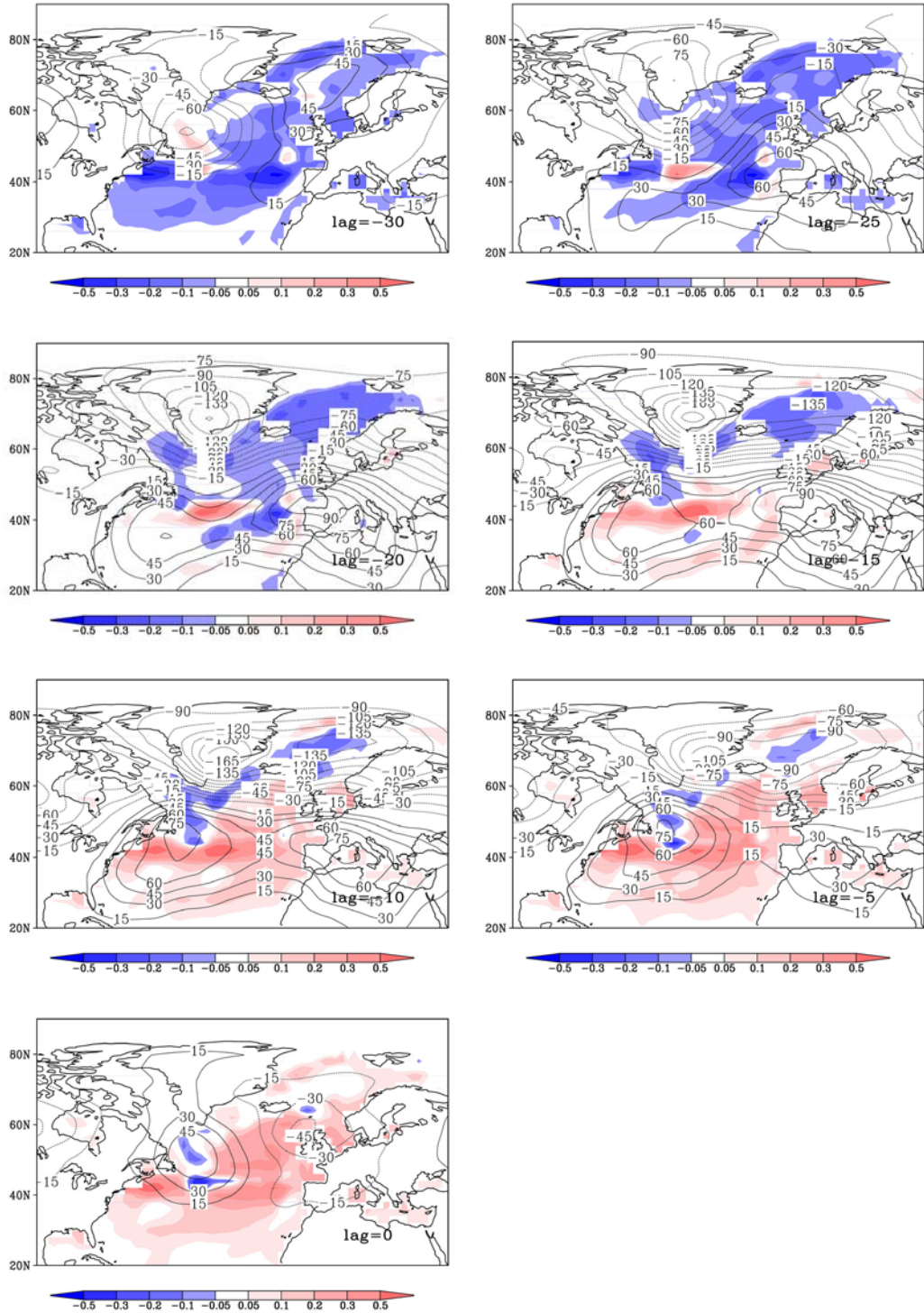
Fig. 6.10: regression coefficients of the SST (shade) and the SLP (contour) onto the multidecadal MOC index (Unit: ^{o}C/Sv and Pa /Sv). Before the regression, linear trend is removed from the SST and SLP, and then an 11-yr running mean is applied.

The spatial pattern of the SLP anomalies has some correspondence to the SST

anomalies: when cold anomalies intrude into the eastern subpolar gyre resulting from the weakened NAC heat transport (Fig. 6.10, at lag -30), the Labrador Sea is still occupied by warm SST anomalies. Therefore, an east-west SST gradient is formed, corresponding to the east-west dipole SLP pattern. When the cold anomalies occupy the Labrador Sea, warming takes place south of the NAC route (south of 48° N) resulting from the enhanced NAC heat transport (e. g., at lag -15) and a north-south temperature gradient across the NAC is built up which favors a NAO-like SLP pattern. The following process in which the warm anomalies move to the Labrador Sea while the subtropics still experiences warming weakens the north-south temperature gradient and the SLP pattern changes accordingly.

The strong impact of the North Atlantic SST anomalies upon the atmospheric SLP anomalies on 'interdecadal' time scales has been suggested independently by Wohlleben and Weaver (1995). They show that the SST anomalies in the vicinity of the Labrador Sea are important in modulating the north-south temperature gradient across the Gulf Stream and hence the atmospheric baroclinic zone, the accompanying jet stream, and the frequency of the baroclinic eddies or storms. Because the atmospheric eddies are the main carrier of the atmospheric northward heat transport, they are very important for the SLP field. The relation between the SST and the SLP (Fig. 6.10) is supportive of their results. We also find that the negative correlation between the SLP and the SST (warm anomalies vs. negative SLP anomalies and vice versa) is stronger on the multidecadal time scale than on shorter time scales (not shown).

The wind stress anomalies associated with the SLP pattern are of great importance to the strength of the ocean gyres. For example, at lag -30, the Labrador Sea is under a positive wind stress curl and the GIN Sea is under a negative wind stress curl (Fig. 6.11~12). The positive wind stress curl over the Labrador Sea reaches its maximum between lag -15 to lag -10 with its center

over Greenland. As a result, the cyclonic gyre in the Labrador Sea speeds up leading to more domed pycnocline and consequently stronger heat loss (Fig. 6.13), which leads to enhanced deep convection in the Labrador Sea, thus cold and fresh anomalies sink down and relatively warm and salty deep water are brought up to the surface, reflected by the near-surface warm and salty anomalies (Fig. 6.3, 6.8).
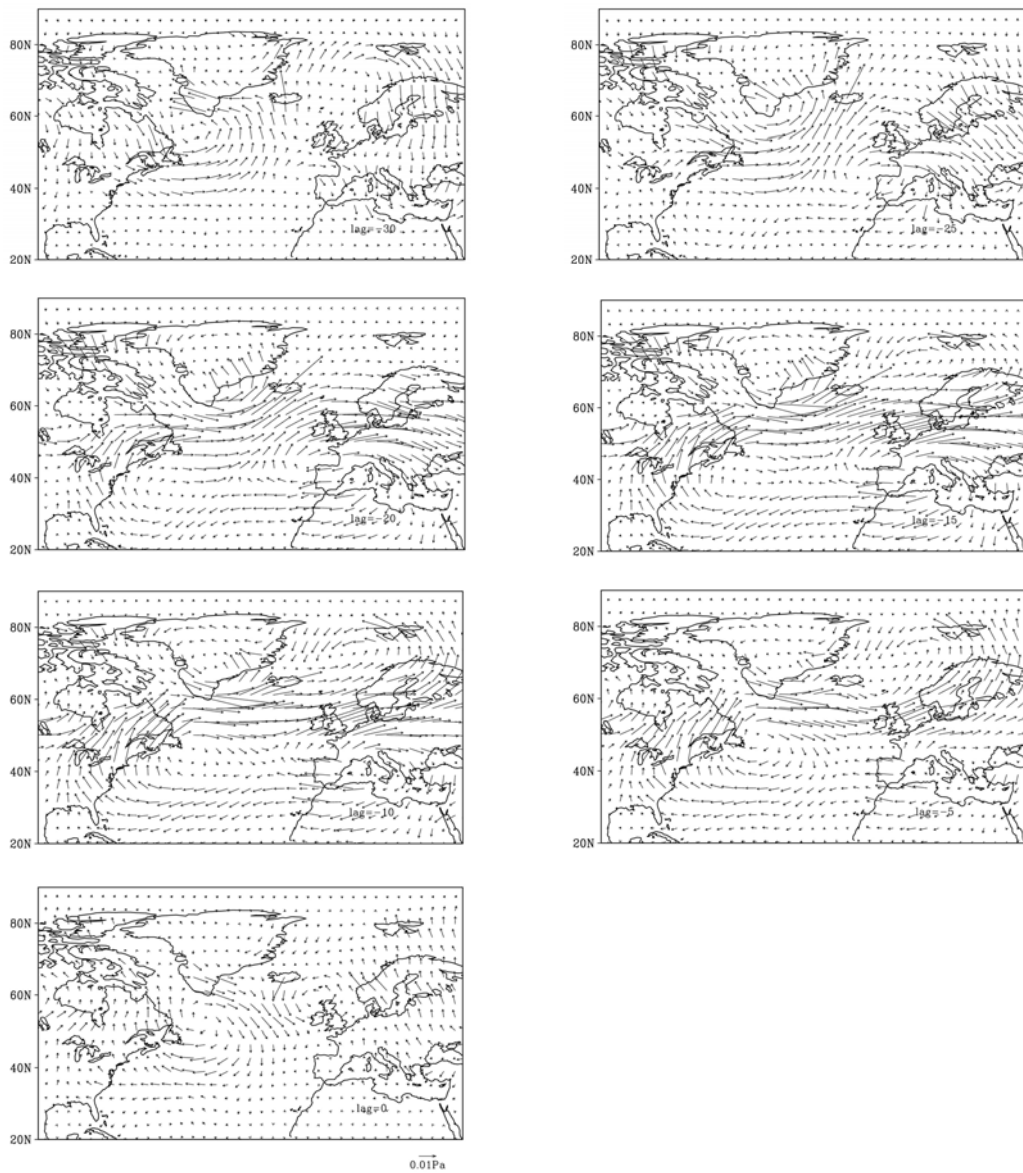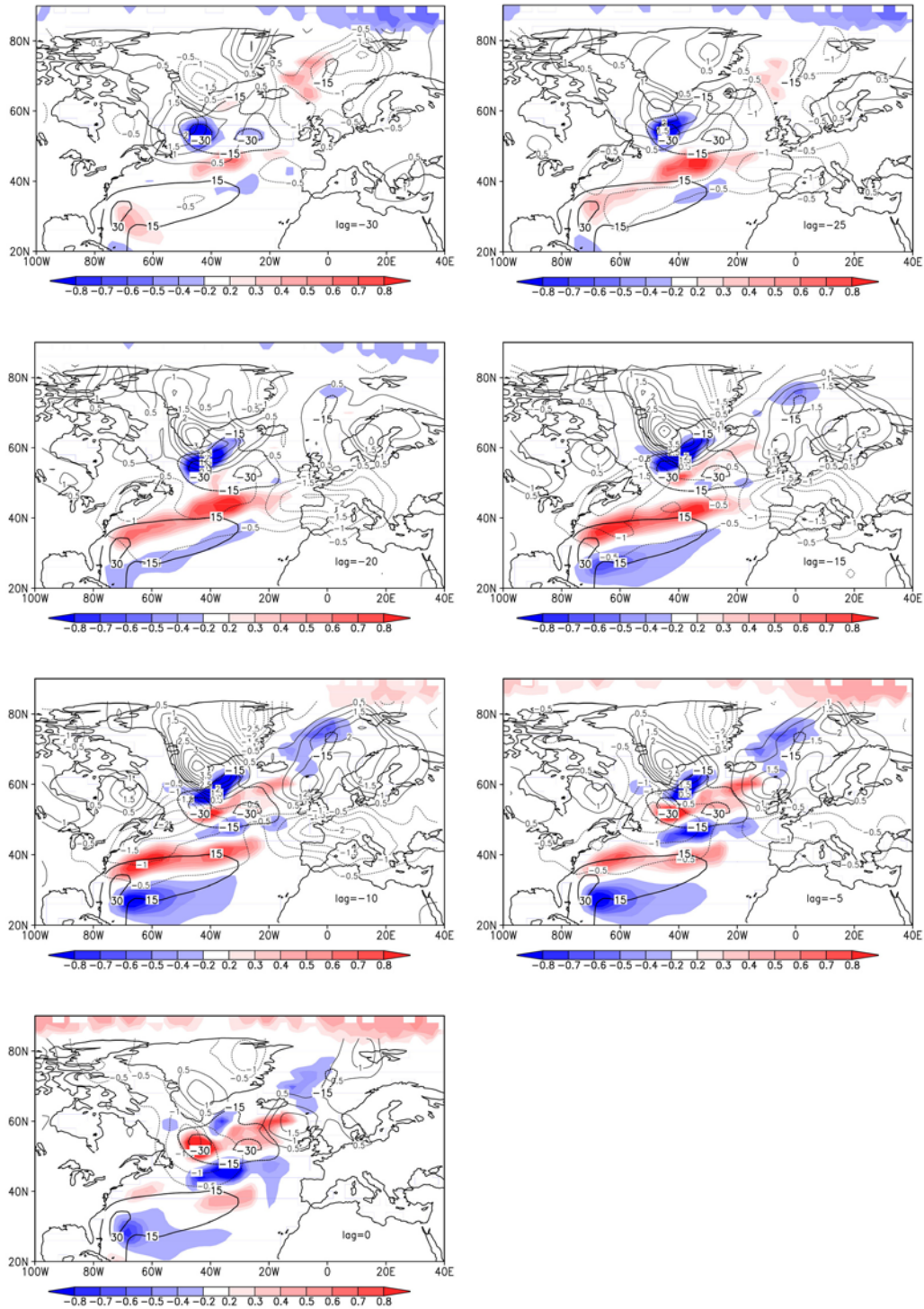

Fig. 6.11: regression coefficients of wind stress (unit: Pa /Sv) onto the MOC index.

Fig. 6.12: regression coefficients of wind stress curl (thin line, unit: 1e-8* N/m3 /Sv) and the barotropic streamfunction (shaded, unit: Sv /Sv) onto the multidecadal MOC index. The thick lines are the mean barotropic streamfunction at every 15 Sv.
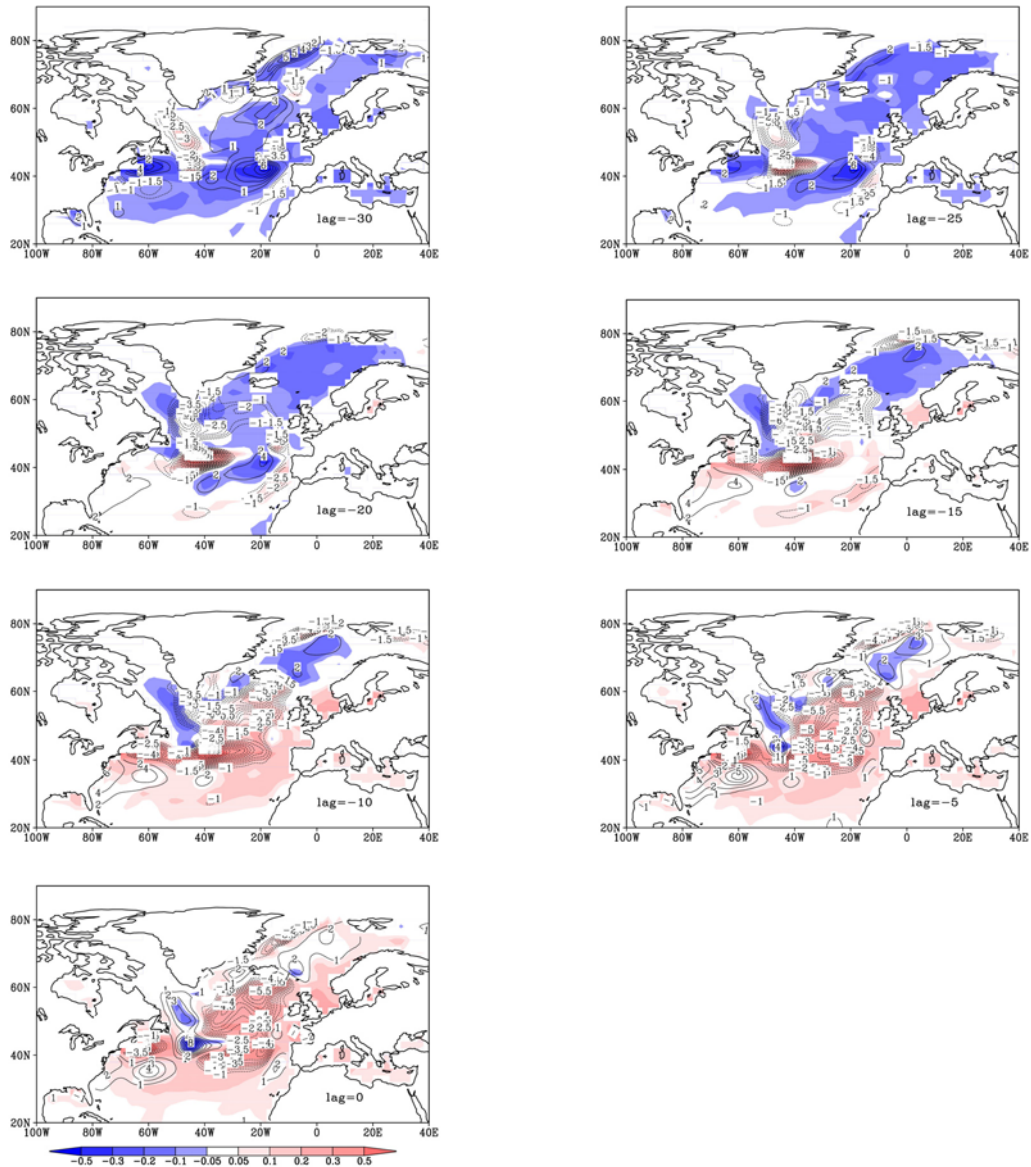
Fig. 6.13: regression coefficients of SST (unit: ^{o}C /Sv) and the surface heat fluxes (unit: w/m^{2} /Sv) onto the multidecadal MOC index. Positive surface heat fluxes mean anomalous heat gain from the atmosphere.

We notice that the subtropics are also affected by the anomalous wind stress: from lag -30 to lag 0, part of the subtropical gyre speeds up in response to the negative wind stress curl, mainly along the NAC route (Fig. 6.12). Therefore, the subtropical gyre carries more warm anomalies back to low latitudes leading to the large-scale warming in the subtropical gyre from lag -15 to lag 0 (Fig. 6.13). In experiment CLIM, this interaction between the wind stress and the ocean gyres is missing, which explains why the NAC-related SST anomalies

are confined along the subpolar front and accumulate in the eastern subtropics in experiment CLIM (Fig. 5.4). This interaction also contributes to the longer time scale of the MDV, because it takes longer to build up the east-west density gradient since in the coupled run the ocean gyres are more efficient to move the temperature anomalies away from the subpolar front.
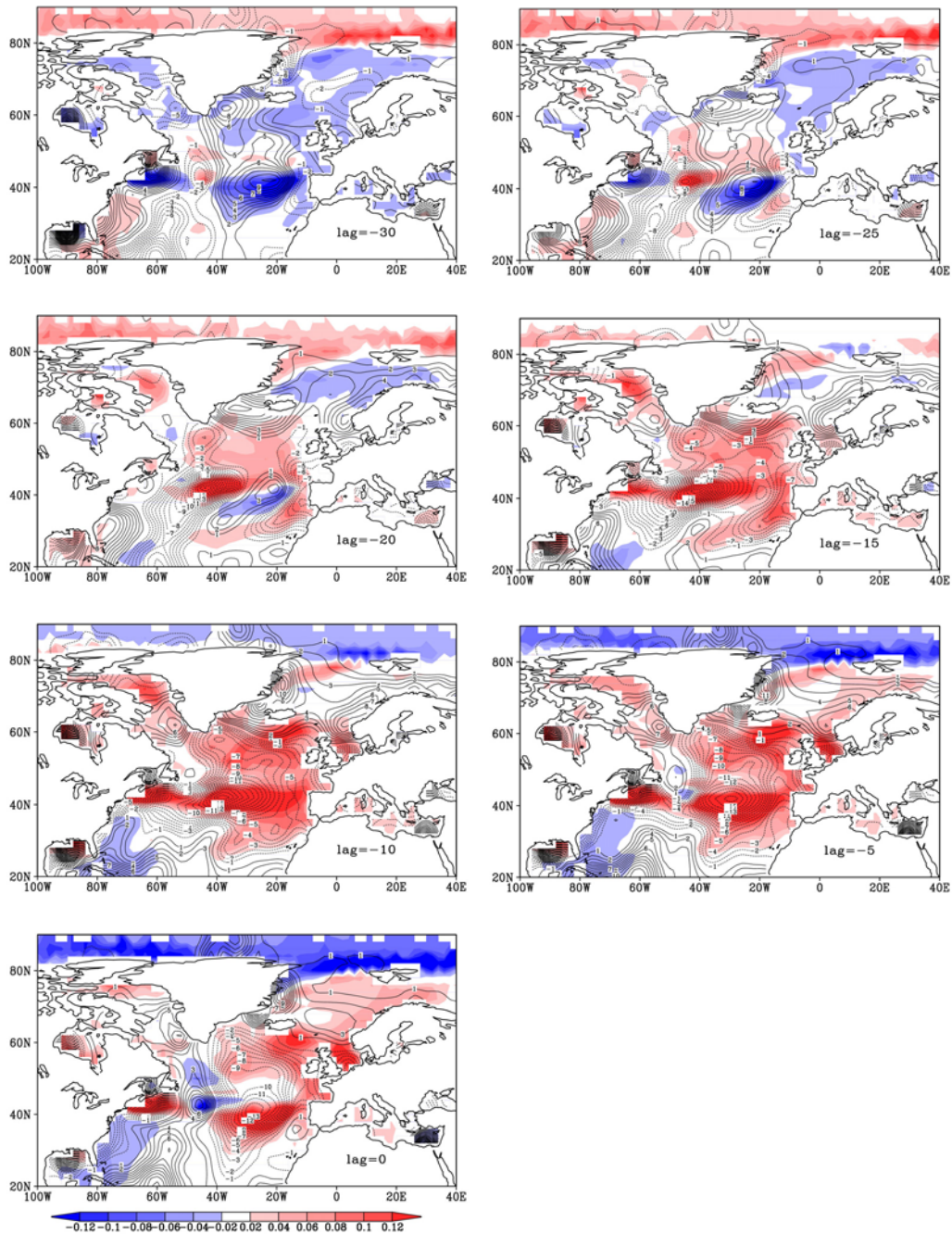

Fig. 6.14: regression coefficients of SSS (shaded, unit: psu /Sv) and the surface freshwater fluxes (contour, unit: 10^{-10} m/s /Sv) onto the multidecadal MOC index. Positive freshwater fluxes mean anomalous water gain from the atmosphere.

Besides directly forcing the ocean gyre and the deep convection sites, the forced atmospheric circulation anomalies are also actively involved in the preconditioning process. For instance, the warm and saline anomalies are accompanied by negative surface heat and freshwater fluxes (Fig. 6.13-14), indicating that the atmosphere tends to damp the surface temperature anomalies but enhance the surface salinity anomalies. Thus the upstream of the deep water becomes less warm and more saline. Considering the dominant role of temperature in determining density anomalies, the atmosphere acts to weaken the ensuing weakening tendency of the MOC associated with the warm and saline anomalies.

In summary, ocean dynamics are responsible for the MOC variation on multidecadal scales by adjusting the north-south and east-west temperature gradients; salinity plays against thermal effects. Distinguished from the ocean self-sustained interdecadal variability (IDV, chapter 5), the MDV shows a clear fingerprint of the air-sea coupling: the atmospheric circulation anomalies, which is forced by underlying SST anomalies, enhance the tendency of cooling (warming) in the deep convection sites by speeding-up (slowing-down) the cyclonic gyre in the Labrador Sea via wind stress curl and surface heat fluxes and hence intensifying the strengthening (weakening) tendency of the deep convection. In other words, the variability of the deep convection in the Labrador Sea is amplified by the air-sea coupling. As a result, salinity dominates density anomalies near the surface, which enhances the integrated density anomalies and is critical to a significant MDV mode.

The air-sea coupling also accounts for the longer-time scale of MDV relative to IDV. On both inter- and multi-decadal time scales, the ocean sets the time scale. The key process is the built-up of the horizontal density gradient. In the fully coupled model, the ocean is more efficient to move the temperature (density) anomalies away from the subpolar front and hence it takes longer to build up

the east-west density gradient. The north-south density gradient depends largely on the density anomalies in the Labrador Sea. Temperature still dominates the density changes in the coupled case, but the thermal contribution is weakened due to atmospheric damping in the preconditioning process in which salinity anomalies are enhanced. The net effect is the density anomalies (integrated over the upper 2000m) with reduced amplitude compared to the ones in IDV (compare Fig 6.1 and Fig. 5.1), which explains the longer time needed to build up the north-south density gradient.

6.4 Multidecadal variability in the North Pacific

One interesting phenomenon is that the North Pacific exhibits also considerable multidecadal variability in the temperature and salinity field (Fig. 6.15) which is not present in experiments RAND and CLIM. Strengthening of the MOC is followed by warm and saline anomalies in the North Pacific. The change in the North Atlantic must somehow project onto the North Pacific.
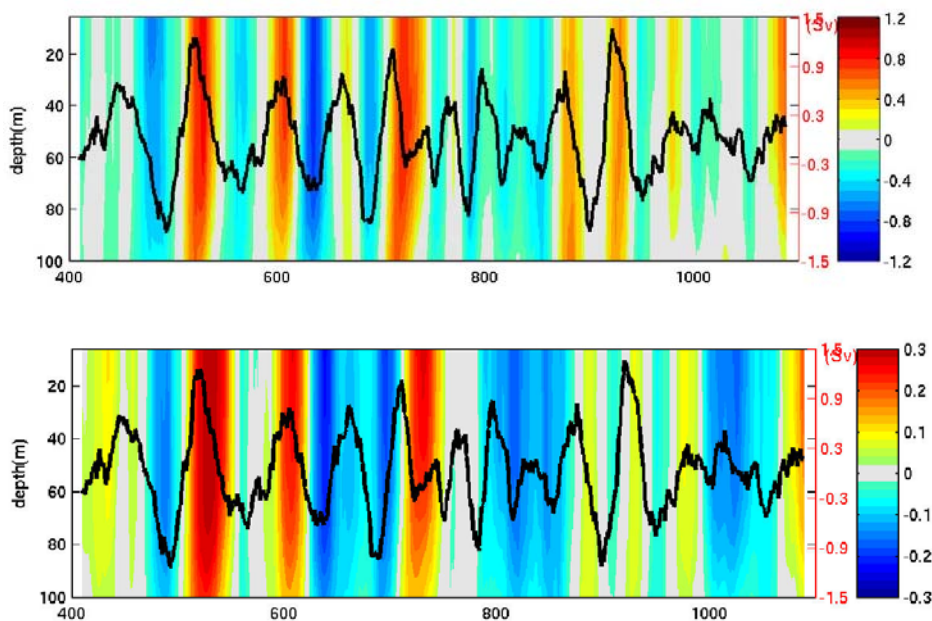
Fig. 6.15: time series of the MOC index (black line, right y-axis, unit: Sv) and the depth-time plot of the temperature (upper panel, unit: ^{o}C) and salinity (lower panel) anomalies in the Pacific averaged over the range between 45N and 60N, east of 180E. Linear trend is first removed and then a 21-yr running mean is applied.

6.4.1 Heat budget analysis

The heat budget is calculated for the upper 100m in the area 20° N – 60° N, 124 ^{o} E – 153° E (Fig. 6.16). The advective heat transport into the box comes from the southern boundary, which is mainly contributed by the Kuroshio Current (KC) ('SOUTH'), from the eastern boundary ('EAST') and the bottom of the box ('VERT'). The diffusion term is calculated as the residue of all other terms. The KC-related advection is the main heat source (Fig. 6.16a). The diffusion term (RDU) and the vertical advection (VERT) also input heat into the selected box. The exchanges through the eastern boundary and the surface heat fluxes ('FLUM') tend to cool the box (negative sign in Fig. 6.16a).

Horizontal advective terms, the surface heat fluxes and the residue term are regressed onto the heat content (Fig. 6.16b). The vertical advection term shows similar tendency as the advection term through the eastern boundary but with weaker amplitude and is not shown.
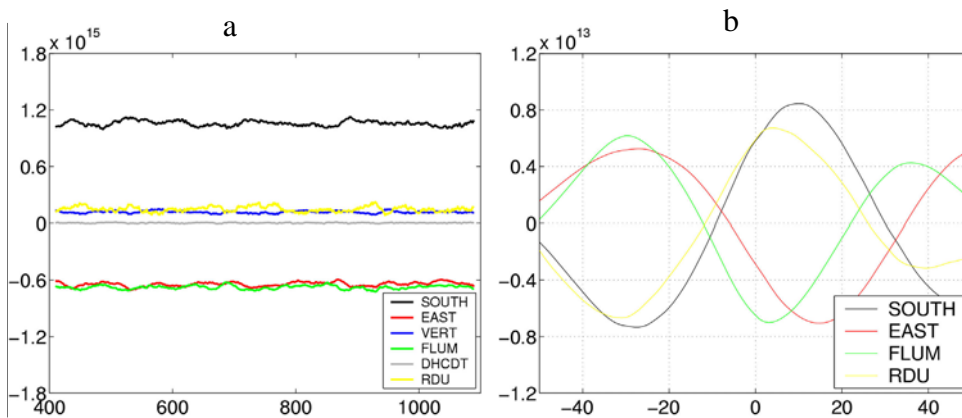
Fig. 6.16: a) heat budget in the upper 100m between 24° N-60° N, 124° E-153° E (unit: W,, positive values mean the box gains heat): advective heat transport through the southern ('SOUTH'), eastern ('EAST') and bottom ('VERT') boundary; surface heat fluxes ('FLUM'), and the diffusion term calculated as the residue from all other terms ('RDU'). b) Time-lag regression of several terms against the heat content (unit: W/J). A 21 years running mean is applied in a). In b), all time series are filtered by 31 years running mean and high-passed with a cut-off frequency 100 yrs. Positive lags mean the heat content leading.

Maximum heat content at lag 0 is contributed by the KC-related advection and the diffusion term, but is damped by surface heat fluxes and the heat release from the eastern boundary. We assume that the diffusion term is dominated by the KC-related strong eddy mixing; thus changes of the KC transport are responsible for the heat content change in the Kuroshio Extension Region; the surface heat fluxes respond to, rather than drive the heat content anomalies. This result is consistent with the results of Kelly and Dong (2004) in which they found the heat content anomalies near the Kuroshio region lead to changes of the surface heat fluxes.

6.4.2 Atmospheric role in the North Pacific

To investigate the changes in the North Pacific, linear regressions are calculated between various variables and the MOC index (Fig. 6.18-21). The mean SLP and the wind stress pattern are shown in Fig. 6.17 for comparison.

There are two permanent low pressure centers, one in northwestern corner of the North Pacific and the other near Alaska (Fig. 6.17). The subtropical high is located near 30º N, 130º W.
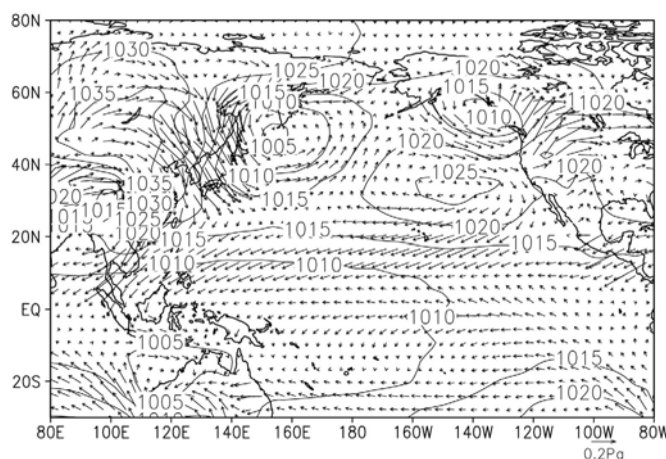

Fig. 6.17: mean wintertime SLP and surface wind stress in the North Pacific (unit: hPa)

The western North Pacific is covered by cold anomalies and an enhanced Aleutian Low controls the North Pacific at lag -30 (Fig. 6.18). While positive SLP anomalies gradually occupy the North Pacific, the cold anomalies move

eastward and turn to a southwest direction after reaching the North America coast, which eventually reach the western equatorial region and spread eastward. Warm anomalies appear near 40ºN at lag -20. These warm anomalies develop and spread to the northern North Pacific at lag 0.
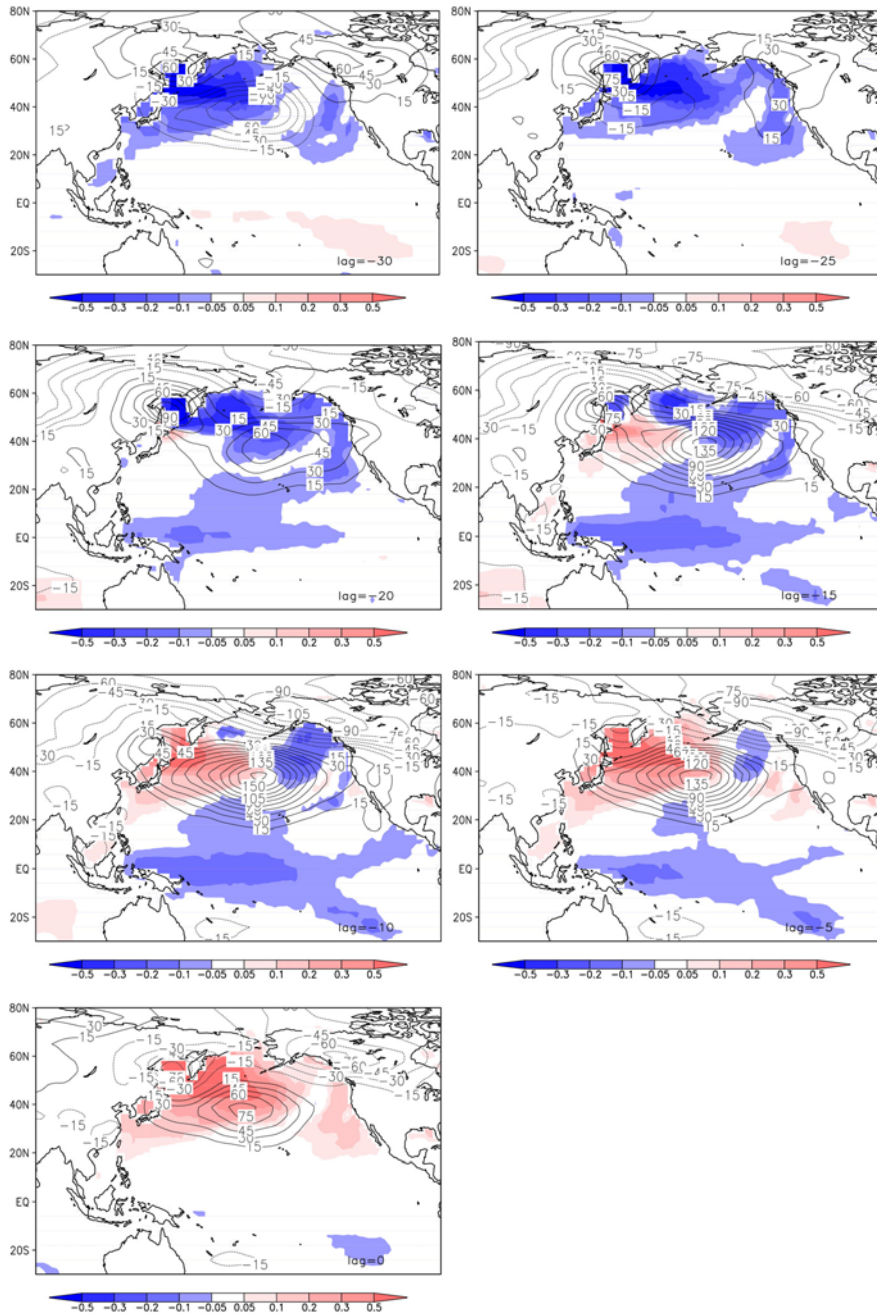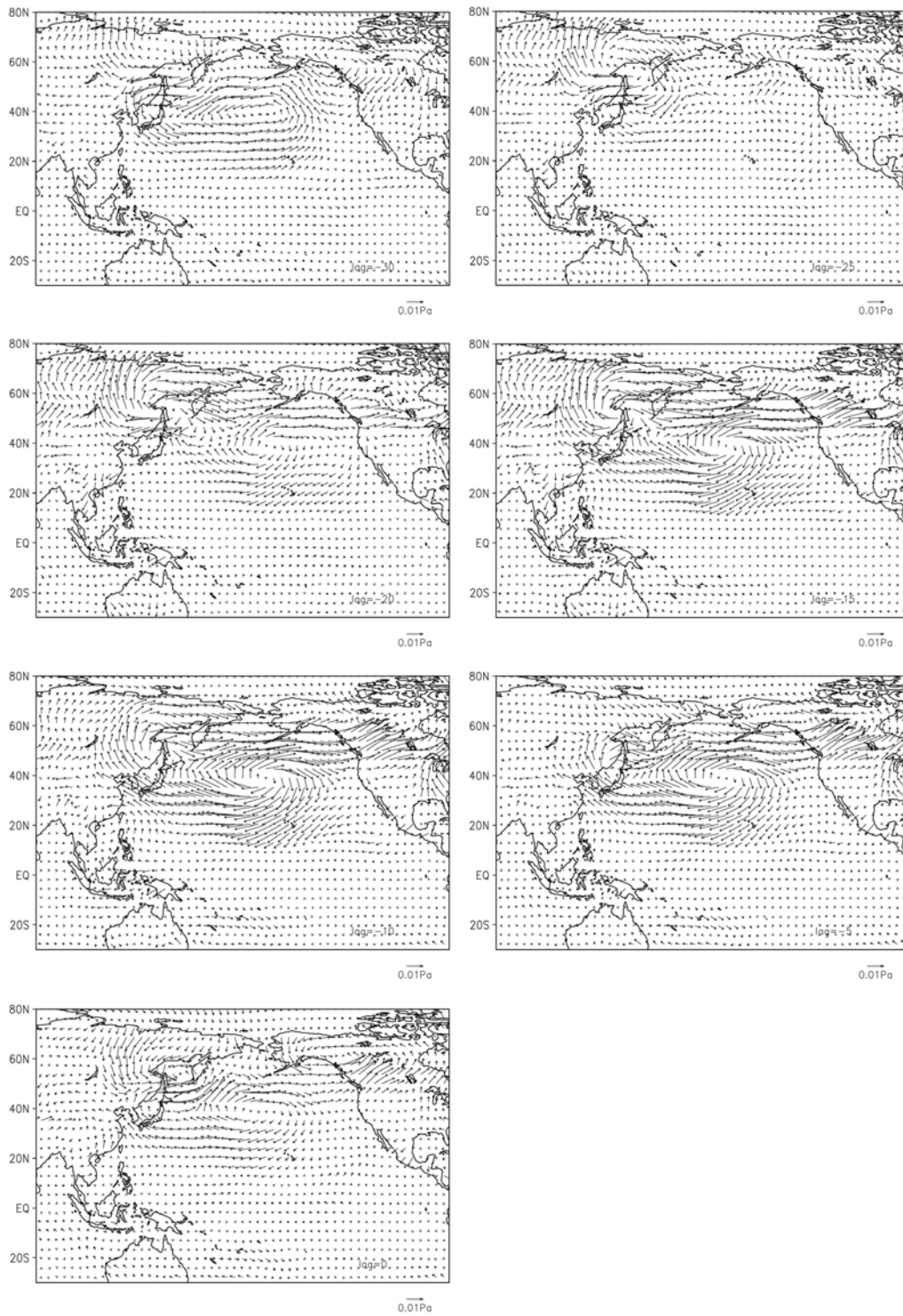

Fig. 6.18: same as Fig. 6.10 but for the North Pacific

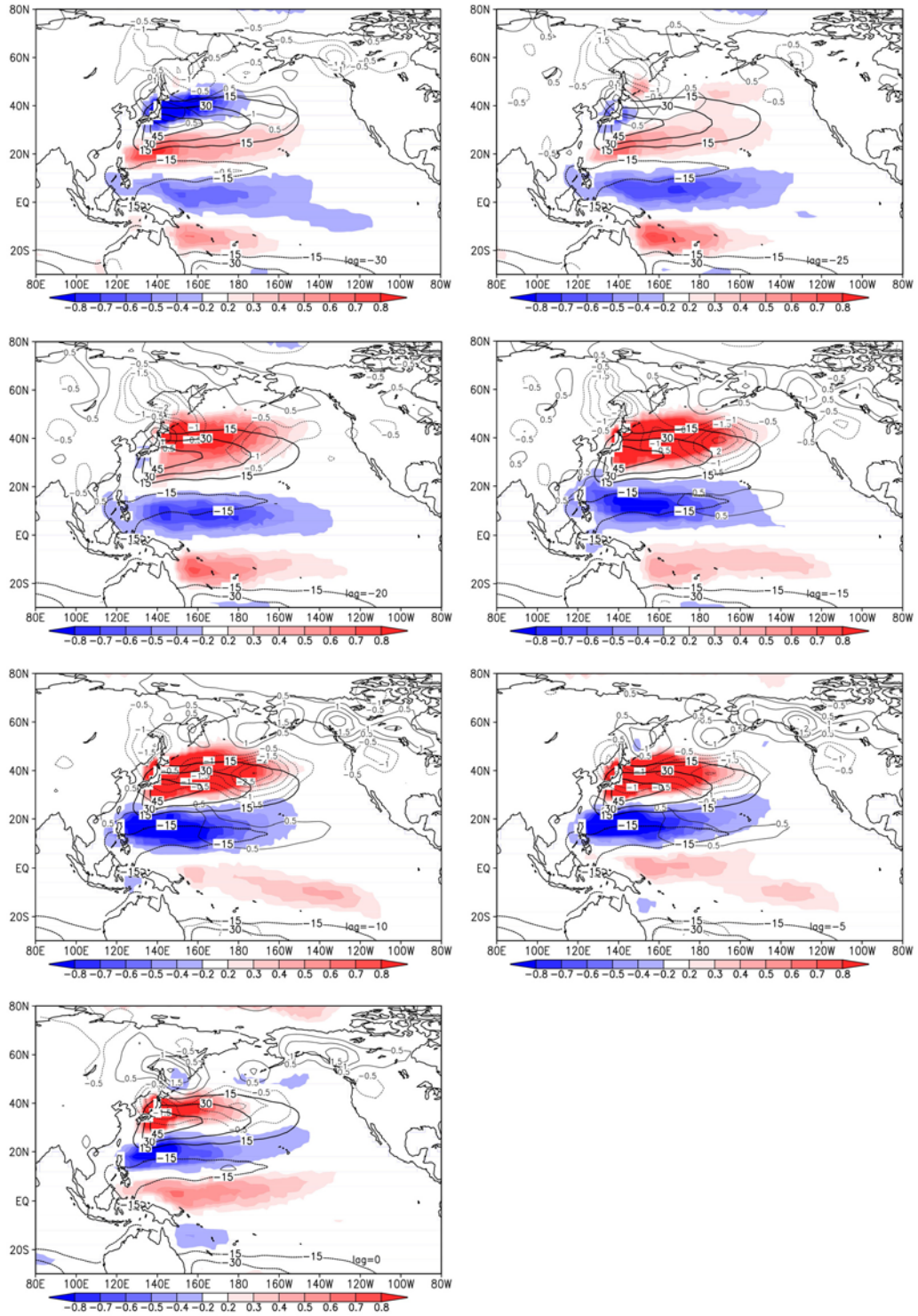Fig. 6.19: same as Fig. 6.11 but for the North Pacific

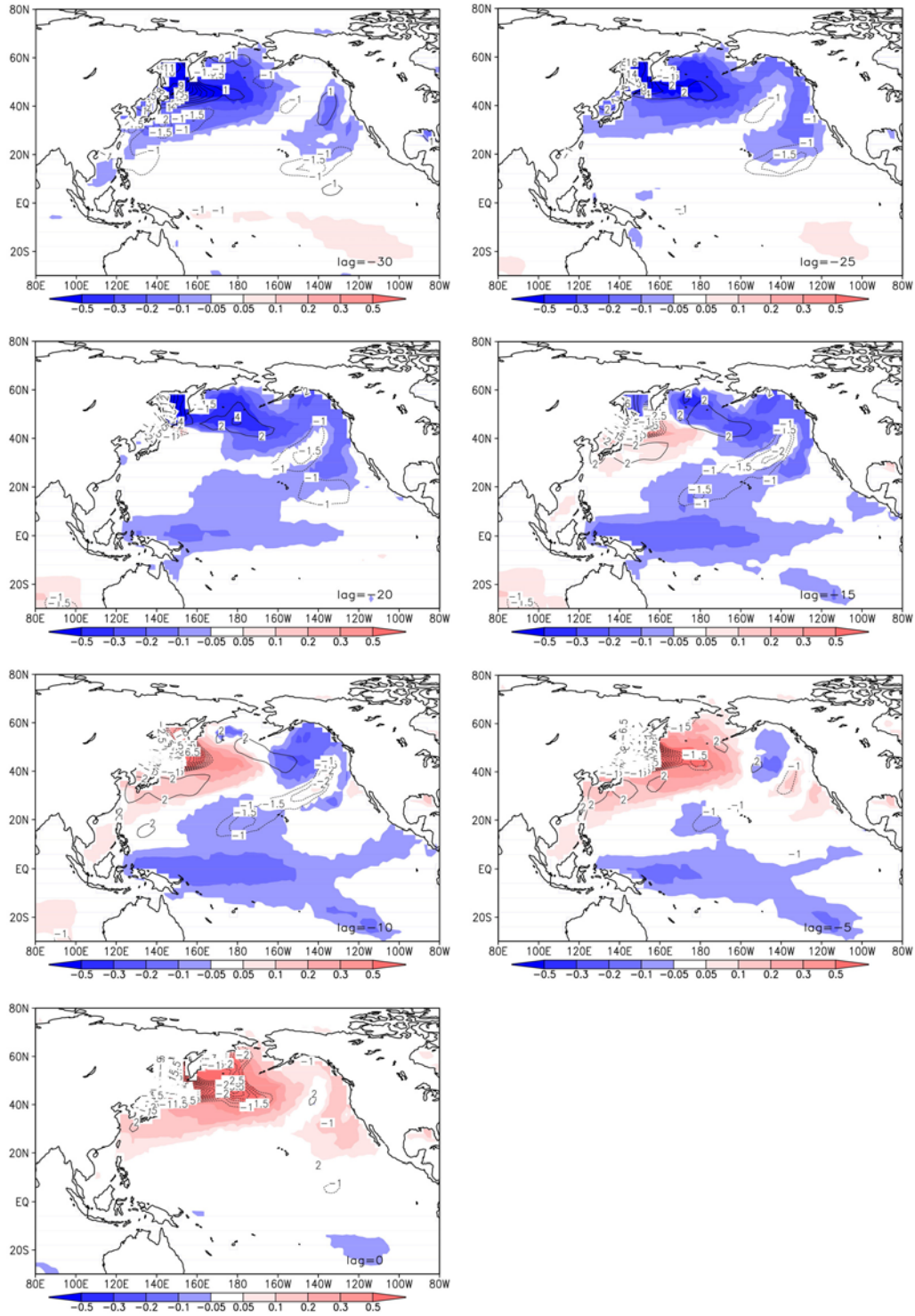Fig. 6.20: same as Fig. 6.12 but for the North Pacific.

Fig. 6.21: same as Fig. 6.13 but for the North Pacific

The associated wind stress leads to shifting of the gyre and changes in the north ward heat transport by the KC. At lag -30, the anomalous wind stress pattern (Fig. 6.19) shows a positive wind curl between 30º N and 40º N and a negative

wind stress curl between 40º N and 60º N (Fig. 6.20), which leads to an anomalous cyclone near the Kuroshio Extension Region (KER) and an anomalous anticyclone near the southern boundary of the subtropical gyre. This corresponds to a southward shift of the gyre and reduced northward heat transport by the KC which is responsible for the cold anomalies in the northern North Pacific. From lag -20 to lag 0, the KER is under a negative wind stress curl (Fig. 6.20), leading to the northward shift of the gyre and consequently enhanced northward heat transport by the Kuroshio Current, consistent with the prevailing warm anomalies. The important role of wind stress changes in affecting the horizontal heat transport in the Kuroshio Extension region has also been noted by previous studies (e. g., Kelly and Dong 2004).

The surface heat fluxes tend to damp the temperature anomalies in the North Pacific due to the varying northward heat transport of the KC (Fig. 6.21). For example, at lag -30, when the cold anomalies prevail in the North Pacific, there is anomalous oceanic heat gain near 40º N. When the warm anomalies develop at lag -15, anomalous heat loss appear and tends to damp the warm anomalies.

It is noteworthy that considerable variations take place also in the equatorial ocean circulation (Fig. 6.20) and surface temperature field (Fig. 6.21). Therefore the North Atlantic multidecadal variability has a potential to influence the equatorial Pacific region, suggesting that it may interact with ENSO events on multidecadal time scales.

6.4.3 Atmosphere bridge

One question arises: how the North Atlantic and the North Pacific are connected? The importance of wind stress to the ocean adjustment in the North Pacific highlights the atmospheric role. This connection is most likely associated with the prominent atmosphere mode — the Arctic Oscillation (AO) or Annular Mode.

Some studies argue that the AO may be a statistical artifact whereas the NAO bears a physical meaning (e. g. Ambaum et al. 2001), while others think the NAO is a regional manifestation of a hemispheric-wide pattern of variability referred to as the AO or the annular mode (Thompson and Wallace 1998; Thompson et al. 2000). The associated difficulty is that a close correlation between the Aleutian Low and the NAO is not always clear (Deser 2000), Ambaum et al. 2001 and Itoh 2002).

To evaluate the relation between the NAO, AO and the Aleutian Low, EOF analysis is calculated for the wintertime SLP field in the North Atlantic, the northern hemisphere (0-90°N), and the North Pacific (120°E-100°W, 20°N-60°N) respectively (Fig. 6.22). The wintertime SLP is the seasonal mean over December, January and February.

The NAO shows one sign of SLP anomalies over the Greenland and the opposite sign in the North Atlantic centered near the Mediterranean Region (Fig. 6.22a). The Arctic Oscillation shows anomalies of one sign over the Arctic and Greenland and an opposite sign in the North Atlantic and the North Pacific (Fig. 6.22b). The Aleutian Low appears as a monopole over the North Pacific (Fig. 6.22c). These three modes account for 68%, 58%, and 40% of the respective total variance.

The maximum correlation between the AO and the NAO is 0.95 and the correlation between the Aleutian Low and the NAO is about 0.5. Both exceed 95% confidence level (not shown). The weaker correlation between Aleutian Low index and the NAO index may be due to the contamination by other variability that is antisymmetric over the North Pacific and the North Atlantic, such as Pacific North America teleconnection (Wallace and Thompson 2002). Thus on multidecadal scales, changes of the NAO, AO and the Aleutian Low are closely related, which acts as an atmospheric bridge connecting the North Pacific with the North Atlantic.

The AO index (Fig. 6.22d) shows concentrated energy centered at 60 years and 16 years. We believe the 60-yr variability corresponds to the multidecadal coupled mode; the 16-yr variability has been found in previous studies and may be related to meandering of the Gulf Stream and the local air-sea coupling (Czaja and Marshall 2001). In comparison with the MOC wavelet plot (Fig. 4.4b), the AO index shows less energy near 30 yr supporting the ocean internal feature of this interdecadal variability.
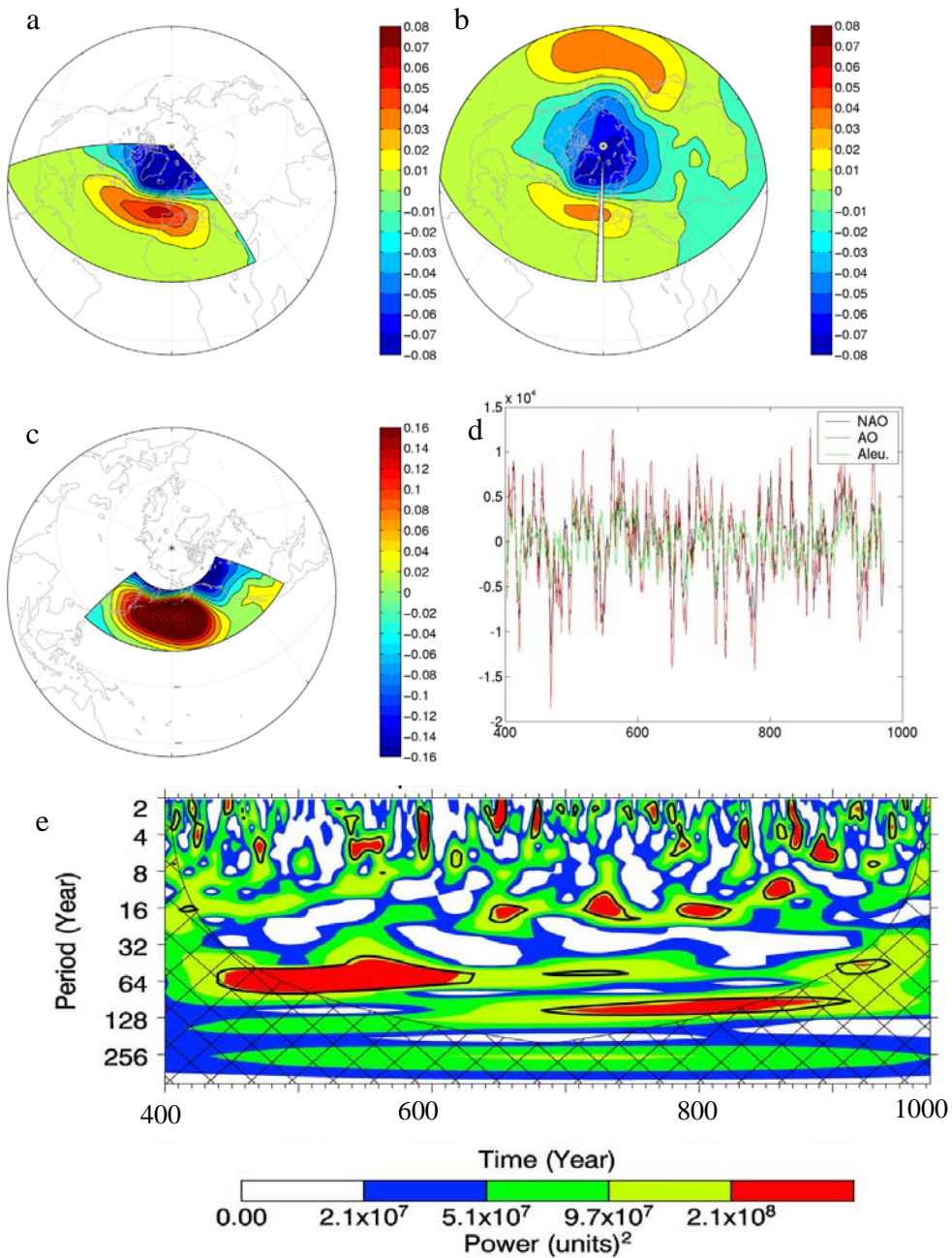
Fig. 6.22: the first EOF for the SLP in a) the North Atlantic ('NAO'), b) the Northern Hemisphere ('AO'), and c) the North Pacific (20°N-60°N) ('Aleu'). They account for 68%, 58%, and 40% of the respective total variance. d) The leading PCs. The black, red, green lines correspond to the one of NAO, AO, and Aleu.5 years running mean is applied. e) Wavelet analysis of the AO.

6.5 Summary and discussions

We have presented the multidecadal variability of the MOC as an air-sea coupled mode. The nature of this oscillation consists of the following ingredients:

1) The oscillation mechanism is due to the geostrophic response of the meridional and zonal overturning to propagation of the temperature anomalies along the subpolar front and the cyclonic subpolar gyre. Thus the time scale is set by the ocean.

2) The associated SST anomalies forces anomalous atmospheric circulation with a similar spatial pattern. These atmospheric circulations directly force the subpolar gyre through the wind stress and surface heat fluxes in the Labrador Basin and affect the deep convection. This coupling increases the haline contribution near the surface to density anomalies which enhance the thermal effects in intermediate depth and hence act as a positive feedback.

The SST anomalies transfer the spatial pattern to the atmosphere. Note that this spatial pattern is not a standing wave pattern of the NAO. The SST anomalies first appear near the subpolar front region due to the varying NAC transport and propagate to the eastern subpolar gyre and the GIN Sea first which leads to an east-west dipole SLP pattern. When the temperature anomalies move westward and occupy the Labrador Basin while south of the NAC is occupied by SST anomalies with an opposite sign, north-south dipole SST anomalies form and

excite a NAO-like atmospheric pattern.

The ocean dynamics in 1) is basically similar to the one associated with the interdecadal variability of the MOC (chapter 5), consistent with results from less complex models by Te Raa and Dijkstra (2002). This process is associated with temperature anomalies. However, in the Labrador Sea, near-surface salinity resulting from deep convection contributes positively to enhancing the thermal effects in the intermediate depths. This haline contribution is amplified by the air-sea coupling, which is critical to the existence of a significant MDV mode. The contribution of the surface freshwater fluxes is negligible. This is different from the results of Timmermann et al. (1998) in which the NAO changes the surface salinity anomalies in the deep convection sites via surface freshwater fluxes.

The Aleutian Low is closely related to the anomalous atmospheric circulation in the North Atlantic, which can be described by the Antarctic Oscillation. Through this atmospheric bridge, the multidecadal oscillation of the MOC influences the North Pacific mainly through the wind stress changes which leads to variation of the Kuroshio Current transport and consequently heat content in the upper ocean in the northern North Pacific. At the same time, the atmosphere damps the heat content anomalies through surface heat fluxes. It is important to note that considerable changes are observed in the equatorial Pacific region. This indicates that the MDV has a potential to influence ENSO.

Chapter 7

Summary and synthesis

Summary and syntheses

In this thesis, the variability of the Meridional Overturning Circulation is investigated, particularly focusing on the variability on inter- to multi-decadal time scales.

In chapter 3, a general view of the variability of the MOC is investigated using two state-of-the-art numerical GCMs: ECHAM5/MPIOM and GFDL CM2.1. This work is initiated by the ongoing discussion about the spectral characteristics of the MOC. So far, a general picture of the MOC spectrum hasn't been achieved yet. It has been assumed to follow the red-noise spectrum (von Storch et al., 2000), with increasing spectrum toward low frequency shown as f^{-2} power law scaling which levels off at low frequencies due to negative feedbacks in the system. Although it has been reported that in a different model the MOC shows power law scaling with $\beta \approx 1$ up to millennia (Blender et al. 2006), the discrepancy on the MOC spectral behavior hasn't attracted enough attention.

We find that the ECHAM5/MPIOM and GFDL show similar MOC spectral behaviors. In the North Atlantic, the MOC spectrum is featured as white noise from months to years and from decades to centuries which are separated by f^{-1} power-law scaling from years to decades. However, this f^{-1} power law scaling extends up to centuries in a coarse-resolution simulation of ECHAM5/MPIOM.

Chapter 4-6 focus on investigating the physical mechanism of the variability of the MOC on inter-to-multidecadal time scales. Chapter 4 shows that there are two oscillations coexisting in the fully coupled atmosphere-ocean-sea-ice system: the interdecadal variability (IDV, from 20-45 years) and the multidecadal variability (MDV, from 45 to 80 years). The IDV exists in the ocean-only model driven by climatological month-to-month surface fluxes, thus

it is an ocean internal mode; the MDV can only exist with the presence of the air-sea coupling. There are indications of possible interactions between IDV and MDV so that when IDV is stronger, MDV tends to be damped and vice versa.

Chapter 5 shows that IDV is associated with large-scale horizontal density gradients in the ocean. Temperature dominates density changes, and the propagation of temperature anomalies along the subpolar front and in the subpolar gyre leads to changes in the east-west and north-south density gradients which in turn control the variation of the meridional and zonal streamfunction. We find that along the subpolar front it is the LSW at intermediate depth which eventually controls the speed of the temperature anomalies and sets the time scale of the east-west density gradient transition. The similarity between the IDV in MPIOM and the ocean-internal mode in less complex models (Te Raa and Dijkstra, 2002, 2003) suggests that the ocean-internal IDV is quite robust.

Chapter 6 shows MDV as an air-sea coupled mode. Similar to IDV, MDV is also associated with changes in east-west and north-south density gradients and consequently the adjustment of the meridional and zonal streamfunction. However, to obtain a significant spectral MDV peak, the air-sea coupling, more specifically, the fast response of the gyre in the Labrador Sea to the anomalous wind stress, is necessary. Lack of this coupling explains the absence of MDV in experiment RAND. The importance of this fast wind driven positive feedback has also been noted by Eden and Greatbatch (2003) as a unique characteristic of a coupled oscillation.

In summary, we investigated the spectral scaling and periodicities of the simulated MOC. We find that two modern models show more often f^{-1} power law scaling from years to decades, instead of f^{-2} associated with the Lorentzian spectrum. Furthermore, this f^{-1} power law scaling may extend up to centuries as

simulated by a coarse-resolution simulation of ECHAM5/MPIOM. It is not clear whether the f^{-1} power-law scaling is unique to the two models analyzed here, therefore, analyses with other models are planned in future studies. The other concern is what leads to the difference between the two simulations with ECHAM5/MPIOM. In further studies three factors will be considered: resolution, cloud scheme, and the feedback of ocean currents on wind stress, which distinguish the two simulations of ECHAM5/MPIOM.

Our results call for caution when the AR (1) process is assumed as the background noise and used as the significance test to identify 'significant' peaks. As is shown in chapter 4, the spectral energy of the MDV, an important part of the power-law scaling, is enhanced by the air-sea coupling, which suggests that the presence of the power law scaling may depend largely on how well the models simulate a 'right' interaction between different components. This aspect should be considered to test the model performance.

We find IDV and MDV coexisting in the climate system. This result provides a new explanation to the wide-spread time scales associated with the 'Atlantic Multidecadal Oscillation' in observational data; the various time scales may correspond to different physical modes in the system. We think that the relatively short runs in previous studies prohibited a clear separation between different modes. For example, Delworth and Greabatch (2000) have noticed that the 'multidecadal' oscillation had different time scales in their fully coupled model and their ocean-only experiment with stochastic atmospheric forcing ('RANDOM'). However, it was difficult to test whether the period shift was statistically significant due to the limited length of the integrations (400 yrs). Therefore, in future studies analyses should be conducted with longer runs.

Our analyses on the ocean internal mode are based on the ocean-only experiment driven by climatological forcing. This idealized experiment set-up determines that it is not easy to make a direct comparison between our

interdecadal mode and observational data, if available. But a nice element in this study is that changes in the meridional and zonal streamfunction can be related to changes in the vertically integrated east-west and north-south density gradients on both inter- and multi-decadal time scales. This motivates observation of the horizontal density gradients over a long time scale from which, according to our studies, the state of the ocean circulation can be derived. The mechanism proposed can be verified by comparing the derived state of the ocean circulation with reconstructed MOC state using observational data (Baehr, 2006).

One concern is that in our studies temperature dominates density changes: near the surface salinity enhances temperature-contributed density anomalies, as a consequence of deep convection; but in intermediate depth, it works against thermal effects. However, salinity can turn out to be the dominant factor in determining density changes. For example, Timmermann et al. (1998) identified a 35-yr oscillation as an air-sea coupled mode in which salinity associated with surface freshwater input controls the weakening and strengthening of the MOC. If salinity dominates density changes, the oscillation will be different from what we have found. Therefore, the relative role of temperature and salinity needs to be evaluated in observational data.

Our studies show that the changes in the North Atlantic may have large impact on the North Pacific through the atmosphere bridge which can be described by the Antarctic Oscillation. On the other hand, Wu and Liu (2005) suggested that the North Pacific can impact the North Atlantic climate variability substantially. Moreover, considerable changes are observed in the equatorial Pacific region, suggesting the North Atlantic variability has a potential to interact with ENSO at low frequencies. Therefore, climate modes dominating in each basin may be interlinked. This interlinking can be achieved through ocean wave adjustments (Timmermann et al. 2005), or/and through the atmosphere.

One shortcoming of our studies is that we consider only linear aspects which can not explain why when IDV is stronger MDV tends to be weaker and vice versa (Fig. 4.4b). This alternate dominance of different physical modes may contribute to different climate regimes (Raible et al. 2001, 2004). How to analyze the nonlinear climate system will remain a big challenge in the near future.

Bibliography

1.   Ambaum, M. H. P., B. J. Hoskins, and D. B. Stephenson, 2001: Arctic oscillation or North Atlantic oscillation? *J. Clim.*, 14, 3495–3507.

2.   Andronova N G., and M. E. Schlesinger, 2000: Causes of global temperature changes during the 19th and 20th centuries [J]. *Geophys. Res. Lett.*, 27(14): 2 137-2 140.

3.   Arakawa, A., and V. R. Lamb, 1977: Computational design of the basic dynamical processes of the UCLA general circulation model. *Methods in Comput. Phys.*, 17, 173-265.

4.   Baehr, J., 2006: Monitoring and detecting changes in the meridional overturning circulation at 26° N in the Atlantic Ocean — The simulation of an observing array in numerical models. *PhD dissertation*, Max Planck Institute für Meteorology, University of Hamburg.

5.   Balan, S. B., 2006: Effect of daily surface flux anomalies on the time-mean oceanic circulation. *PhD dissertation*, Max Planck Institute für Meteorology, University of Hamburg.

6.   Barbosa, S. M., M. J. Fernandes, and M. E. Silva, 2006: Long range dependence in North Atlantic sea level. *Physica A: Statistical Mechanics and its Applications*, 371, 725-731.

7.   Blender, R., K. Fraedrich, and B. Hunt, 2006: millennial climate variability: simulation and Greenland ice cores, *Geophys. Res. Lett.*, 33, L04710. doi: 10.1029/2005GL024919.

8.   Blender, R., and K. Fraedrich, 2003: Long time memory in global warming simulations, *Geophys. Res. Lett.*, 30, 1769-1772. doi:10.1029/2003GL017666.

9.   Bjerknes, J., 1964: Atlantic air–sea interaction. *Adv. Geophys.*, Vol. 10, Academic Press, 1–82.

10.   Capotondi, A., and R. Saravanan, 1996: Sensitivity of the thermohaline

circulation to surface buoyancy forcing in a two-dimensional ocean model. *J. Phys. Oceanogr.*, 26, 1039-1058.

11. ——, and W. R. Holland, 1997: Decadal variability in an idealized ocean model and its sensitivity to surface boundary conditions. *J. Phys. Oceanogr.*, 27, 1072-1093.

12. Colin de Verdière, A., and T. Huck, 1999: Baroclinic instability: An oceanic wave-maker for interdecadal variability. *J. Phys. Oceanogr.*, 29, 893–910.

13. Collins, M., Botzet, M., Carril, A., Drange, H., Jouzeau, A., Latif, M., Otteraa, O. H., Pohlmann, H., Sorteberg, A., Sutton, R., and Terray, L., 2006: Interannual to decadal climate predictability: A multimodel-ensemble study. *J. Clim.*, 19, 1195-1203.

14. Cooper, C. and C. Gordon, 2002: North Atlantic oceanic decadal variability in the Hadley Centre coupled model. *J. Clim.*, 15; 45-72.

15. Curry, Ruth G., and M. S. McCartney, 2001. Ocean gyre circulation changes associated with the North Atlantic oscillation. *J. Phys. Oceanogr.*, 31(12), 3374 – 3400.

16. Czaja, A., and J. Marshall, 2001: Observations of atmosphere-ocean coupling in the North Atlantic. *Quart. J. Roy. Meteor. Soc.*, 127:1893-1916.

17. ——, and C. Frankignoul, 2002: Observed impact of North Atlantic SST anomalies on the North Atlantic Oscillation. *J. Clim.*, 15, 606–623.

18. ——, A. W. Robertson, and T. Huck, 2003: The role of Atlantic ocean–atmosphere coupling in affecting North Atlantic Oscillation variability. The North Atlantic Oscillation: Climatic Significance and Environment Impact, *Geophys. Monogr.*, Vol. 134, Amer. Geophys. Union, 147–172.

19. Delworth, T. L., 1996: North Atlantic interannual variability in a coupled ocean-atmosphere model. *J. Clim.*, 9(10), 2356-2375.

20.　——, A. J. Broccoli, Rosati A, R. J. Stoufer, V. Balaji, J. A. Beesley, W. F. Cooke, K. W. Dixon, J. Dunne, and K. A. Dunne, 2006: GFDL's CM2 global coupled climate models. Part I: Formulation and simulation characteristics, *J. Clim.*, 19, 643-674.

21.　——, and R. J. Greatbatch, 2000: Multidecadal thermohaline circulation variability driven by atmospheric surface flux forcing. *J. Clim.*, 13, 1481–1495.

22.　——, S. Manabe, and R. J. Stouffer, 1993: Interdecadal variations in the thermohaline circulation in a coupled ocean–atmosphere model. *J. Clim.*, 6, 1993–2010.

23.　——, S. Manabe, and R. J. Stouffer, 1997: Multidecadal climate variability in the Greenland Sea and surrounding regions: a coupled model simulation. *Geophys. Res. Lett.*, 24(3), 257-260.

24.　Deser C., 2000: On the teleconnectivity of the "Arctic oscillation". *Geophys. Res. Lett.*, 27, 779–782.

25.　——, and M. L. Blackmon, 1993: Surface climate variations over the North Atlantic Ocean during winter: 1900–1993. *J. Clim.*, 6, 1743–1753.

26.　Dickson R. R., J. Lazier, J. Meincke, et al., 1996: Long-term coordinated changes in the convective activity of the North Atlantic. *Prog. Oceanogr.*, 38(3): 241～295.

27.　Dong, B., and R. T. Sutton, 2005: Mechanism of Interdecadal Thermohaline Circulation Variability in a Coupled Ocean–Atmosphere GCM. *J. Clim.*, Vol. 18, No. 8, pp. 1117–1135.

28.　Döscher, R., C. W. Böning, and P. Herrmann, 1994: Response of circulation and heat transport in the North Atlantic to changes in Thermohaline forcing in northern latitudes: a model study. *J. Phys. Oceanogr.*, 24, 2306-2320.

29.　Eden, C., and R. J. Greatbatch, 2003: A damped decadal oscillation in the North Atlantic climate system. *J. Clim.*, 16, 4043-4060.

30. ——, R. J. Greatbatch, and J. Lu, 2002: Prospects for decadal prediction of the North Atlantic Oscillation (NAO), *Geophys. Res. Lett.*, 29(10), doi: 10.1029/2001GL014069.

31. ——, and T. Jung, 2001: North Atlantic interdecadal variability: Oceanic response to the North Atlantic Oscillation (1865-1997), *J. Clim.*, 14, 676-691.

32. ——, and J. Willebrand, 2001: Mechanism of interannual to decadal variability of the North Atlantic circulation. *J. Clim.*, 14, (10), 2266-2280.

33. Fischer, J., and Schott, F., 2002: Labrador Sae Water tracked by profiling floats - from the boundary current into the open North Atlantic. *J. Phys. Oceanogr.*, 32, 573-584.

34. Frankignoul, C., P. Müller, and E. Zorita, 1997: A simple model of the decadal response of the ocean to stochastic wind forcing. *J. Phys. Oceanogr.*, 27, 1533–1546.

35. Fraedrich, K., and R. Blender, 2003: Scaling of atmosphere and ocean temperature correlations in observations and climate models, *Phys. Rev. Lett.*, 90, 108510-(1-4).

36. ——, U. Luksch, and R. Blender, 2004: 1/f-model for long time memory of the ocean surface temperature, *Phys. Rev. E*, 70, 037301. doi: 10.1103/PhysRevE.70.037301

37. Gent, P. R., J. Willebrand, T. McDougall, and J. C. McWilliams, 1995: Parameterizing eddy-induced tracer transports in ocean circulation models. *J. Phys. Oceanogr.*, 25, 463–474.

38. Gnanadesikan, A., and Coauthors, 2006: GFDL's CM2 global coupled climate models. Part II: The baseline ocean simulation. *J. Clim.*, 19, 675–697.

39. Goodman, P. J., 2001: Thermohaline adjustment and advection in an. OGCM, *J. Phys. Oceanogr.*, 31, 1477–1497.

40. Gray S. T., J. L. Betancourt, C. L. Fastie, and S. T. Jackson, 2003: Patterns and sources of multidecadal oscillations in drought-sensitive tree-ring records from the central and southern Rocky Mountains, *Geophys. Res. Lett.*, 30 (6), 1316, doi:10.1029/2002GL016154.

41. Gray, S.T., L.J. Graumlich, J.L. Betancourt, and G.D. Pederson，2004: A tree-ring based reconstruction of the Atlantic Multidecadal Oscillation since 1567 A.D. *Geophys. Res. Lett.*, 31:L12205, doi:10.1029/2004GL019932.

42. Greatbatch, R. J., and K. A. Peterson, 1996: Interdecadal variability and oceanic thermohaline adjustment. *J. Geophys. Res.*, 101, 20467–20482.

43. ——, and S. Zhang, 1995: An interdecadal oscillation in an idealized ocean basin forced by constant heat flux. *J. Clim.*, 8, 82–91.

44. Griffies, S. M., 1998: The Gent–McWilliams skew flux. *J. Phys. Oceanogr.*, 28, 831–841.

45. ——, and K. Bryan, 1997: Predictability of North Atlantic multidecadal climate variability. *Science*, 275(5297), 181-184.

46. ——, and E. Tziperman, 1995: A linear thermohaline oscillator driven by stochastic atmospheric forcing. *J. Clim.*, 8(10), 2440-2453.

47. ——, M. J. Harrison, R. C. Pacanowski, and A. Rosati, 2003: A technical guide to MOM4. *GFDL Ocean Group Tech. Rep. 5*, NOAA/Geophysical Fluid Dynamics Laboratory, Princeton, NJ, 295 pp.

48. ——, A. Gnanadesikan, K. W. Dixon, J. P. Dunne, R. Gerdes, M. J. Harrison, A. Rosati, J. L. Russell, B. L. Samuels, M. J. Spelman, M. Winton, and R. Zhang, 2005: Formulation of an ocean model for global climate simulations. *Ocean Science*, 1, 45–70.

49. Haines and Old, 2005: Diagnosing Natural Variability of North Atlantic Water Masses in HadCM3. *J. Clim.*, 18, 1925-1941.

50. Hakkinen, S., 1999: Variability of the simulated meridional heat transport in the North Atlantic for the period 1951-1993. *J. Geophys. Res.*, 104(C5),

10,991-11,007.

51. ——, 2000: Decadal air-sea interaction in the North Atlantic based on observations and modeling results. *J. Clim.*, 13(6), 1195-1219.

52. Halliwell, G., 1998: Simulation of North Atlantic decadal/multi-decadal winter SST anomalies driven by basin-scale atmospheric circulation anomalies. *J. Phys. Oceanogr.*, 28, 5-21

53. Hansen, D. V., and H. F. Bezdek, 1996: On the nature of decadal anomalies in the North Atlantic sea surface temperature. *J. Geophys. Res.*, 101, 9749-9758.

54. Hasselmann, K., 1976: Stochastic climate models. Part I: Theory, *Tellus*, 28, 473-484.

55. Hátún, H., A. B. Sandø, H. Drange, B. Hansen, and H. Valdimarsson, 2005: Influence of the Atlantic Subpolar Gyre on the Thermohaline Circulation , *Science*, 309, 1841-1844.

56. Hibler,W. D., III, 1979: A dynamic thermodynamic sea ice model. *J. Phys. Oceanogr.*, 9, 815–846.

57. Hoerling, M. P., J. Hurrell, and T. Xu, 2001: Tropical origins for North Atlantic climate change. *Science*, 292, 90-92.

58. Hogg NG, G. Siedler, W. Zenk, 1999: Circulation and variability at the southern boundary of the Brazil Basin. *J. Phys. Oceangr.*, 29(2), 145-157.

59. Huang, R. X., W. Wang, and L. L. Liu, 2006: Decadal variability of wind-energy input to the world ocean. *Deep-Sea Res.* II, 53, 31-41.

60. Huck, T., A. Colin de Verdiere, and A. J. Weaver, 1999: Decadal variability of the thermohaline circulation in ocean models. *J. Phys. Oceanogr.*, 29, 893-910.

61. ——, G K. Vallis, 2001: Linear stability analysis of the three-dimensional thermally-driven ocean circulation: application to interdecadal oscillations. *Tellus A-Dyn, Meteorol Oceanol*, 53: 526-545.

62. Hurrell, J. W., 1995: Decadal trends in the North Atlantic Oscillation:

regional temperature and precipitation. *Science*, 269,676-679.

63. Huybers, P., and W. Curry, 2006: Links between annual, Milankovitch and continuum temperature variability, *Nature*, 444, 329-332.

64. Itoh, H. 2002: True versus apparent arctic oscillation. *Geophys. Res. Lett.*, 29-29..

65. Jayne, S. R., and J. Marotzke, 2001: The dynamics of wind-induced ocean heat transport, *Rev. Geophys.*, 39, 385-411.

66. Junge, M., and K. Fraedrich, 2006: Temperature anomalies in the northeastern North Atlantic: Subpolar and subtropical precursors on multiannual time scales, *J. Clim.*, 19, in press.

67. Jungclaus et al., 2005: Arctic-North Atlantic interactions and multidecadal variability of. the meridional overturning circulation. *J. Clim.*, 18, 4013-4031.

68. ——, N. Keenlyside, M. Botzet, H. Haak, J.-J. Luo, M. Latif, J. Marotzke, U. Mikolajewicz and E. Roeckner. 2006: Ocean Circulation and Tropical Variability in the Coupled Model ECHAM5/MPI-OM. *J. Clim.*, Vol. 19, No. 16, pp. 3952–3972.

69. Kantelhardt J. W., E. Koscielny-Bunde, D. Rybski, P. Braun, A. Bunde, and S. Havlin, 2006: Long-term persistence and multifractality of river runoff and precipitation records. *J. Geophys. Res.* (Atmosph.), 111, D01106.

70. Kelly, K. A., and S. Dong, 2004: The relationship of western boundary current heat transport and storage to mid-latitude ocean-atmosphere interaction, in Earth's Climate: The Ocean-Atmosphere Interaction, *American Geophysical Union Geophysical Monograph 147*, edited by C. Wang, S.-P. Xie, and J. A. Carton, pp. 347-363.

71. Kerr, R. A., 2000: A North Atlantic climate pacemaker for the centuries. *Science*, *288*, 1984-1986.

72. Kirchner, Ingo, Georgiy L. Stenchikov, Hans-F. Graf, Alan Robock and

Juan Carlos Antuña, 1999: Climate model simulation of winter warming and summer cooling following the 1991 Mount Pinatubo volcanic eruption. *J. Geophys. Res.*, 104, 19,039-19,055.

73. Knight, J. R., R. J. Allan, C. Folland, M. Vellinga, and M. E. Mann, 2005: A signature of persistent natural thermohaline circulation cycles in observed climate. *Geophys. Res. Lett.*, ***32***, L20708, doi:10.1029/2005GL024233.

74. ——, C. K. Folland, and A. A. Scaife, 2006: Climate impacts of the Atlantic Multidecadal Oscillation. *Geophys. Res. Lett.*, L17706, doi:10.1029/2006GL026242.

75. Kushnir, Y., 1994: Interdecadal variations in North Atlantic sea surface temperature and associated atmospheric conditions. *J. Clim.*, 7, 142–157.

76. Latif M., 2001: Tropical Pacific/Atlantic Ocean interactions at multi-decadal time scales. *Geophys. Res. Lett.*, 28 , 539-542.

77. ——, C. Böning, J. Willebrand, A. Biastoch, J. Dengg, N. Keenlyside, and U. Schweckendiek, 2006: Is the thermohaline circulation changing? *J. Clim.*, 19, 4631-4637.

78. ——, E. Roeckner, U. Mikolajewicz and R. Voss, 2000: Tropical stabilization of the thermohaline circulation in a greenhouse warming simulation. *J.Clim.*, 13, 1809-1813.

79. ——, et al., 2004: Reconstructing, monitoring, and predicting. multidecadal scale changes in the North Atlantic thermohaline circulation with sea surface. temperatures. *J. Clim.*, 17, 1605-1614.

80. ——, and T P. Barnett, 1996: Decadal climate variability over the North Pacific and North America: Dynamics and predictability. *J Clim.*, 9: 2407-2 423.

81. Levitus, S., 1989: Interpentadal variability of temperature and salinity at intermediate depths of the North Atlantic Ocean, 1970-74 versus 1955-59, *J. Geophys. Res.*, 94, 6091～6131.

82.   Lilly, J.M. and P.B. Rhines, 2002: Coherent eddies in the Labrador Sea observed from a. mooring, *J. Phys.Oceanogr.*, 32, 585-598. 64.

83.   MacMynowski, D. G., and E. Tziperman, 2006. Two-way feedback interaction between the thermohaline and wind-driven circulations, *J. Phys. Oceanogr.*, 36, 5, 914-929.

84.   Mann M E, J. Park, and R. Bradley, 1995: Global interdecadal and century-scale oscillations during the past five centuries. *Nature,* 378: 266～270.

85.   Marotzke, J., 1990: Instabilities and multiple equilibria of the thermohaline circulation. *Ph.D. dissertation*, Institut für Meereskunde, Christian-Albrechts Universität, 126 pp.

86.   ——, and B. A. Klinger, 2000: The dynamics of equatorially asymmetric thermohaline circulations. *J. Phys. Oceanogr.*, 30, 955-970.

87.   Marsland, S.J., H. Haak, J.H. Jungclaus, M. Latif, and F. Röske, 2003: The Max- Planck- Institute global ocean/sea ice model with orthogonal curvilinear coordinates. *Ocean Model.*, 5, 91-127.

88.   McCartney, M. S., and Lynne D. Talley, 1982. The Subpolar Mode Water of the North Atlantic Ocean. *J. Phys. Oceanogr.*, 12, 1169-1188.

89.   ——, R.G. Curry, and H.F. Bezdek, 1996: North Atlantic's transformation pipeline chills and redistributes subtropical water, *Oceanus*, 39, 19-23.

90.   Mikolajewicz, U., and E. Maier-Reimer, 1990: Internal secular variability in an ocean general circulation model. *Clim. Dyn.*, 4, 145-156.

91.   Minobe, S. 1997: A 50-70 year climatic oscillation over the North Pacific and North America. *Geophys. Res. Lett.*, Vol 24, pp 683-686.

92.   Murray, R. J., 1996: Explicit generation of orthogonal grids for ocean models. *J. Comput. Phys.*, 126, 251–273.

93.   Mysak LA, D. K. Manak, and R. G. Marsden, 1990: Sea-ice anomalies observed in the Greenland and Labrador Seas during 1901-1984 and their relation to an interdecadal arctic climate cycle[J]. *Clim. Dyn.*,

5(2):111-133.

94. Nikolopoulos, A., K. Borena¨s, R. Hietala, and P. Lundberg, 2003: Hydraulic estimates of Denmark Strait overflow. *J. Geophys. Res.*, 108(C3), 3095, doi: 10.1029/2001JC001283.

95. Ogi M., Yoshihiro Tachiba, and Koji Yamazaki, 2004: The Connectivity of the Winter North Atlantic Oscillation (NAO) and the Summer Okhotsk High. *J. Meteorol. Soc. Jpn.*, Vol. 82, No. 3, pp. 905--913.

96. Pacanowski, R. C., and S. G. H. Philander, 1981: Parameterization of vertical mixing in numerical models of tropical oceans. *J. Phys. Oceanogr.*, 11, 1443–1451.

97. Pelletier, J. D., and D. L. Turcotte, 1997: Long-range persistence in climatological and hydrological time series: analysis, modeling and application to drought hazard assessment, *J. Hydrol.*, 203, 198– 208.

98. Peng, C.-K., S. V. Buldyrev, S. Havlin, M. Simons, H. E. Stanley, and A. L. Goldberger, 1994: On the mosaic organization of DNA sequences, *Phys. Rev. E*, 49, 1685-1689.

99. Pickart, R.S., D.T. Torres, and R. A. Clarke, 2002: Hydrography of the Labrador Sea during active convection. *J. Phys. Oceanogr.*, 32, 428-457.

100. ——, M. A. Spall, M. H. Ribergaard, G. W. K. Moore, and R. F. Milliff, 2003: Deep convection in the Irminger Sea forced by the Greenland tip jet. *Nature*, 424, 152−156.

101. Pohlmann, H., and M. Latif, 2005: Atlantic versus Indo-Pacific influence on Atlantic-European climate. *Geophys. Res. Lett.*, 32, L05707, doi:10.1029 / 2004GL021316.

102. ——, Sienz, F., and M. Latif, 2006: Influence of the multidecadal Atlantic meridional overturning circulation variability on European climate. *J. Clim.*, 19, 6062-6068.

103. Raible, C. C., U. Luksch, K. Fraedrich, and R. Voss, 2001: North Atlantic decadal regimes in a coupled GCM simulation. *Clim. Dyn.*, 18, 321-330.

104. ——, U. Luksch, and K. Fraedrich, 2004: Precipitation and Northern Hemisphere Regimes, *Atmos. Sci. Lett.*, **5**, 43-55.

105. Redi, M.H., 1982: Oceanic isopycanal mixing by coordinate rotation. *J. Phys. Oceanogr.*, 12, 1154-1158.

106. Rind, D., 2002: The Sun's role in climate. *Science*, 296: 673-677.

107. Rivin, I., and E. Tziperman, 1997: Linear versus self-sustained interdecadal thermohaline variability in a. coupled box model, *J. Phys. Oceanogr.*, 27(7), 1216–1232.

108. Robertson, A.W., C.R. Mechoso, and Y.-J. Kim, 2000: The influence of Atlantic sea surface temperature anomalies on the North Atlantic Oscillation. *J. Clim.*, 13, 122-138.

109. Roeckner, E., G. Bäuml, L. Bonaventura, R. Brokopf, M. Esch, M. Giorgetta, S. Hagemann, I. Kirchner, L. Kornblueh, E. Manzini, A. Rhodin, U. Schlese, U. Schulzweida, and A. Tompkins, 2003: The atmospheric general circulation model ECHAM5, part I: Model description. *Max- Planck- Institut für Meteorologie, Report No. 349*, 127pp.

110. Schlesingerm M, and N. Ramanktty, 1994: An Oscillation in the Global Climate System of Period 65-70 Years. *Nature*, 367, 723-726.

111. Schmittner A., C. Appenzeller, and T. F. Stocker, 2000: Enhanced Atlantic freshwater export during El Ni~no. *Geo. Phys. Res. Lett.*, 27 (8), 1163-1166.

112. Schott FA, R. Zantopp, L. Stramma, M. Dengler, J. Fischer, and M. Wibaux, 2004: Circulation and Deep-Water Export at the Western Exit of the Subpolar North Atlantic. *J. Phys. Oceanogr.*, 34(4): 817-843.

113. Spall, Michael A., 1996a: Dynamics of the Gulf Stream/Deep Western Boundary Current Crossver. Part I: Entrainment and recirculation. *J. Phys. Oceanogr.*, 26 (10), 2152-2168.

114. ——, 1996b: Dynamics of the Gulf Stream/Deep Western Boundary

Current Crossver. Part II: Low-frequency internal oscillations. *J. Phys. Oceanogr.*, 26 (10), 2169-2182.

115. Sturges, W., and B. G. Hong, 1995: Wind forcing of the Atlantic thermocline along 32±N at low frequencies. *J. Phys. Oceanogr.*, 25, 1706-1715.

116. Sutton, R.T., and D.L.R. Hodson, 2005: Atlantic Ocean forcing of North American and European summer climate. *Science*, 309, 115-118.

117. ——, and M. R. Allen, 1997: Decadal predictability of North Atlantic sea surface temperature and climate. *Nature*, 388, 563–567.

118. Te Raa, L. A., and H. A. Dijkstra, 2002: Instability of the thermohaline ocean circulation on interdecadal time scales, *J. Phys. Oceanogr.*, 32, 138-160.

119. ——, and H. A. Dijkstra, 2003: Sensitivity of North-Atlantic multidecadal variability to freshwater flux forcing, *J. Clim.*, 16, 2586-2601.

120. ——, J. Gerrits, and H. A. Dijkstra, 2004: Identification of the mechanism of interdecadal variability in the North-Atlantic Ocean, *J. Phys. Oceanogr.*, 34, 2792-2807.

121. Timmerman, A., M. Latif, R. Voss, and A. Grötzner, 1998: Northern Hemispheric interdecadal variability: A coupled air–sea mode. *J. Clim.*, 11, 1906–1931.

122. ——, S.-I. An, U. Krebs, and H. Goosse 2005: ENSO suppression due to weakening of the North Atlantic thermohaline circulation, *J. Clim.*, 18, 3122-3139.

123. Thompson D. W. J., and J. M. Wallace, 2000: Annular modes in the extratropical circulation. Part I: Month-to-month variability. *J. Clim.*, 13, 1000–1016.

124. ——, and J. M. Wallace, 1998: The Arctic Oscillation signature in the wintertime geopotential height and temperature fields. *Geophys. Res.*

Lett., 25, 1297–1300.

125. Tourre, Y. M., Y. Kushnir, and W. B. White, 1999: Evolution of interdecadal variability in sea level pressure,sea surface temperature and upper ocean temperature over the Pacific Ocean. *J. Phys. Oceanogr.*, 29, 1528-1541

126. Valcke, S., A. Caubel, D. Declat, and L. Terray, 2003: OASIS Ocean Atmosphere Sea Ice Soil users's guide. *CERFACS Tech. Rep. TR/CMGC/03/69*, Toulouse, France, 85pp.

127. van der Schrier, G., S.L. Weber and S.S. Drijfhout, 2002: Sea level changes in the North Atlantic by solar forcing and internal variability. *Clim. Dyn.*, 19 435-447.

128. Vellinga M, and P. Wu, 2004: Low latitude freshwater influence on. centennial variability of the Atlantic Thermohaline Circulation. *J. Clim*, 17(23):4498–4511.

129. Visbeck, M., H. Cullen, G. Krahman, and N. Naik, 1998: An ocean model's response to North Atlantic Oscillation–like wind forcing. *Geophys. Res. Lett.*, 25, 4521–4524.

130. ——, E. Chassignet, R. Curry, T. Delworth, B. Dickson, and G. Krahmann, 2003: The ocean's response to NAO variability. The North Atlantic Oscillation: Climatic Significance and Environment Impact, *Geophys. Monogr.*, Vol. 134, Amer. Geophys. Union.

131. Von Storch, J.-S., P. Müller, R. J. Stouffer, R. Voss, and S. F. B. Tett, 2000: Variability of deep-ocean mass transport: spectral shapes and spatial scales, *J. Clim.*, 13, 1916-1935.

132. ——, P. Müller, and E. Bauer, 2001: Climate variability in millenium integrations with coupled atmosphere ocean GCMs: A spectral view. *Clim. Dyn.*, 10, 1525–1543.

133. Wallace J. M., and D. W. J. Thompson, 2002: The Pacific center of action of the Northern Hemisphere Annular Mode: Real or Artifact? *J. Clim.*, 15,

1987-1991.

134. Weaver, A J., and E.S. Sarachik, 1991: Evidence for decadal variability in an ocean general circulation model: An advective mechanism. Atmosphere-Ocean, *R. W. Stewart Symposium Special Edition*, 29, 197-231.

135. ——, E. S. Sarachik, and J. Marotzke, 1991: Freshwater flux forcing of decadal and interdecadal oceanic variability. *Nature*, 353, 836–838.

136. Weisse, R., U. Mikolajewicz, E. Maier-Reimer, 1994: Decadal variability of the North Atlantic in an ocean general circulation model. *J. Geophys. Res.*, 99, 12411-12421.

137. Whitehead, J. A., 1989: Internal hydraulic control in rotating fluids-Applications to oceans, *Geophys. Astrophys. Fluid Dyn.*, 48, 169–192.

138. ——., A. Leetmaa, and R. A. Knox, 1974: Rotating hydraulics of strait and sill flows, *Geophys. Fluid Dyn.*, 6, 101– 125.

139. Willebrand, J. S., S. G. H. Philander, and R. C. Pacanowski, 1980: The oceanic response to large-scale atmospheric disturbances, *J. Phys. Oceanogr.*, 10, 411-429.

140. Winton, M., 1996: The role of horizontal boundaries in parameter sensitivity and decadal-scale variability of coarse-resolution ocean general circulation models. *J. Phys. Oceanogr.*, 26, 289–304.

141. Wolff, J.O., E. Maier-Reimer, E., Legutke, S., 1997: The Hamburg Ocean Primitive Equation Model HOPE. *Technical Report No. 13, German Climate Computer Center (DKRZ)*, Hamburg, Germany.

142. Wu, L. and Z. Liu, 2005: North Atlantic decadal variability: Air-Sea Coupling, Oceanic Memory and Potential Northern Hemisphere Resonance. *J. Clim.*, 18(2), pp. 331-349. doi: 10.1175/JCLI-3264.1.

143. Yin, F.L., I.Y. Fung, and C.K. Chu, 1992: Equilibrium response of ocean deep-water circulation to variations in Ekman pumping and deep-water

sources. *J. Phys. Oceanogr.*, 22, 1129-1157.

144. Zemba, J. C., 1991: The structure and transport of the Brazil Current between 278 and 368S. *PhD. Thesis*, MIT/WHOI Joint Program in Oceanography and Oceanographic Engineering, 160 pp.

145. Zhang, S., R. J. Greatbatch, and C. A. Lin, 1993: A reexamination of the polar halocline catastrophe and implications for coupled ocean–atmosphere modeling. *J. Phys. Oceanogr.*, 23, 287–299.

146. Zhu, X., K. Fraedrich, and R. Blender, 2006: Variability regimes of simulated Atlantic MOC, *Geophys. Res. Lett.*, 33, L21603, doi:10.1029/2006GL027291.

Acknowledgement

I would like to thank my principal supervisor, Johann Jungclaus, for his hand-in-hand guidance to acquaint me with models, soft-ware matters, for his inspiring discussions, his meticulous corrections of my manuscript.

I would like to thank my co-supervisor, Jochem Marotzke, for his enlightening advices and all his support.

Special thanks to my panel chair, Detlef Stammer, for the discussions we had and for his guidance to keep my research in the right direction.

Part of my work is done with cooperation with Klaus Fraedrich, Richard Blender, from University of Hamburg. Thanks to them for showing me a new view, for their helpful comments and all the intensive discussions we had.

Thanks to Richard Greatbatch, for his instructive advice I appreciate very much.

Special thanks to Guy Brasseur who gave me the great opportunity to join the IMPRS－ESM.

Thanks to Cornelia and Antje for their help, and for the fantastic annual retreats they organized.

Thanks to Helmut Haak for all the discussions and his unreserved help.

Thanks to Miren, Clotilde, Lin, Fiona, Robin, Malte, Marin, Semeena, Luca, Dirk, Felix, and all others for providing such a great and pleasant environment.

Thanks to Fan who led me through my first months in Hamburg.

Thanks to Katsu for the invaluable time we have together.

Finally I would like to thank Weiqiang, my brother, and particularly my dear parents, for their love and support!

Publikationsreihe des MPI-M
„Berichte zur Erdsystemforschung" , *„Reports on Earth System Science*", ISSN 1614-1199
Sie enthält wissenschaftliche und technische Beiträge, inklusive Dissertationen.

1

Publikationsreihe des MPI-M
„Berichte zur Erdsystemforschung" , *„Reports on Earth System Science*", ISSN 1614-1199
Sie enthält wissenschaftliche und technische Beiträge, inklusive Dissertationen.

Publikationsreihe des MPI-M
„Berichte zur Erdsystemforschung" , *„Reports on Earth System Science*", ISSN 1614-1199
Sie enthält wissenschaftliche und technische Beiträge, inklusive Dissertationen.